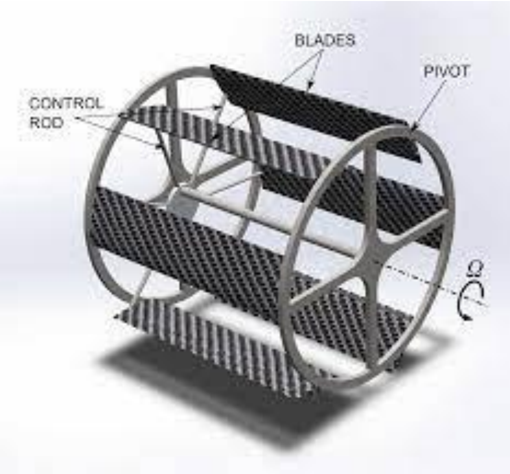

Analysis and description of cyclocopter performances

Alberto Ramos Escobar

Thesis to obtain the Master of Science Degree in

Aerospace Engineering

Supervisor: Prof. Filipe Szolnoky Ramos Pinto Cunha

Examination Committee

Chairperson: Prof. Afzal Suleman
Supervisor: Prof. Filipe Szolnoky Ramos Pinto Cunha
Member of the Committee: Prof. José Maria Campos da Silva André

November 2021

Acknowledgments

I would like to thank Professor Dr. Filipe Szolnoky Cunha for offering me this thesis when I had troubles to find one at the beginning of the semester and for helping me in every difficulty which I have been able to have during the realisation of it.

Moreover, I would like to thank my parents and my brother for giving me support whenever I needed it while I have been living a new experience abroad and thanks to this, I have been able to enjoy more it in Portugal.

Resumo

Na sequência do crescente interesse na utilização de drones, esta tese centra-se no estudo e análise do seu desempenho, mas utilizando um tipo específico de rotor: o ciclorotor.

Assim, os fundamentos do ciclocóptero, que é o nome que recebe este tipo de UAV, são explicados tanto do ponto de vista dimensional como aerodinâmico. Este objectivo é alcançado através do desenvolvimento de alguns códigos numéricos que permitem aproximar e assim, compreender o comportamento do escoamento em torno das pás do ciclorotor.

Finalmente, o impulso produzido e a potência consumida são os valores mais importantes a obter e assim, são apresentados alguns resultados mostrando a evolução destas variáveis quando alguns parâmetros dimensionais ou aerodinâmicos são variados.

Palabras-chave: Ciclocóptero, Aerodinâmica Instacionária, Velocidade Induzida, Tubo Duplo.

Abstract

Following the growing interest in the use of drones, this thesis is focused on studying and analysing their performance but using a specific type of rotor: the cyclorotor.

Like this, the fundamentals of cyclocopter, which is the name that receive this type of UAV, are explained from both dimensional and aerodynamic point of view. This objective is achieved by developing some numerical codes which allow to approximate and so, to understand the behaviour of the flow around the blades of the cyclorotor.

Finally, the thrust produced and the power consumed are the most important values to obtain and so, some results are presented showing the evolution of these variables when some dimensional or aerodynamic parameters are varied.

Keywords: Cyclocopter, Unsteady Aerodynamics, Induced Velocity, Double-Multiple Streamtube.

Table of Contents

List of Tables

List of figures

Acronyms

2D	Two-Dimensions
3D	Three-Dimensions
BEMT	Blade Element Momentum Theory
CFD	Computational Fluids Dynamics
DS	Double-Multiple Streamtube
MAV	Micro Aerial Vehicle
MIT	Massachusetts Institute of Technology
NACA	National Advisory Committe for Aeronautics
NASA	National Aeronautics and Space Admistritation
PIV	Particle Image Velocimetry
SS	Single Streamtube
UAV	Unmanned Aerial Vehicle
UVLM	Unsteady Vortex Lattice Method

Nomenclature

a	adimensional localization of pitching axis at ¼-chord
A	blade area
A_1, A_2	constants of Wagner's function
AR	aspect ratio
b_1, b_2	exponential constants of Wagner's function
b	blade span
c	blade chord
C	Theodorsen's function
C_d	drag coefficient
C_l	lift coefficient
C_l^c	circulatory part of lift coefficient
C_l^{nc}	non-circulatory part of lift coefficient
C_{D0}	sectional profile drag coefficient
C_{Di}	induced drag coefficient
$C_{l\alpha}$	lift curve slope
e	Oswald efficiency factor
F	resultant force
k	reduced frequency
L_1, L_2, L_3, L_4	4-bar linkage mechanism lengths
$\vec{L}$	lift
M	Mach number
N_b	number of blades
P	power consumed
Q	torque about the axis of rotation
q	pitch rate
R	blade radius
R_e	Reynolds number
s	reduced time
t	time step
T_{res}	resultant thrust
U_R	resultant velocity
U_P, U_T	normal and tangential velocity components
v_d	downstream induced velocity
v_u	upstream induced velocity
v_i	induced velocity
V	flow velocity
V_h, V_v	horizontal and vertical advance velocities

w	far downstream velocity
X_α, Y_α	recursive functions of angle of attack
X_q, Y_q	recursive functions of pitch rate
W	weight

Greek symbols

α	angle of attack
α_e	effective angle of attack
β	direction of the resultant thrust
η_r	localization of pitching axis at ¼-chord
ϑ	pitch angle
ϑ_a	pitch angle in forward flight
ρ	flow density
ε	phase angle of eccentricity
ϕ	Wagner’s function
Ψ	azimuthal angle
ω	angular velocity
Ω	rotation speed

Chapter 1

Introduction

1.1 Motivation

The tendency of using UAV (Umanned Aerial Vehicles) is increasing year after year due to the huge variety of applications in which this type of vehicles can be used. Drones can be used in areas like surveillance, meteorology, plague control, among others.

Moreover, most of drones have some advantages that conventional aircrafts can not achieved like more reduced dimensions, less consumption, an easier control and adaptability due to the fact that they do not have a pilot on board and several drones can be controlled by one on the ground. That is why drones are a very common topic for the present day researches.

Different types of drones can be found, explaining their huge utility. One classification is between fixed-wing and rotating-wing drones, being this last type the objective of this thesis because they can perform movements that the fixed wing can not like hover and moreover, they can be a great option in many activities due to their specific characteristics.

1.2 Objectives

The main goal of this thesis is to describe and analyse the aerodynamic of the cyclocopter studying velocities and forces that appear on the blades and a calculation of the power consumed is then performed. The hover case is first analysed and next, the forward motion. Moreover, three computacional models will be created using Matlab (two for hover and one for forward) and validated with experimental values obtained from different researches and like this, the general operation of the cyclocopter will be able to be represented.

In addition, a variation of some parameters that define the geometry and structure of the cyclocopter is going to be done and so, their effect on the aerodynamic of the cyclocopter could be obtained.

1.3 Thesis Structure

The thesis is divided in 5 chapters:

- Chapter 1: This initial chapter establishes an introduction to the analysis that is going to be carried out along the thesis, explaining the objetives of it as well as the motivations for doing it.

- Chapter 2: This chapter focus on showing the state of art of cyclopter and some scientific studies that were done. Finally, some general concepts related to the structure of the cyclocopter are described.

- Chapter 3: The main goal of this chapter is to describe the fundamentals of unsteady aerodynamic as well as the main theories used to approximate these effects appearing around the cyclocopter. In addition, two inflow models are going to be explained in order to be used to obtain results about the performance of the cyclocopter (velocities, forces, thrust...).

- Chapter 4: This chapter is focus on hover situation. First, the code which has been developed is explained in order to be next validated using some experimental results extracted from bibliography. Finally, some results about this performance are presented showing the most important conclusions.

- Chapter 5: The same that it was done in chapter 4 is now explained in chapter 5 but changing to forward motion. Therefore, the explanation and validation of the model, the results obtained with it and the comparison with the hover case are shown in this chapter analysing four movements (forward, backward, upward and downward).

- Chapter 6: This final chapter has the aim of exposing all the conclusions obtained along the thesis as well as a posible application which may be developed using the codes explained.

Chapter 2

The Cyclocopter

2.1 General Concepts

A cycloidoal rotor, cyclorotor or cyclocopter is a rotating-wing system where the span of the blades runs parallel to the axis of its rotation, like it is schematized in figure 2.1.

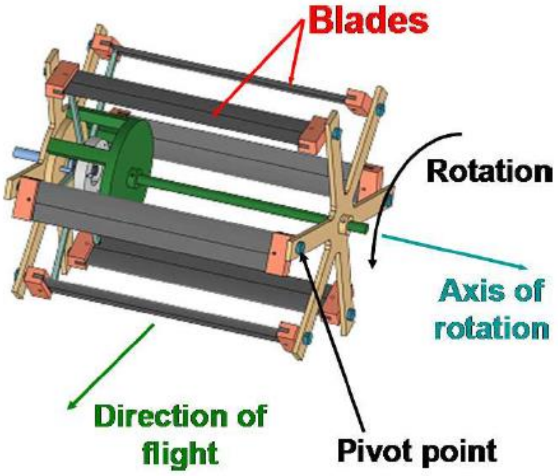

Figura 2.1: Cycloidal rotor [1]

In this type of aircraft, the pitch angle of each blade is varied cyclically by mechanical means such that each blade experiences positive geometric angles of attack at both the top and bottom halves of its circular trajectory. The variation of the amplitude and phase of the cyclic blade pitch is used to change the magnitude and direction of the net thrust vector (T_{Res}) produced by the cyclorotor. This resultant thrust can be decomposed into the vertical and horizontal directions (lift and forward thrust respectively which are shown in figure 2.2).

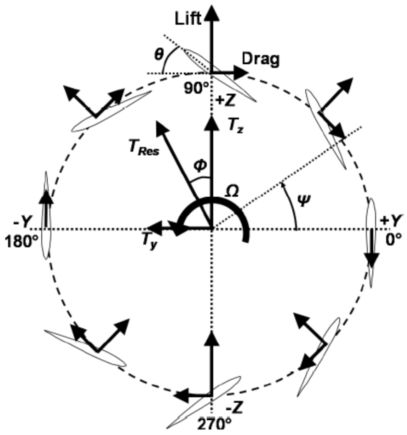

Figure 2.2: Forces in each azimuthal position [1]

In comparison to a conventional rotor, each spanwise blade element operates at similar aerodynamic conditions and so, the blades can be more easily optimized to achieve the best aerodynamic efficiency.

The next sections 2.2 and 2.3 are related to the state of art of the cyclocopter as well as the scientific studies developed during the century XXI.

2.2 State of Art

The concept of the cyclopter is more than 100 years old but its origin is not so clear yet. The earliest reported work was in 1909 done by E. P. Sverchkov. This military engineer in St. Peterburg (Russia) developed an aircraft called ''Samoljot'' (figure 2.3(a)) [8]. This ''wheel-orthopter'', which was another name that this vehicle received, had three flat surfaces, a rudder and the rear edge of one of surfaces could be bent replacing the action of an elevator. In order to create the lift and thrust, Samoljod had paddle wheels consisting of 12 blades and the pitch angle were changed by means of pulleys and springs. However, the vehicle did not pass the tests successfully because it not only did not come off ground but even did not move from the place.

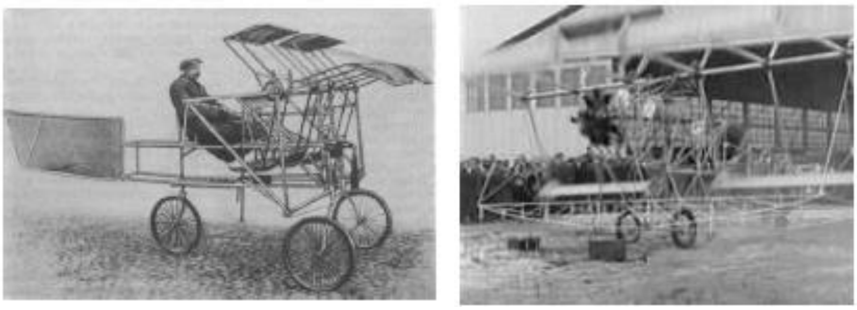

Figure 2.3: (a) Salmoljot aircraft (b) Unknown french aircraft [8]

Few years later, a cyclogyro design (figure 2.3(b)) was found out in France between 1909 and 1914. However, not too much information is available from this vehicle, only a video footage which shows two unsuccessful attempts [8].

In 1920, C.Brooks form Pattonville (Montana) designed an aircraft with a paddle-wheel actuator (figure 2.4) with an assembly frame in front of the engine which allowed to assume that thrust had to be produced by one more engine with the traditional propeller [8]. Moreover, there was a short, rotating upper wing for forward flight. However, one more time, this vehicle does not look like that it was be successful.

Figure 2.4: Brook's cyclogyro [8]

The next information comes from 1923, when Jonathan Edward Caldwell, an aeronautical engineer from US, filed for a patent on a device that he called the cyclogyro [8]. This aircraft consisted of an airplane fuselage with two paddle-wheel rotors which were powered by an engine in the fuselage. Like in an actual cyclocopter, the lift of the airfoils could be tuned to produce thrust in any direction by changing the pitch continuously. Moreover, by changing the angle of attack, the vehicle could move in any direction with differential thrust between the two rotors yawing could be achieved.

In 1937, Caldwell took again the model of 1923 and created a modified prototype (figure 2.5.) [8]. In this new design, Caldwell mounted two long three-bladed airfoil-equipped paddlewheels to the sides of a conventional-looking aircraft fuselage.

Figure 2.5: New Caldwell design [8]

In 1926, Bruno Nagler patented a cyclogyro with two 4-bladed cycloidal propellers on either side (figure 2.6) [9]. A particularity of this design was that the blade pitching mechanism was passive and since the blade center of gravity was coincident with the pitching axis, this passive mechanism is fully governed by the aerodynamic forces. Like this, the required blade kinematics changed depending on the flight condition and the pilot had pitch, roll and yaw control during all times.

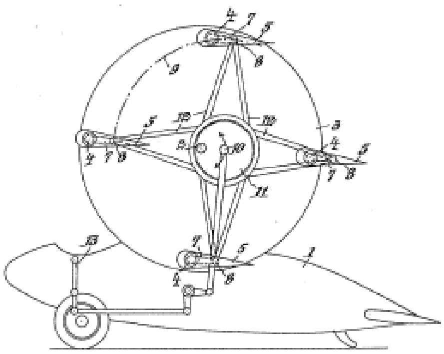

Figure 2.6: Nagler’s cyclogyro [9]

Meanwhile, Adolf Rohrbach created a cyclogyro with two cyclorotors operating like wings of a high-wing monoplane (figure 2.7) [8]. This aero-technician achieved on this aircraft that the variation of angles of attack were calculated in such way that both lift and thrust are developed during a most part of revolution.

Figure 2.7: Rohrbach’s cyclogyro [8]

In 1930, Schroeder developed a single-place cyclogyro replacing the conventional screw propeller for two large cycloidal propellers (figure 2.8 (a)) [10]. Three years later, Haviland Hull Platt used the Rohrbach’s cyclogyro research to design his own cyclogyro (figure 2.8 (b)) [8] whose paddle-wheel wing arrangement was awarded a US patent. Thanks to this, Platt’s cyclogyro was used in an extensive wind-tunnel testing at MIT (Massachusetts Institute of Technology).

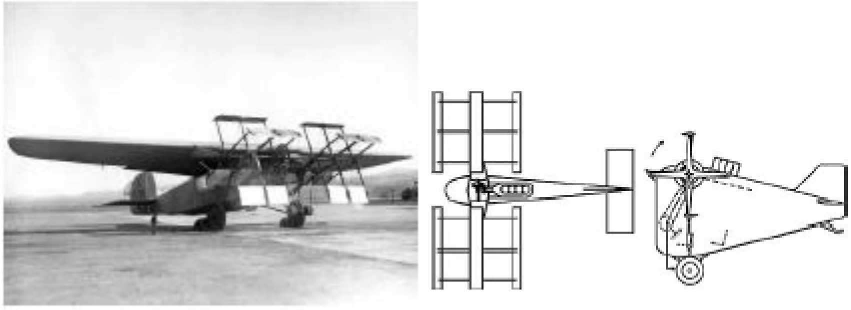

Figure 2.8: (a) Schroeder’s cyclogyro [10] (b) Platt’s design [8]

In 1935, the next design appears by Rahn Aircraft Corp. This consists of a one-seater aircraft with two 6 feet rotating wings on each side that allow the plane to rise or descend vertically and fly laterally without a propeller (figure 2.9) [8]. However, there is not any record which demonstrates that this cylogyro accomplished any of these feats.

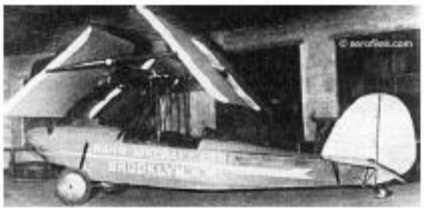

Figure 2.9: Rahn Aircraft Corp. cyclogyro [8]

In 1976, Marcel Chabonat filed a patent for a new type of cyclorotors that he named propulsive lifting rotors (figure 2.10) [8]. In this new type of two-bladed rotors, the variation of an angle of incidence was obtained in a passive way using the aerodynamic and/or centrifugal forces. However, he changed this later using profiled cams to vary the angle of incidence. Depending on the mode of flight (take-off, climb...), the set of cams changed.

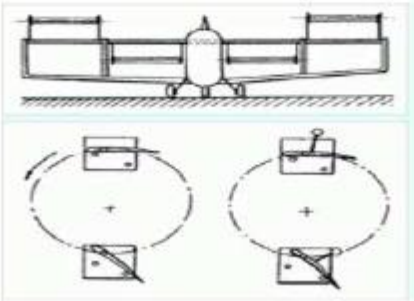

Figure 2.10: Marcel's patented cyclorotors [8]

In 1977, Thomas H. Sharpe patented an aircraft design where cyclogyros were used to increase the lift (figure 2.11 (a)) [8]. These cyclorotors are placed in a wing and used as ordinary fans ans thanks to a simplified eccentric mechanism, the angles of incidence are controlled. Later, a second version of this design was done and this was intented for high-speed aircraft (figure 2.11(b)).

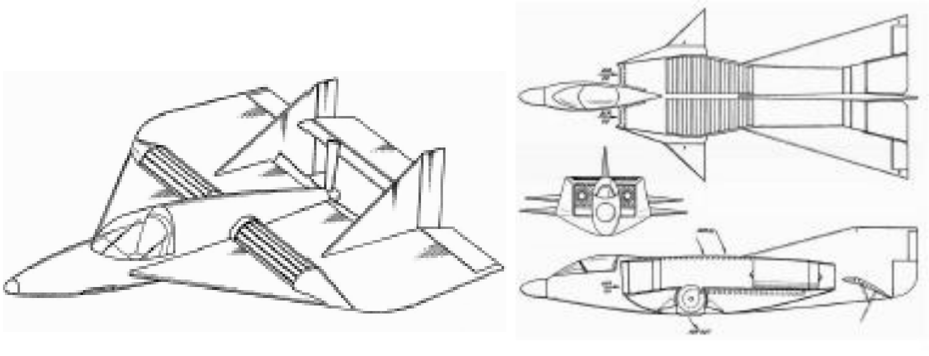

Figure 2.11: (a) Sharpe's first version (b) Sharpe's second version [8]

In 1980, Arthur G. Crimmins designed a composite aircraft whose main goal was to be a flying crane (figure 2.12) [8]. The particularity of this model is that had different configurations like ''classical'' airship, ''classical'' cyclogyro and all intermediate configurations. Thanks to this possibility of changing the configuration, the thrust vector could be orientated in all directions without restrictions and that is what a flying crane needs.

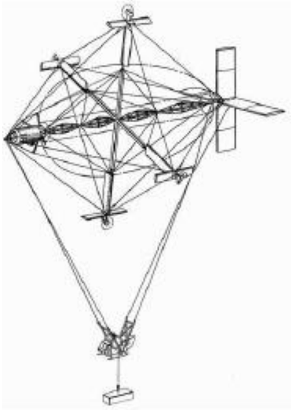

Figure 2.12: Crimmins's flying crane [8]

Finally, in 1992, Heinz A.Gerhardt patented a ''paddle wheel rotorcraft'' (figure 2.13) [8]. This was basically a cyclogyro and one main feature of it was the absence of kinematic management of an angle of incidence of blades. The control was done by a computer which provided the required blade kinematics achieving the optimum performance in all regimes of flight.

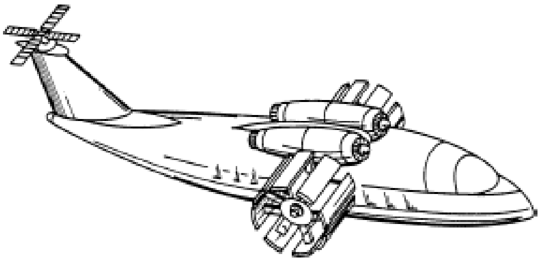

Figure 2.13: Heinz's cyclogyro [8]

2.3 Scientific Studies

Like it was explained in the previous section 2.2., the early attempts that the different engineers did in order to make possible the creation of a flying cyclocopter failed. The main reason was because they did not understand so well the physics of this type of vehicles. So, the next step was to do some scientific studies in order to solve all the problems that appear and this is the content of this section focusing on researches done during the century XXI.

From 1961 to 1998, there was a stop in the researches about cyclocopter. However, Bosch Aerospace revived the idea in 1998 studying the feasibility of using a cycloidal propulsion system for an UAV with around 300 kg of weight (figure 2.14) [8].

Figure 2.14: Bosch Aerospace cycloidal propulsion system [8]

Although the company wanted to use this system for heavier-than-air UAV, finally the cyclorotor was used for control aims. Bosh Aerospace built a cyloidal propeller with a test rig (figure 2.15) [11] which was capable of measuring the rotation speed, the lift and the torque that the propeller needed.

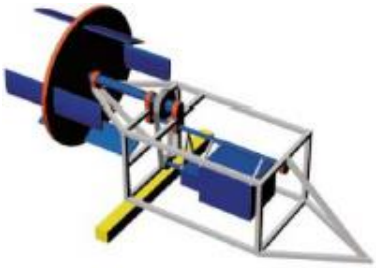

Figure 2.15: Experimental cycloidal propeller [11]

Then, the company collaborated with Mcnabb of the Raspet Flight Laboratory from Mississippi and they developed a simplified unsteady aerodynamic model based on Garricks's formulation for a cycloidal propeller operating in hover and small forward flight speeds [12]. The forces predicted by this model was compared with the wind tunnel data obtained by Wheatley in 1935 and also with the results from the tests conducted by the company itself [13]. In conclusion, it was found that the unsteady effects had to be included not only to the lift and the pitching moment but also to the drag and this would explain the underprediction of power that was found in the analysis.

In 2003, Iosilevskii and Levy carried out a combined experimental and numerical study on a cyclorotor operating at Reynolds numbers around 40000, measuring the forces and moments produced thanks to a experimental rig (figure 2.16) [14].

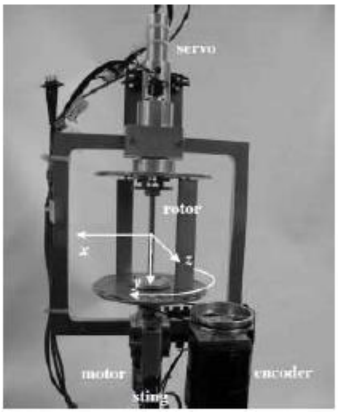

Figure 2.16: Experimental setup of Iosilevskii and Levy analysis [14]

The conclusion obtained was that the resultant thrust formed an angle with the vertical due to a lateral force that appeared. The origin of this force was attributed to the Magnus effect produced by the rotor spinning in the induced flow originated by it [14].

In addition, a 3-D CFD simulation was done in order to compare the average forces obtained with this new method with the experimental results. Thanks to this, the direction of the thrust led by about 10º but the trend was correct [15].

Like Iosilevskii and Levy's research, from 2003 to 2008, Seoul National University did an study combining experimental and computational analysis. In comparison to previous study, this research used double-multiple-streamtube theory for predicting the resultant thrust produced which is compared later with the experimental values [16].

In relation to the experiments, the university carried out some of them with different geometries and aerodynamic parameters [4,16,17]. Among these parameters were the rotor diameter, number of blades, rotational speed and the blade pitching amplitude and phase. The results showed that the thrust and power varied as the square and cube of rotational speed respectively. Moreover, it was found that the resultant force was inclined like Iosilevskii and Levy also stated. However, the reason for this lateral force was not only attributed to the Magnus effect, because this research stated that the curvature of the induced flow in the downstream part of the rotor also caused this partly. Other conclusions obtained were:

- Cyclocopter blades did not stall and so, there was not a decrease in the thrust until a picthing amplitude of 30º.

- Increasing in thrust until this high pitching amplitudes was attributed to the dynamic stall phenomenon.

- Possibly also due to this dynamic stall, the power also suffered a fast increase with pitch angle. However for a constant thrust, the power loading (thrust/power) increased with pitching amplitude until 30º and the rotor with the highest radius had the highest power loading.

- When the number of blades was changed, it was observed that the increase in thrust was not proportional to the increase in number of blades. In addition, the 3-bladed rotor produced the highest power loading. The next was the 2-bladed rotor and finally, the 6-bladed rotor.

- For a constant tip speed, the thrust increased with the rotor radius.

Seoul National University also built a range of UAVs with cycloidal blades system in order to evaluate its potential for VTOL vehicles in hover and low speed forward flight. Some of these cyclocopters are shown in the following figure 2.17 [18].

Figure 2.17: Seoul National University cyclocopter designs [18]

Finally, now a 2-D CFD analysis was also done using STAR-CD, a commercial software, to determine the aerodynamic design parameters of the cyclocopter rotor system [4,16,17]. The objective was to understand the flow conditions around the blades (figure 2.18) and like this, be used for aerodynamic design goals. In conclusion, the resultant forces from the CFD model adapted well to the experiments.

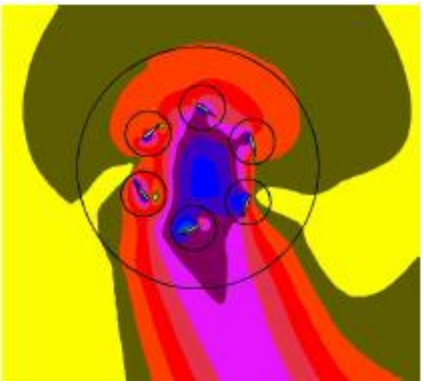

Figure 2.18: Seoul National University 2-D CFD model [17]

In 2006, Yu from the National University of Singapore did an analysis to predict the thrust and power of a MAV-scale cyclorotor in hover using a 3-D Unsteady Vortex Lattice Method (UVLM) which assumed that the flow was inviscid and irrotational [19]. Yu used some vortex rings which were selected as singular elements and deployed on blade surfaces and wake sheets (figure 2.19).

Figure 2.19: Yu's UVLM model and results [19]

Thanks to this UVLM analysis, the effect of blade pitching amplitude, planform taper ratio, blade span-to-rotor diameter ratio and winglets at blade tips was studied in relation to power loading at constant disk loading. The conclusions obtained were:

- The moderate pitching amplitude provided the highest power loading.
- Blade planform taper-ratio did not have any significant effect on power loading.
- For the same disc area, the rotor with the smallest radius and highest blade span provided the highest power loading.
- The presence of winglets decreased the power loading.

In addition, an experimental study was carried out using a newly developed innovative 5-bar based pitching mechanism (figure 2.20) [20]. These experiments was done to investigate the effect of the blade airfoil section comparing flat plate with NACA 0012 and planform taper ratio.

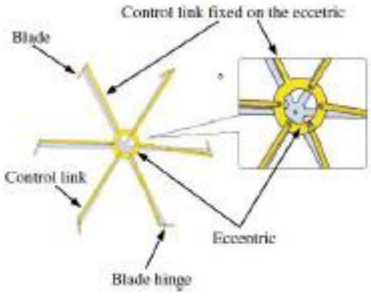

Figure 2.20: Yu's 5-bar pitching mechanism [20]

Meanwhile, Sirohi performed systematic experimental parametric studies on 3- and 6-bladed micro-scale cyclorotors at the University of Maryland in 2006 (figure 2.21) [21]. The aim was to measure the thrust and torque produced varying the rotational speed and pitching amplitude. It was found that thrust increased as the square of rotational speed and power, as the cube. The most important conclusion obtained from the study was that cyclorotor could be promising at very low Reynolds number which is a typical range of operation of MAVs.

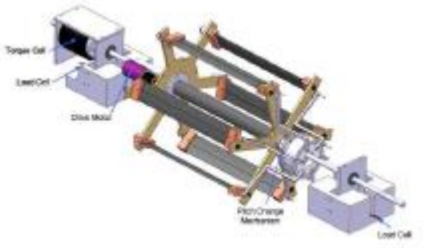

Figure 2.21: Sirohi's experimental setup [21]

Other research that was developed in 2006 was done by Acuity Technologies which performed both experimental and 2-D CFD studies on a model cyclorotor [22]. The objective was to built a VTOL transport aircraft using cyclorotors. In relation to the 2-D CFD model (figure 2.22), the analysis was carried out on different blade shapes and rotor geometries for determining the forces, torques and power requirements in hover and high speed forward flight.

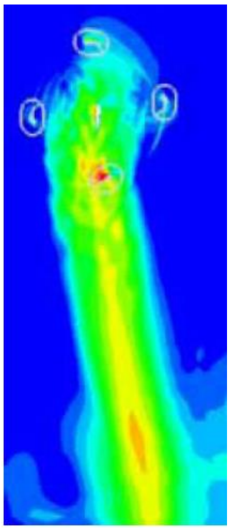

Figure 2.22: 2-D CFD model of Acuity Technologies [22]

One year later, in 2007, Siegel from the US airforce continued with the 2-D CFD analysis in order to demonstrate the capability of a cycloidal propeller to use unsteady, dynamic lift for operation at MAV-scale Reynolds number (figure 2.23) [23]. For the CFD computations, the full compressible Navier-Stokes equations were solved based on the Finite Volume Formulation. The simulations were done varying the forward flight speeds with different combination of frequency, radius of the foil motion, phase and pitch amplitude.

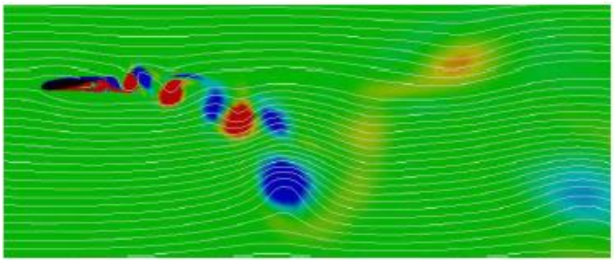

Figure 2.23: Siegel's 2-D CFD model [23]

The same year as before, two engineers developed new types of mechanism. The first one was designed by Hara and it was a more efficient and innovative flying mechanism for cyclogyro-based horizontal axis rotorcrafts (figure 2.24) [24]. The mechanism had two different parts, a revolving slinder-crank mechanism and a pantograph-link. Due to the motions, the wing segments located on the pantograph links reciprocated and swung around the center of the wing chord.

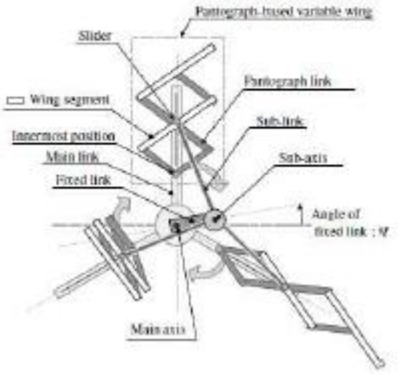

Figure 2.24: Hara's new mechanism design [24]

The other engineer was Tanaka who designed a new variable angle of attack mechanism. The main feature of this mechanism was the eccentric rotational point which had the ability to change the blade pitch angle with the azimuthal positions of the blades in a passive way. The aim of this experiment was to maximize the lift produced by the rotor.

In 2009, Nozaki developed experimental researches on a cycloidal rotor to be used on a 20 meter airship (figure 2.25) with the aim to determine the thrust produced [25]. The resultant conclusion was consistent with the previous studies because the direction of the thrust was found to have a phase lag of 10º with the vertical direction.

Figure 2.25: Nozaki’s cycloidal rotor [25]

One year later, in 2010, Kan from the University of Maryland carried out 2-D and 3-D simulations of a MAV-scale cyclorotor in hover (figure 2.26) [26]. For these simulations, it was used OVERTURNS which is a compressible Reynolds-Averaged Navier-Stokes (RANS) solver with the goal of investigating the performance and flow physics and like this, developing a computational methodology to understand the complex aerodynamics of the cyclorotor. Thanks to the code, it was found that the maximum vertical force and power was achieved when the blade was at the lowest azimuthal position in circular blade trajectory. The reason was due to the virtual camber effect which imposed a positive camber on the symmetric airfoil at the bottom of the cyclocopter cage and a negative camber at the top.

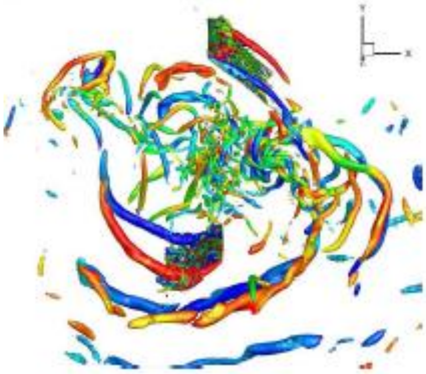

Figure 2.26: Kan’s 3-D simulation [26]

In 2010, Nakai developed an experiment about the flow around a cycloidal propeller using a particle image velocimetry (PIV) system whose data acquisition was synchronized with the propellers angular position (figure 2.27) [27]. The images obtained revealed the presence of a downwash around the propeller during the generation of lift.

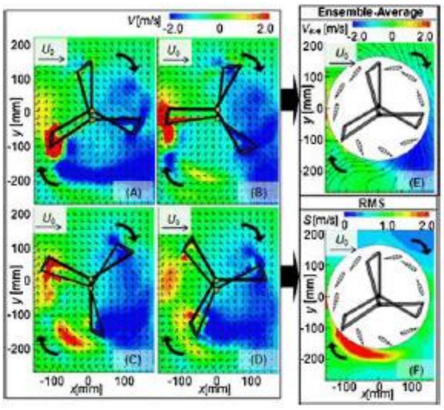

Figure 2.27: Nakai’s 2-D PIV measurement [27]

In 2016, G.Warmbroth and S.Husseyin, two engineers from NASA, tried to design a stopped rotor cyclocopter to be used for a mission to Venus [28]. This cyclocopter should be capable of flying in all atmospheric layers of Venus. Moreover, the cyclorotor blades would be used as both a propulsive system and for VTOL during the mission. Therefore, three main designs were tested with three different yaw angles of a cyclorotor in the stopped position (figure 2.28). The models were created in Rhino and simulated in RotCFD for both high altitude properties on Venus and low altitude flow properties. Finally, plots of lift coefficient vs angle of attack were created to find the stall angle of these designs and like this, identify the cyclorotor yaw angle with the least drag compared to lift.

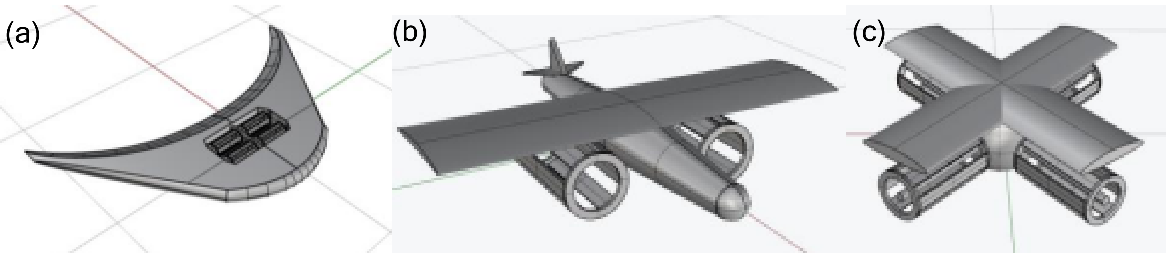

Figure 2.28: NASA's (a) first design, (b) second design and (c) third design of Venus mission cyclocopter [28]

Finally, two interesting studies developed during this year 2021 are going to be presented. The first one is the development of a nonlinear aeroelastic coupled trim model of a twin cyclocopter in forward flight by engineers Moble Benedict and Atanu Halder [29]. This twin cyclocopter consisted of two cycloidal rotors as main thrusters and a conventional nose rotor for pitch-torque balance (figure 2.29). In this coupled trim procedure, blade aeroelastic response equations and vehicle trim equations were solved together by simultaneously updating control inputs and blade response. Once the model was validated with previously published data by the authors, it was used to understand the trim behaviour of a micro-air-vehicle-scale twin cyclocopter in forward flight.

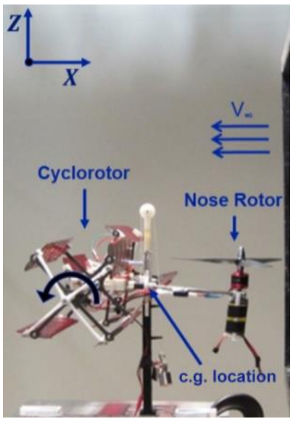

Figure 2.29: Side view of Benedict and Atanu's cyclocopter [29]

The other study was the design and experimental validation of an all-terrain cyclocopter micro-air-vehicle capable of power-efficient aerial, terrestrial and aquatic locomotion wihh seamless transition between the modes [30]. The cyclopcopter was designed by engineer Elena Shrestha and it had four cycloidal rotors whose rotational speeds and thrust vectors were individually modulated to sustain stable hover in aerial model. For the aquatic mode, a similar control strategy using the aerodynamics forces was developed. For the terrestrial mode, two wheels were efficiently integrated into the carbon fiber rotro endplates. Seamless transition was achieved using a retractable landing gear system.

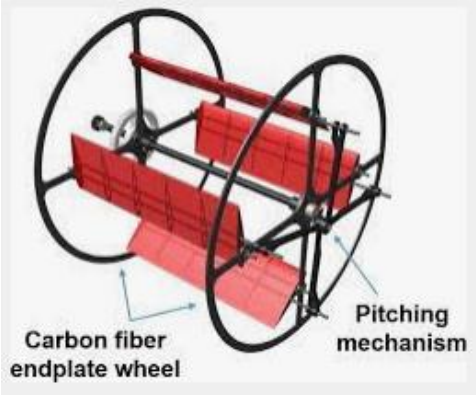

Figure 2.30: Elena’s all-terrain cyclocopter design [30]

2.4 Cyclocopter Structure

The main challenge in the cyclocopter design is to obtain the lowest possible weight and mechanical complexity. However, this is a complex task due to the structural design. The reason is because in a cyclorotor, there is a large rotating structure which has to be carefully designed to be strong enough to handle the large centrifugal loads and light enough to be used on a flying vehicle.

For dealing with this problem, the two mains part of a cyclopcopter are going to be discussed in the following subsections and are:

- Blades (following reference [1]).
- Blade Pitching Mechanism (following references [1] and [2]).

2.4.1 Cyclocopter Blades

In order to obtain an efficient cyclorotor, it is necessary to analyse the structural design of the blades. Thin flat blades are very flexible but thanks to some researches, it was found that the flexibility degrades the performance of the cyclocopter. If the thickness is increased, the blades are stiffer but turned out to be heavier. So, one of the main objectives is to make blades which are light and also structurally stiff enough to withstand the high centrifugal forces. In addition, this centrifugal forces act in the transverse direction and so, the blade design has to be stiff enough to limit transverse bending and torsional deformations. Increasing the bending and torsional stiffness results in heavy blades and now, the rotor structure weight has also to be higher in order to compesate the increase in the blades weight. All these changes resulted in cyclocopters which are considerably heavier than their conventional counterparts.

However, thanks to the new manufacturing techniques and high power-to-weight ratio propulsion systems, it looks feasible to design a cyclocopter at smaller scales.

2.4.2 Blade Pitching Mechanism

This mechanism is necessary to allow the cyclorotor to be used on a flying vehicle. It is passive mechanism consisting mainly of two bearings, one inserted in the other, and the linkages are connected to the offset ring which is installed around the second bearing (figure 2.31 (a)). So, if the connection between the axis of rotation and the mechanism is direct, the only losses that appear are due to the friction of the moving components. The geometry of it is shown in figure 2.31 (b).

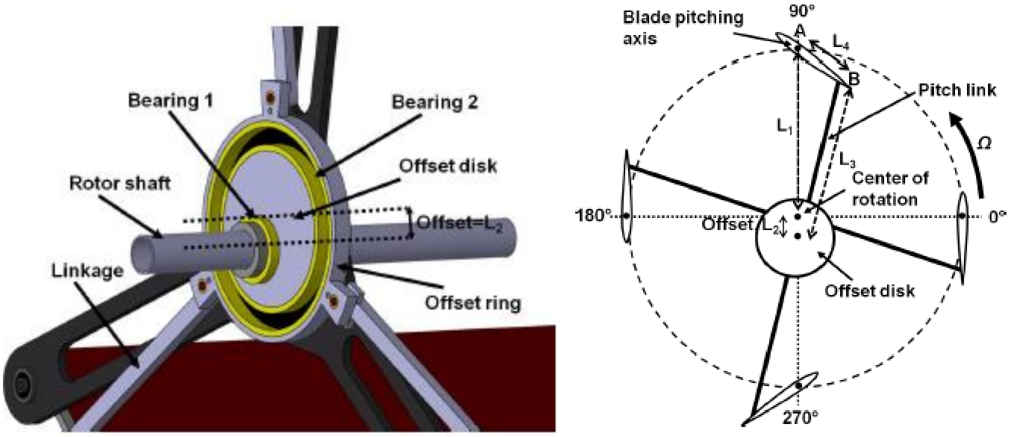

Figure 2.31: (a) Blade pitching structure (b) Description of the mechanism [1]

Like it is represented in the schematic of the figure 2.31, there is an offset (L_2) between the axes of the bearings. The connection between the second bearing and the blades is done at points A and B, defining the distances L_1 and L_3. Finally, the distance between A and B is L_4. The resulting system is four-bar linkage mechanism which allows to obtain the required cyclic change in blade pitch and also, in the angle of attack. In order to change the pitch amplitude, the offset length L_2 can be varied and like this, the magnitude and direction of the thrust produced.

The next step is to try to find an analytical model that approximates the kinematics of this mechanism and be able to calculate the pitch angle θ and the angle of attack α in every azimuthal position Ψ of the blades.

$$\theta = \frac{\pi}{2} - \alpha \qquad ; \qquad \alpha = \alpha_1 + \alpha_2$$

where α_1 and α_2 are defined in figure 2.32.

According to reference [2], the equations can be found applying sine and cosine theorems to the triangles that are defined in figure 2.32.

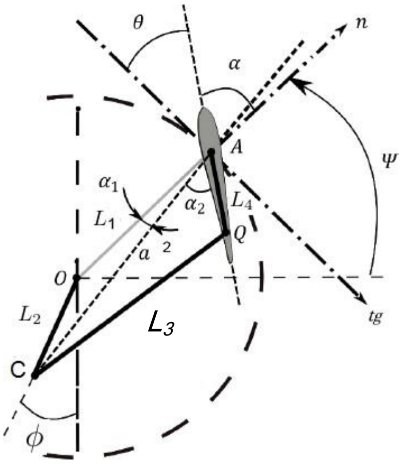

Figure 2.32: Schematic for kinematic equations [2]

Therefore, the equations that define the problem are the following

$$a^2 = L_2^2 + L_1^2 - 2L_1L_2\cos(\Psi+\phi+{}^{\pi}/_{2}) \qquad (2.1)$$

$$\frac{sin(\alpha_1)}{L_2} = \frac{1}{a}\cos(\Psi+\phi+{}^{\pi}/_{2}) \qquad (2.2)$$

$$L_3^2 = a^2 + L_4^2 - 2aL_4cos(\alpha_2) \qquad (2.3)$$

where all the lengths and angles are shown in figure 2.32.

Thanks to the last equations and the definitions of the pitch angle and the angle of attack, the result is:

$$\theta(t) = \frac{\pi}{2} - sin^{-1}\left[\frac{L_2}{a}cos(\Psi+\phi)\right] - cos^{-1}\left(\frac{a^2+d^2-L_3^2}{2aL_4}\right) = f(\Psi(t)) \qquad (2.4)$$

Once the initial blade positions are known, their pitch angles at each instant can be obtained using the equation (2.4).

Chapter 3

Aerodynamic Analysis

This chapter is focus on explaining the origin and the effects of the unsteady aerodynamics. Thanks to this, it will be possible to see how it affects to the performance of the cyclocopter and so, to the forces that it generates and the power consumed.

The first step is to explain the reduced frequency and how the unsteady effects can be quantified using this parameter. This will allow us to differentiate among steady, unsteady and highly unsteady problems.

Next, two unsteady models are studied in order to approximate the unsteady aerodynamics. The first one will be Theodorsen's model in which three different types of movement will be considered (pure angle of attack oscillations, pure plunging oscillations and pitch oscillations). The other one is the indicial response method which is based on Wagner function and Duhamel superposition principle in order to solve the problem.

Finally, two inflow models are explained in order to predict and analyse the unsteady aerodynamics around the cyclorotor. These two inflow models are the Single Streamtube (SS) and Double-multiple Streamtube (DS) models.

3.1 Unsteady Aerodynamic

All the information which is going to be presented in the following sections is obtained from reference [3].

3.1.1 Introduction

Like in helicopter performances, the design of new UAVs has improved due to the ability to predict accurately the aerodynamic behaviour of the rotor (cyclorotor) in all the operational envelope. However, the major difficulty is to describe the unsteady aerodynamic effects that appear, especially in high speed forward flight and during maneuvers with the aim to approximate their impact on the airloads and the performances.

In the following points, the origin of this unsteady effects are going to be explained as well as different models that have been developed in order to predict and take into account them in the codes which finally are going to be explained

3.1.2 Sources of Unsteady Aerodynamic

First of all, it is important to define the movements that determine the blade motion (figure 3.1). The angle of attack of a typical blade is a combination of forcing from collective and cyclic blade pitch, twist angle, elastic torsion, blade flapping velocity and elastic bending.

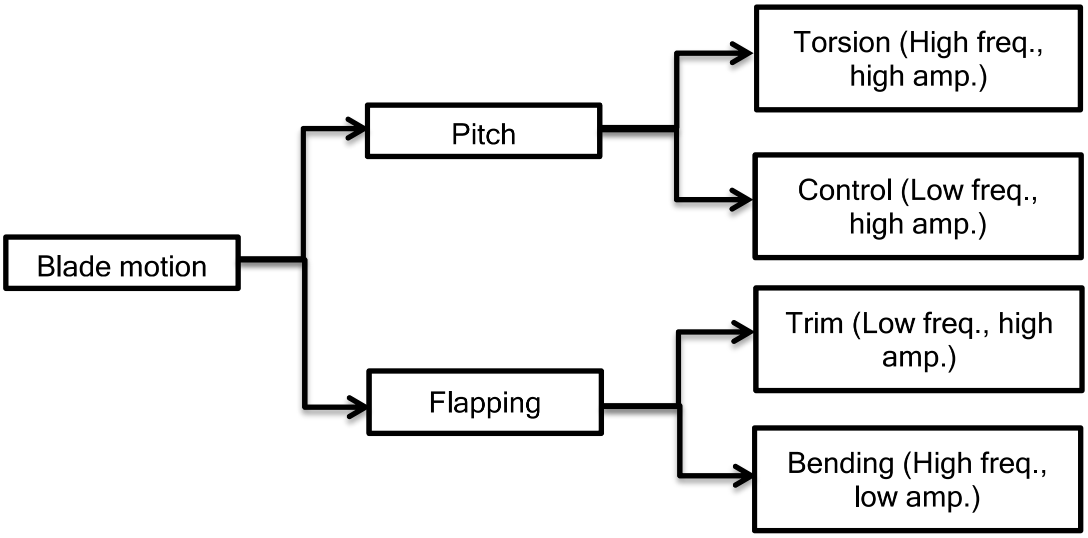

Figure 3.1: Decomposition of the blade motion

In addition, the flow field structure can be decomposed into periodic and non-periodic effects (figure 3.2). Inside the periodic effects, it is found the high velocity fields, induced downwash effects and sweep of them. On the other hand, the non-periodic effects are the fuselage flowfield, the discrete vortices produced at the blade tips and the wake distortion.

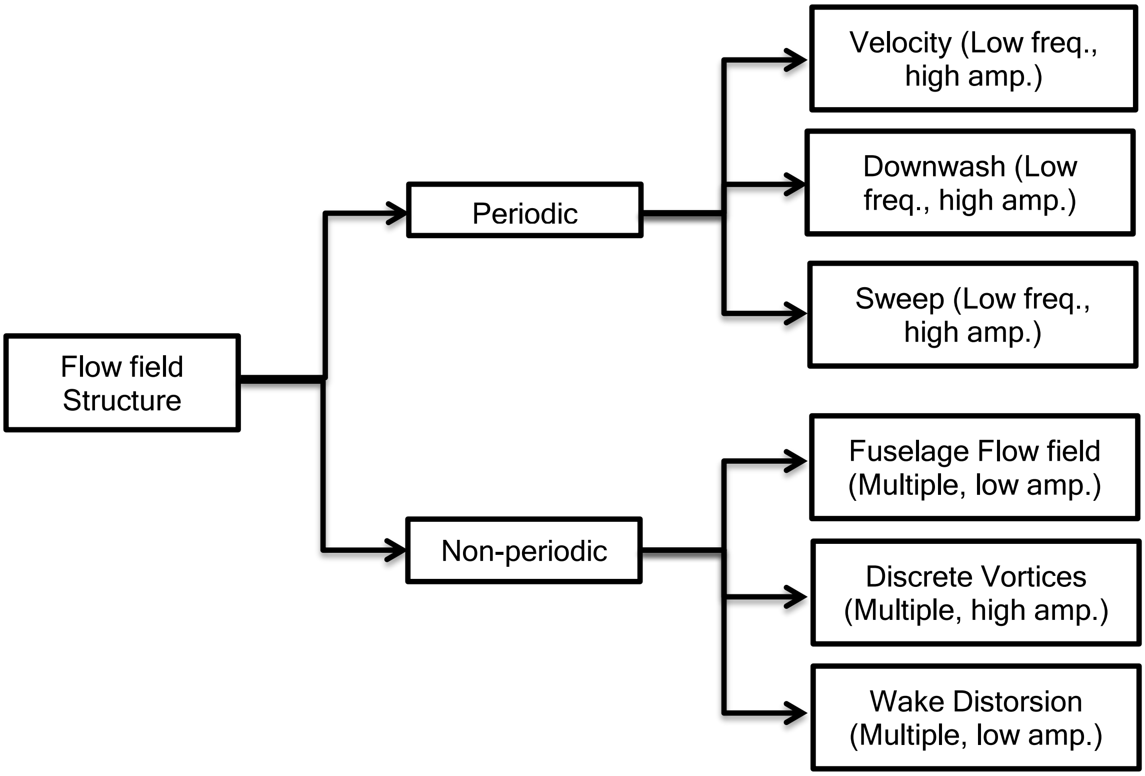

Figure 3.2: Flow field structure composition

In relation to the unsteady effects, these can be divided into perturbations to the local angle of attack and velocity field. Other point of interest is to study the amplitude and frequency of these effetcs. When the angle of attack is low with fully attached flow, the unsteady effects appear as moderate amplitude and phase variations relative to the quasi-steady airloads. However, with high angles of attack when time-dependent flow separation from the airfoil may be involved, a new phenomenon occurs called dynamic stall which involves large overshoots in lift, drag and pitching moment and much larger phase variations in the unsteady airloads. Moreover, these stalled airloads and more precisely, the amplitude and phase effects that they produced can lead to aeroelastic problems on the rotor limiting the performances.

3.1.3 Reduced Frequency (k)

The next step is to try to characterize these unsteady effects. In order to achieve this, the reduced frequency (*k*) is the most important parameter which allows the definition of a degree of unsteadiness of the problem. The definition of this parameter in terms of the airfoil semi-chord *b=c/2* is:

$$k = \frac{\omega b}{V} = \frac{\omega c}{2V} \qquad (3.1)$$

where ω is the angular frequency of the problem, *c* is the airfoil chord and *V* is the flow velocity.

Moreover, it can be shown using dimensional analysis the resultant force F that appears on an airfoil depends on the Reynolds number *(Re),* Mach number *(M)* and also, on this reduced frequency parameter to take into account the unsteady effects which may occur.

The degree of unsteadiness using the reduced frequency is measured in the following way:

- $k = 0$: Flow is steady.
- $0 \leq k \leq 0.05$: Flow can be considered quasi-steady, so the unsteady effects are generally small and they may be neglected completely for some problems.
- $0.05 \leq k \leq 0.2$: Flow is unsteady and now, the unsteady terms can not be neglected.
- $k \geq 0.2$: Flow is highly unsteady and the unsteady terms dominate the behaviour of the airloads.

However, this parameter is only an approximation and its use is only to illustrate the potential significance of unsteady effects. Therefore, if the problems are more transient, the reduced frequency loses its significance and so, it is normal to work with the reduced time s whose definition is:

$$s = \frac{1}{b}\int_0^t V dt = \frac{2}{c}\int_0^t V dt$$

This new parameter represents the relative distance travelled by an airfoil through the flow in terms of airfoil semi-chords during a time interval *t*.

3.2 Unsteady Models

3.2.1 Theodorsen’s Theory

Theodorsen solved in 1935 [3] the problem of finding the airloads on an oscillating airfoil that Glauert started to study in 1929. Theodorsen’s model gives a solution to the unsteady airloads on a 2-D harmonically oscillated airfoil in inviscid, incompressible flow and subject to small disturbance assumptions (figure 3.3).

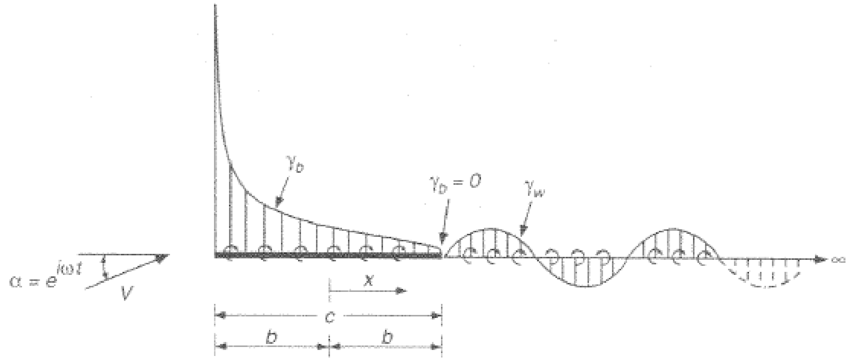

Figure 3.3: Theodorsen's model representation [3]

The representation of the airfoil and its shed wake is done using a vortex sheet. The shed wake is shown like a planar surface due to the angle of attack disturbances remain small and it extends from the trailing edge downstream to infinity. Moreover, the shed wake comprises counter circulation that is shed at the airfoil trailing edge and is convected downstream at the free-stream velocity.

As it is shown in figure 3.3, two types of vorticity appear. One of them, the bound vorticity γ_b can sustain a pressure difference and therefore, a lift force. The other vorticity, the wake vorticity γ_w must be force free with zero net pressure jump over the shed wake. Thanks to these vorticities, Theodorsen's problem is focus on obtaining the solution for γ_b on the airfoil surface under harmonic forcing conditions. However, this problem is not trivial but for simple harmonic motion, Theodorsen gives a simple solution in terms of lift and pitching moment for a general motion combination of pitching $(\alpha, \dot{\alpha})$ and plunging (h) motion in a flow of steady velocity *V*:

$$L = \pi\rho V^2 b\left[\frac{b}{V^2}\ddot{h} + \frac{b}{V}\dot{\alpha} - \frac{b^2}{V^2}a\ddot{\alpha}\right] + 2\pi\rho V^2 b\left[\frac{\dot{h}}{V} + \alpha + \frac{b\dot{\alpha}}{V}\left(\frac{1}{2} - a\right)\right]C(k) \qquad (3.2)$$

$$M = -\rho b^2\left(\pi\left[\frac{1}{2} - a\right]Vb\dot{\alpha} + \pi b^2\left[\frac{1}{8} + a^2\right]\ddot{\alpha} - a\pi b\ddot{h}\right) + 2\rho V b^2\pi\left(a + \frac{1}{2}\right)\left(V\alpha + \dot{h} + b\left[\frac{1}{2} - a\right]\dot{\alpha}\right)C(k) \qquad (3.3)$$

where *a* is the pitch axis location relative to the mid-chord of the airfoil and ρ is the density of the flow. Moreover, in these two equations 3.2 and 3.3, it is possible to difference two different terms. The first set is the non-circulatory or apparent mass effect which results from flow acceleration effects. The second terms are the circulatory effect and they arise from the creation of circulation about the airfoil.

In addition, the complex function that appears in the circulatory term $C(k) = F(k) + iG(k)$ is known as Theodorsen's function and it is used to take into account the effects of the shed wake on the unsteady airloads. This function can be expressed in terms of Hankel functions *H* which are defined as $H_v^{(2)} = J_v - iY_v$ with J_v and Y_v being Bessel functions of the first and second kind respectively.

$$C(k) = \frac{H_1^{(2)}(k)}{H_1^{(2)}(k) + iH_0^{(2)}(k)}$$

$$Real\big(C(k)\big) = F = \frac{J_1(J_1 + Y_0) + Y_1(Y_1 - J_0)}{(J_1 + Y_0)^2 + (J_0 - Y_1)^2} \quad ; \quad Imag\big(C(k)\big) = G = -\frac{Y_1Y_0 + J_1J_0}{(J_1 + Y_0)^2 + (J_0 - Y_1)^2}$$

With these definitions, the amplitude and phase of Theodorsen's function is represented in the following figure 3.4:

$$|C(k)| = \sqrt{F^2 + G^2} \quad ; \quad \phi = tan^{-1}\left(\frac{G}{F}\right)$$

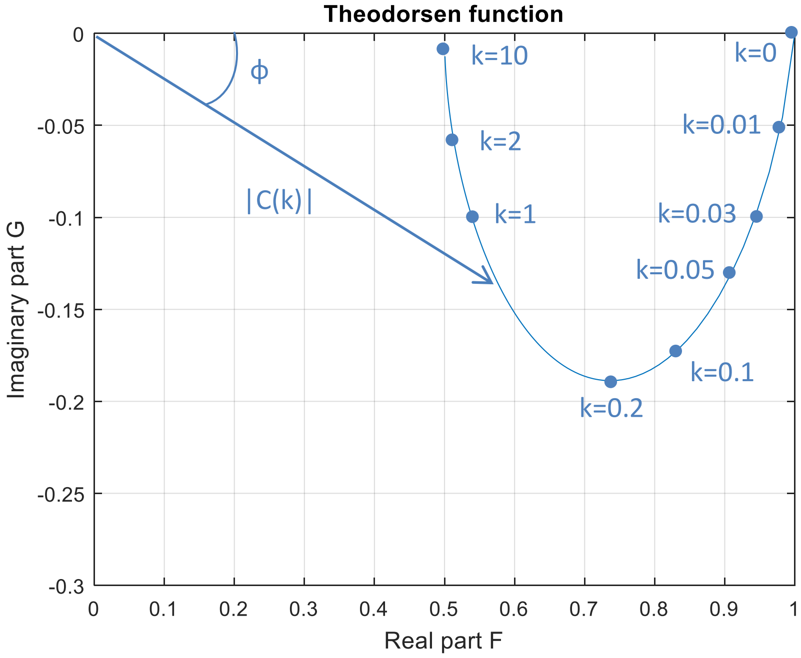

Figure 3.4: Theodorsen's function

As it can be seen in figure 3.4 and also in equations 3.2 and 3.3, Theodorsen's function allows to introduce an amplitude reduction and phase lag effect on the circulatory part in comparison to the quasi-steady conditions. This effect on the lift response can be seen in the following figure 3.5.

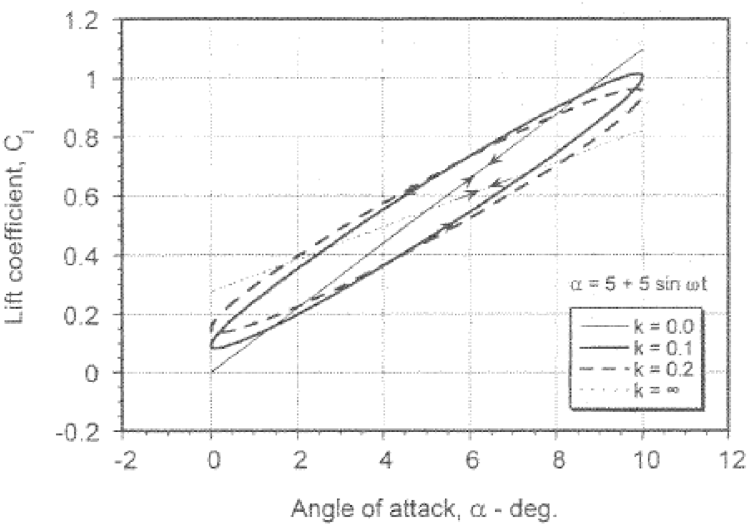

Figure 3.5: Circulatory part of the lift response [3]

For *k*=0, C_l is linearly proportional to α (steady case) and when *k* is increased, the lift plots develop into hysteresis loops and these loops rotate such that the amplitude of the lift response decreases with increasing reduced frequency. If *k* tends to infinity, the circulatory part of the lift amplitude is half and there is not phase lag angle.

If the equations 3.2 and 3.3 are expressed in coefficient form, the result is the following:

$$C_l = \pi b\left[\frac{1}{V^2}\ddot{h} + \frac{1}{V}\dot{\alpha} - \frac{b}{V^2}a\ddot{\alpha}\right] + 2\pi\left[\frac{\dot{h}}{V} + \alpha + \frac{b\dot{\alpha}}{V}\left(\frac{1}{2} - a\right)\right]C(k) \qquad (3.4)$$

$$C_m = -\frac{\pi}{2}\left(\left[\frac{1}{2} - a\right]\frac{b\dot{\alpha}}{V} + \frac{b^2}{V^2}\left[\frac{1}{8} + a^2\right]\ddot{\alpha} - \frac{ab\ddot{h}}{V^2}\right) + \pi\left(a + \frac{1}{2}\right)\left(\alpha + \frac{\dot{h}}{V} + b\left[\frac{1}{2} - a\right]\frac{\dot{\alpha}}{V}\right)C(k) \qquad (3.5)$$

However, these equations 3.4 and 3.5 can be simplified if a particular movement is considered like they are presented in the following subsections.

3.2.1.1 Pure Angle of Attack Oscillations

For this movement, a pure harmonic variation in the angle of attack is considered $\left(\alpha = \bar{\alpha}e^{i\omega t}\right)$. The resultant lift and pitching moment responses are the following:

$$C_l = \frac{L}{\rho V^2 b} = [2\pi(F + iG) + i\pi k]\bar{\alpha}e^{i\omega t} \qquad (3.6)$$

$$C_m = -i\frac{\pi k}{2}\bar{\alpha}e^{i\omega t} \qquad (3.7)$$

In these two last equations, the first term is the circulatory part and the second, the apparent mass contribution. The results of these normalised responses with the variation of the reduced frequency are shown in figures 3.6. and 3.7.

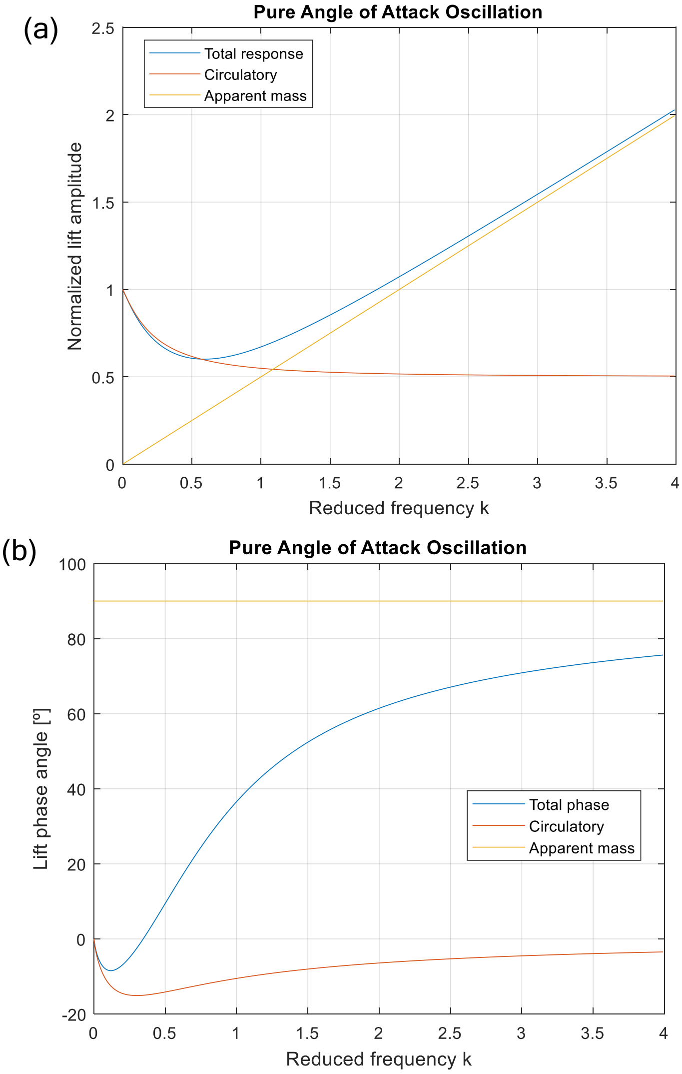

Figure 3.6: Normalised (a) Lift amplitude and (b) Phase of lift for pure angle of attack oscillations

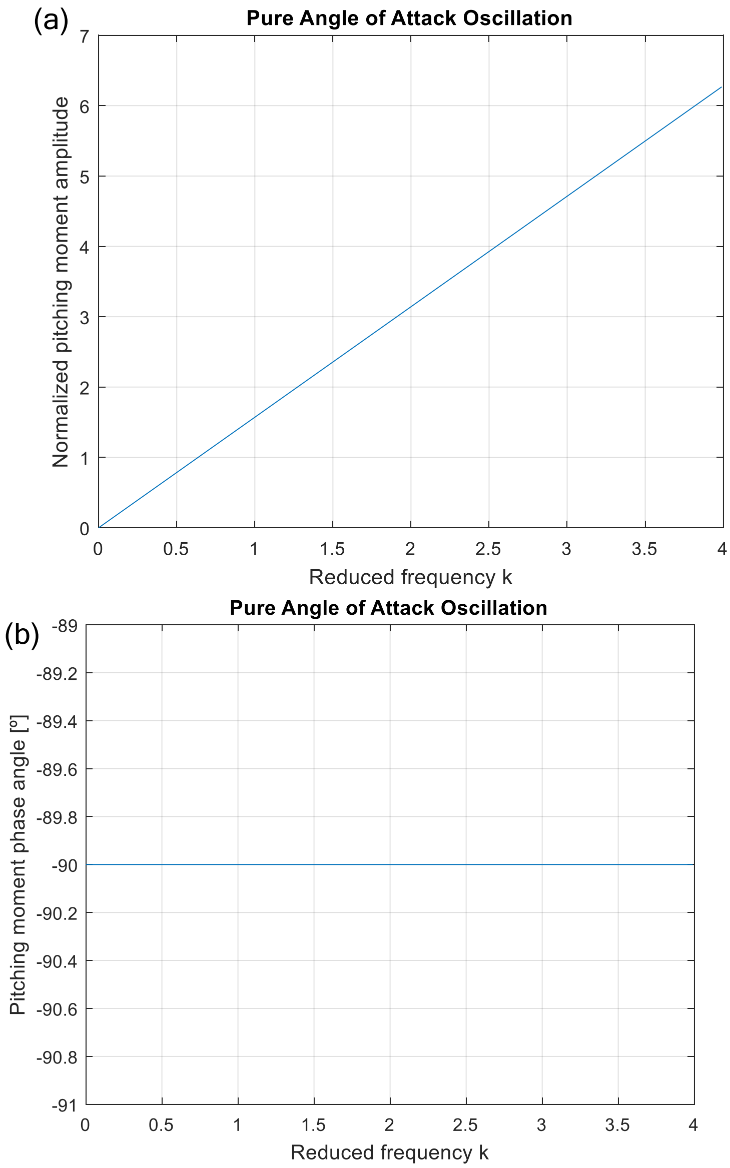

Figure 3.7: Normalised (a) Pitching moment amplitude about ¼-chord and (b) Phase of pitching moment for pure angle of attack oscillations

3.2.1.2 Pure Plunging Oscillations

Now, the blade motion considered is a harmonic plunging movement $\left(h = \bar{h}e^{i\omega t}\right)$ and the results obtained are:

$$C_l = [2\pi k(iF - G) - \pi k^2]\frac{\bar{h}}{b}e^{i\omega t} \qquad (3.8)$$

$$C_m = \frac{\pi}{4}k^2\frac{\bar{h}}{b}e^{i\omega t} \qquad (3.9)$$

As the previous movement, the normalised responses with the variation of the reduced frequency are shown in figures 3.8 and 3.9.

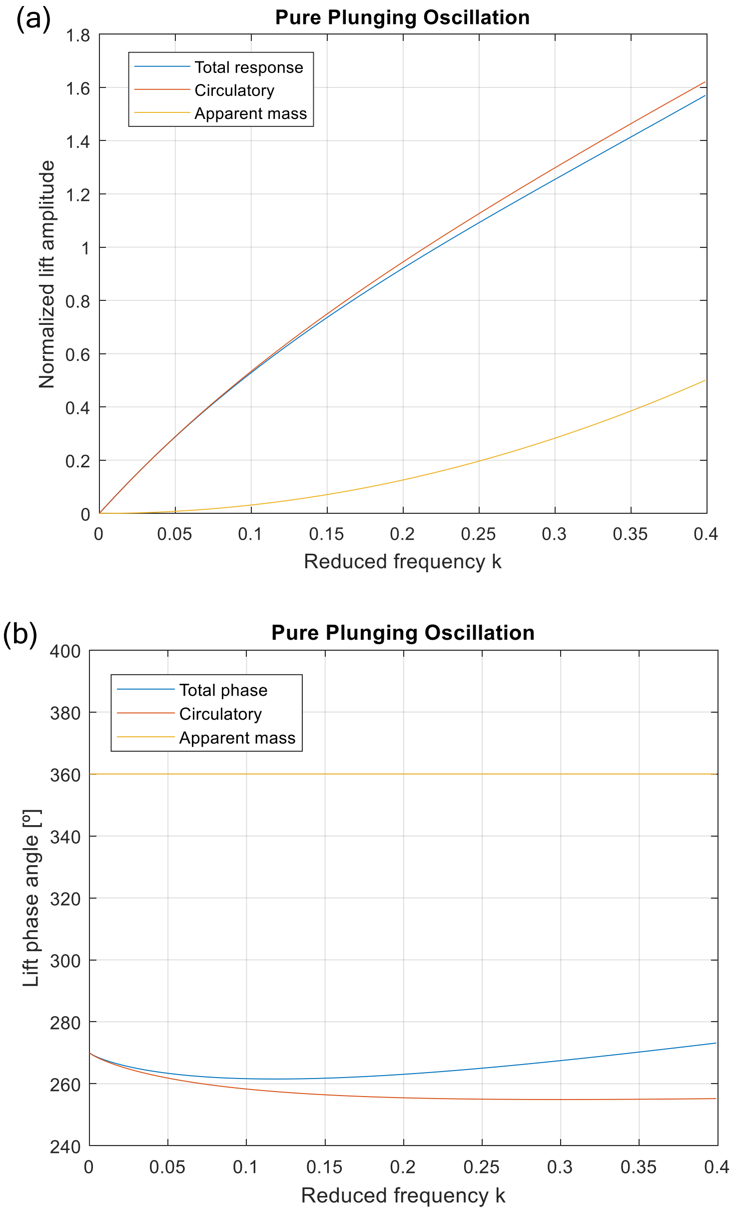

Figure 3.8: Normalised (a) Lift amplitude and (b) Phase of lift for pure plunging oscillations

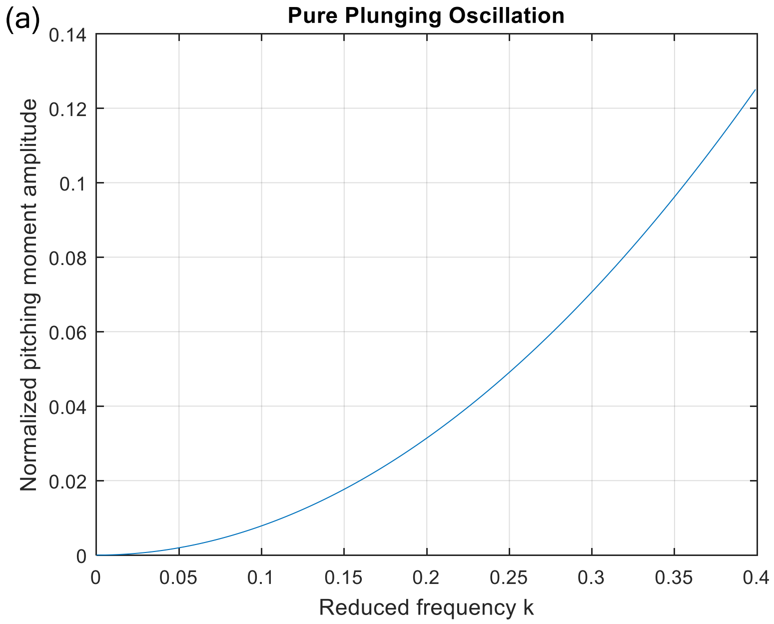

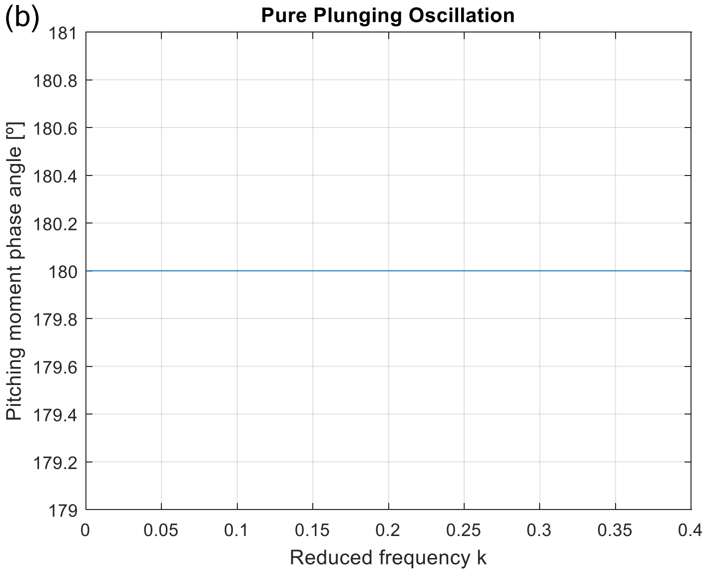

Figure 3.9: Normalised (a) Pitching moment amplitude about ¼-chord and (b) Phase of pitching moment for pure plunging oscillations

3.2.1.3 Pitch Oscillations

For this last motion, a harmonic pitch oscillations are considered where the forcing is now given by $\alpha = \bar{\alpha}e^{i\omega t}$ and the pitch rate by $\dot{\alpha} = i\omega\bar{\alpha}e^{i\omega t}$. So, the responses are:

$$C_l = 2\pi[F(1+ik) + G(i-k)]\bar{\alpha}e^{i\omega t} + \pi k\left(i - \frac{k}{2}\right)\bar{\alpha}e^{i\omega t} \qquad (3.10)$$

$$C_m = \frac{\pi k}{2}\left(\frac{3}{8}k - i\right)\bar{\alpha}e^{i\omega t} \qquad (3.11)$$

Finally, the results are presented in figures 3.10 and 3.11.

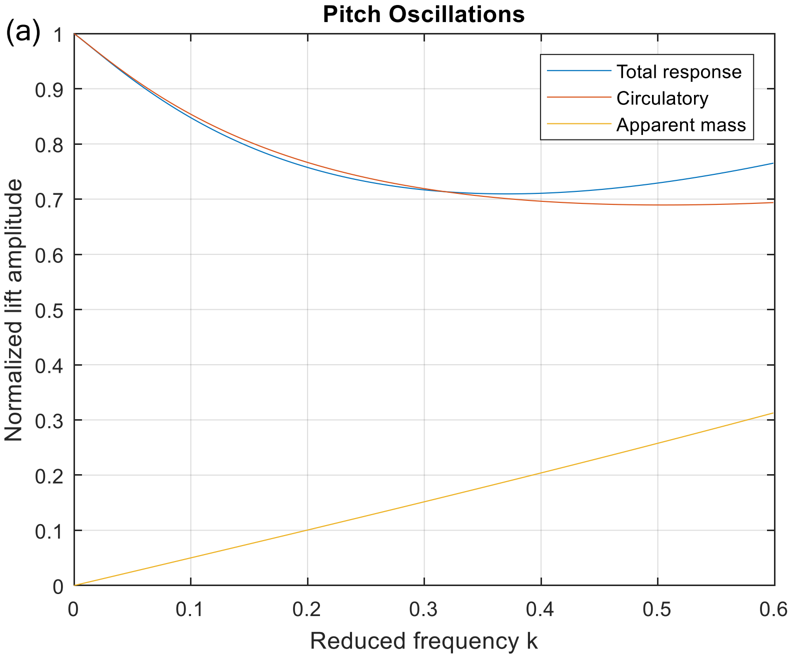

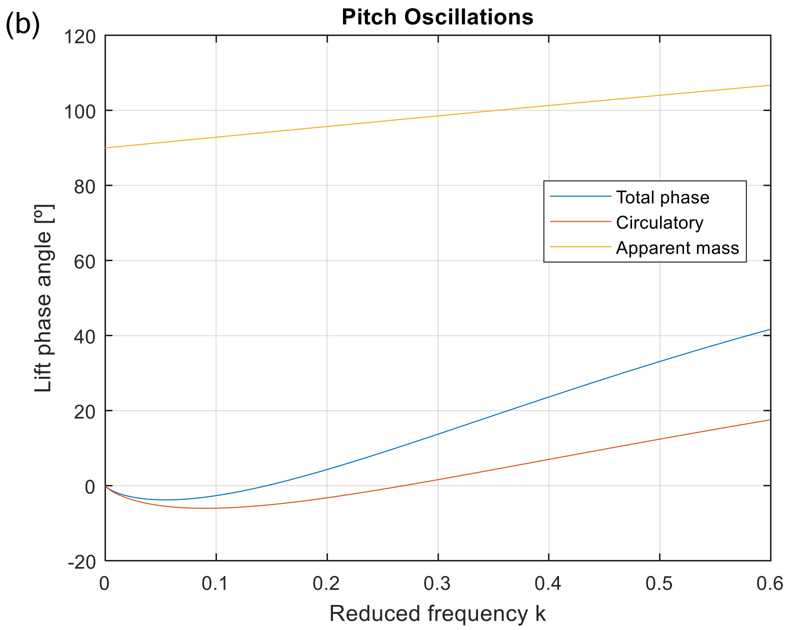

Figure 3.10: Normalised (a) Lift amplitude (b) Phase of lift for pitch oscillations

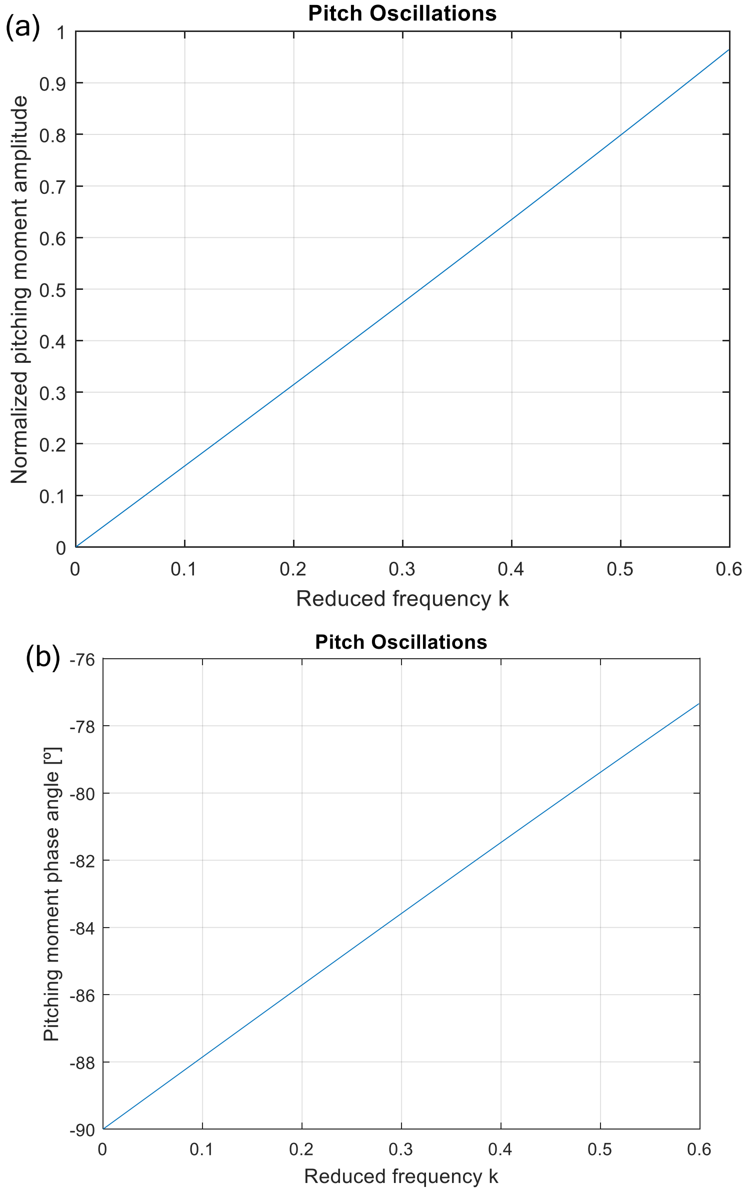

Figure 3.11: Normalised (a) Pitching moment amplitude about ¼-chord and (b) Phase of pitching moment for pitch oscillations

3.2.2 Indicial Response: Wagner's Problem

For a rotor analysis, Theodorsen's theory is somewhats less useful because in a rotor environment, the non-steady value of *V* means that the reduced frequency *k* is an ambiguos parameter. Therefore, a theory formulated in the time domain is more general and usually more useful. Wagner (1925) [3] has obtained a solution for the indicial lift on a thin airfoil undergoing a step change in angle of attack in incompressible flow.

This method is very useful if the indicial aerodynamic response can be determined. Then, it is possible to find the unsteady aerodynamics forces and moments in the time domain as a result of arbitrary variations in angle of attack and/or inflow velocity through the superposition of indicial aerodynamic responses using the Duhamel integral.

However, this method has two problems. The first one is to determine the indicial response functions which are known in incompressible flow but in subsonic compressible flow, they are not known exactly. The second difficulty is that numerical methods must be devised to enable the superposition process to be conducted accurately and efficiently.

The time-varying value of the lift coefficient can be expressed in terms of the Duhamel integral as:

$$C_l(s) = C_{l\alpha}[\alpha(s_0)\,\phi(s) + \int_{s_0}^{s} \frac{d\alpha}{ds}(\sigma)\,\phi(s-\sigma)d\sigma] = C_{l\alpha}\alpha_e(s) \qquad (3.12)$$

where s is the distance traveled by the airfoil in semi-chords, ϕ(s) is the indicial response, also called Wagner's function, to an unit step input of the angle of attack and, by analogy with Theodorsen's function, accounts for the effects of the shed wake, $C_{l\alpha}$ is the lift curve slope and $\alpha_e(s)$ simply represents an effective angle of attack and contains within it all of the time-history effects on the lift due to the shed wake. Moreover, if *V*=constant, then $s = 2Vt/c$.

For solving equation 3.12, it is necessary to use a numerical method for discrete values of time and like this, $\alpha_e(s)$ can be written for a discretely sampled system at times $s = s_0, \sigma_1 \ldots \sigma_2, \sigma_1, s$ as:

$$\alpha_e(s) = \alpha(s_0)\phi(s) + \sum_{i=1}^{\infty} \frac{d\alpha}{ds}(\sigma_i)\phi(s-\sigma_i)\Delta\sigma_i = \alpha(s_0)\phi(s) + \alpha'(\sigma_1)\phi(s-\sigma_1)\Delta\sigma_1 + \alpha'(\sigma_2)\phi(s - \sigma_2)\Delta\sigma_2 + \ldots + \alpha'(\sigma_i)\phi(s-\sigma_i)\Delta\sigma_i + \ldots$$

The problem here is, although the Wagner's function ϕ(s) is known exactly (figure 3.12), its evaluation is not in a convenient simple analytic form. However, there are some alternatives in order to solve the problem.

3.2.2.1 Recurrence Solution to the Duhamel Integral

One solution to the problem is supposing that the Wagner's function takes the form of a general two-term exponentially growing function (figure 3.12), attributed to R.T.Jones (1938,1940) [3]:

$$\phi(s) = 1 - A_1 e^{-b_1 s} - A_2 e^{-b_2 s}$$

where the indicial coefficients take the following values: $A_1 = 0.165$; $A_2 = 0.335$; $b_1 = 0.0455$; $b_2 = 0.3$. It will be noted that $A_1 + A_2 = 0.5$, according to Wagner's exact result. In addition, the exponential approximation has the main advantage of having a simple Laplace transform and although the exponential behaviour of the Wagner's function is not an exact representation of the physical behavior, it is usually sufficiently accurate for practical calculations.

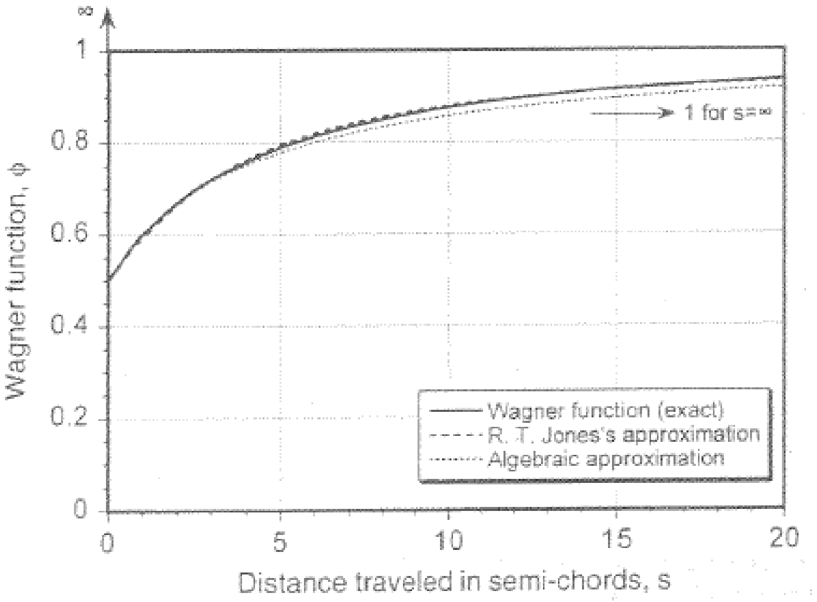

Figure 3.12: Wagner's function and approximations [3]

Thanks to this, the Duhamel integral from equation 3.12 can be expressed as:

$$\alpha_e(s) = \alpha(s_0)\left(1 - A_1 e^{-b_1 s} - A_2 e^{-b_2 s}\right) + \int_{s_0}^{s} \frac{d\alpha}{ds}(\sigma)\left(1 - A_1 e^{-b_1 s} - A_2 e^{-b_2 s}\right) d\sigma$$

Moreover, the terms $A_1\alpha(s_0)e^{-b_1 s}$ and $A_2\alpha(s_0)e^{-b_2 s}$ can be neglected because they are short-term transients containing only the initial value of α. Finally, the Duhamel integral can be written in compact form as $\alpha_e(s) = \alpha(s) - X(s) - Y(s)$ where the X and Y terms are given by:

$$X(s) = A_1 \int_{s_0}^{s} \frac{d\alpha}{ds}(\sigma) e^{-b_1(s-\sigma)} d\sigma \quad ; \quad Y(s) = A_2 \int_{s_0}^{s} \frac{d\alpha}{ds}(\sigma) e^{-b_2(s-\sigma)} d\sigma$$

After some calculations and using the rectangle rule of integration, the resultant formulas are the followings:

$$X(s) = X(s - \Delta s)e^{-b_1 \Delta s} + A_1 \Delta\alpha_s \quad ; \quad Y(s) = Y(s - \Delta s)e^{-b_2 \Delta s} + A_2 \Delta\alpha_s$$

This form of X and Y terms is named as one-step recursive formulas or Algorithm D-1. These recursive functions contain all the time history information of the unsteady aerodynamics and are simply updated once at each time step. The relative error in this algorithm is $\epsilon = 2 - \frac{b_1 \Delta s}{1 - e^{-b_1 \Delta s}} - \frac{b_2 \Delta s}{1 - e^{-b_2 \Delta s}}$. In order to obtain low errors, a relatively small time step is needed. If it is not possible and in order to minimize the error, another approximation can be done using the midpoint rule. Therefore, this new method produced the Algorithm D-2:

$$X(s) = X(s - \Delta s)e^{-b_1 \Delta s} + A_1 \Delta\alpha_s e^{-b_1 \Delta s/2} \quad ; \quad Y(s) = Y(s - \Delta s)e^{-b_2 \Delta s} + A_2 \Delta\alpha_s e^{-b_2 \Delta s/2}$$

Now, the relative error is $\epsilon = 2 - \frac{b_1 \Delta s e^{-b_1 \Delta s/2}}{1 - e^{-b_1 \Delta s}} - \frac{b_2 \Delta s e^{-b_2 \Delta s/2}}{1 - e^{-b_2 \Delta s}}$. However, while the above mentioned methods have seen some previous use in comprehensive rotor analyses, other methods based on the trapezoidal rule or Simpson's rule can also be used. Using Simpson's rule, the Algorithm D-3 is obtained:

$$X(s) = X(s - \Delta s)e^{-b_1 \Delta s} + \frac{A_1}{6}\Delta\alpha_s\left(1 + 4e^{-\frac{b_1 \Delta s}{2}} + \; e^{-b_1 \Delta s}\right)$$

$$Y(s) = Y(s - \Delta s)e^{-b_2 \Delta s} + \frac{A_2}{6}\Delta\alpha_s(1 + 4e^{-\frac{b_2 \Delta s}{2}} + \; e^{-b_2 \Delta s})$$

The new relative error is $\epsilon = 2 - \frac{b_1 \Delta s\left(1+4e^{-\frac{b_1 \Delta s}{2}}+e^{-b_1 \Delta s}\right)}{6\left(1-e^{-b_1 \Delta s}\right)} - \frac{b_2 \Delta s(1+4e^{-\frac{b_2 \Delta s}{2}}+e^{-b_2 \Delta s})}{6\left(1-e^{-b_2 \Delta s}\right)}$.

3.3 Inflow Dynamic Analysis

The goal of this section is to define different inflow models which are going to be used in order to predict and analyse the aerodynamics of the cyclocopter. First, the hover situation is going to be covered and next, the forward flight.

3.3.1 Hover Flight

In this subsection, two inflow models are going to be defined for approximating the hover situation. These two inflow models are based on blade momentum theory and are the followings:

- Single Streamtube Model (SS) [1]: The entire rotor is immersed in a unique streamtube (figure 3.13 (a)).

- Double-Multiple Streamtube Model (DS) [4]: The rotor is divided into a number of streamtubes and the influence of the upper half of the rotor on the lower half is taken into account (figure 3.13 (b)).

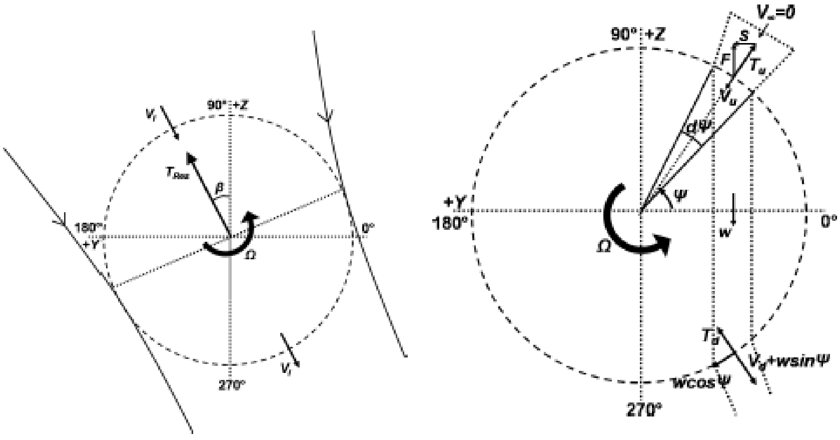

Figure 3.13: (a) Single Streamtube Inflow (b) Double-Multiple Streamtube Inflow [1]

3.3.1.1 Single Streamtube Model

The final result of the models is the blade aerodynamic loads (lift and drag). So, the first step is the calculation of the section angle of attack which has two components: the wind velocity $(\vec{V}_w)$ from rotor inflow and the blade velocity at the ¾ chord location $(\vec{V}_b)$ relative to the hub fixed frame:

$$\vec{V} = -\vec{V}_w + \vec{V}_b = V_x\vec{\imath} + V_y\vec{\jmath} + V_z\vec{k}$$

Moreover, these two terms can be decomposed in:

$$\vec{V}_w = V_{wx}\vec{\imath} + V_{wy}\vec{\jmath} + V_{wz}\vec{k}$$

$$V_{wx} = 0 \;\; ; \;\; V_{wy} = -v_i\cos(\Psi - \beta) \;\; ; \;\; V_{wz} = -v_i\sin(\Psi - \beta)$$

where *Ψ* is the azimuth angle, *β* is the direction of the resultant thrust and v_i is the inflow velocity.

These two last parameters, as well as the thrust force *T*, are defined by the following expressions:

$$v_i = \sqrt{\frac{\kappa T}{2\rho A}} \quad ; \quad \beta = tan^{-1}\left(\frac{F_Y^A}{F_Z^A}\right) \quad ; \quad T = \sqrt{F_Z^2 + F_Y^2}$$

where *A* is the blade area, $F_Z^A$and $F_Y^A$are the aerodynamic forces in the non-rotating inertial frame which are the final result of the problem. So, it is necessary to make an iterative process in order to use the final solution to obtain these two variables and solve again the problem with the correct values. Moreover, *κ* is a correction factor from the inflow and it is assumed to be 1.15 which is a typical value as it is indicated in reference [1]. Continuing now with the blade velocities expressions:

$$\vec{V}_b = V_{bx}\vec{\imath} + V_{by}\vec{\jmath} + V_{bz}\vec{k}$$

$$V_{bx} = -(\dot{v}' + w'\dot{\theta}_1)\eta_r\cos(\theta_1) - (\dot{w}' - v'\dot{\theta}_1)\eta_r\sin(\theta_1)$$

$$V_{by} = \dot{v} - \eta_r\sin(\theta_1)\dot{\theta}_1 + \Omega(w + \eta_r\sin(\theta_1) + R)$$

$$V_{bz} = \dot{w} + \eta_r\cos(\theta_1)\dot{\theta}_1 - \Omega(v + \eta_r\cos(\theta_1))$$

where *v* is the tangential bending, *w* is the radial bending, $\theta_1 = \theta + \phi$ (θ is the pitch angle and ϕ is the elastic twist), *Ω* is the rotation velocity, *R* is the rotor radius and if the blade is pitching at ¼-chord, $\eta_r = -0.5c$ (c is the blade chord).

However, the velocities are needed to be expressed in the deformed frame in order to calculate the blade section loads. Therefore, the rotation matrix from undeformed to deformed frame is:

$$T_{DU} = \begin{bmatrix} 1 - \frac{v'^2}{2} - \frac{w'^2}{2} & v' & w' \\ -v'\cos(\theta_1) - w'\sin(\theta_1) & \left(1 - \frac{v'^2}{2}\right)\cos(\theta_1) - v'w'\sin(\theta_1) & \left(1 - \frac{w'^2}{2}\right)\sin(\theta_1) \\ v'\sin(\theta_1) - w'\cos(\theta_1) & -\left(1 - \frac{v'^2}{2}\right)\sin(\theta_1) - v'w'\cos(\theta_1) & \left(1 - \frac{w'^2}{2}\right)\cos(\theta_1) \end{bmatrix}$$

Applying this rotation, the new velocities obtained are the followings that can be seen in figure 3.14:

$$\begin{bmatrix} U_X \\ U_T \\ U_P \end{bmatrix} = T_{DU}\begin{bmatrix} V_x \\ V_y \\ V_z \end{bmatrix}$$

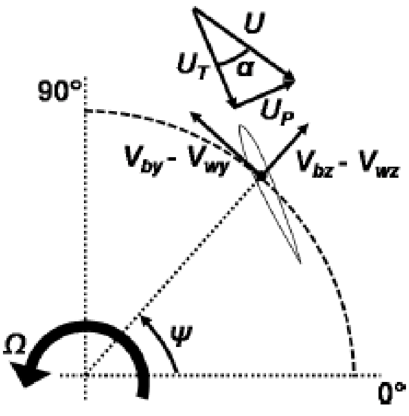

Figure 3.14: Velocities in the deformed and undeformed frames [1]

where $\alpha = tan^{-1}\left(\frac{U_P}{U_T}\right)$ is the angle of attack and $U = \sqrt{U_P^2 + U_T^2}$ is the deformed frame velocity magnitude.

In order to solve the aerodynamic of the cyclocopter and take into account the unsteady effects, the indicial response method explained in section 3.2.2 is going to be used.

Moreover, the same exponential approximation for the Wagner function is used:

$$\phi(s) = 1 - A_1 e^{-b_1 s} - A_2 e^{-b_2 s}$$

where $A_1 = 0.165, A_2 = 0.335, b_1 = 0.0455\ and\ b_2 = 0.3$ which are approximated values of the coefficients obtained from reference [3].

The sectional lift coefficient can be decomposed in circulatory and non-circulatory components.

$$C_l = C_l^c + C_l^{nc}$$

The circulatory component of the lift has the contribution from both angle of attack (α) and pitch rate (q). The same Wagner function is used for both contributions. The Duhamel integral is solved following the steps explained in section 3.2.2.1 and it is used the Algorithm D-1:

$$X_\alpha(s) = X_\alpha(s - \Delta s)e^{-b_1 \Delta s} + A_1 \Delta\alpha_s \quad ; \quad Y_\alpha(s) = Y_\alpha(s - \Delta s)e^{-b_2 \Delta s} + A_2 \Delta\alpha_s$$

$$X_q(s) = X_q(s - \Delta s)e^{-b_1 \Delta s} + A_1 \Delta q_s \quad ; \quad Y_q(s) = Y_q(s - \Delta s)e^{-b_2 \Delta s} + A_2 \Delta q_s$$

Due to this formulation, it is necessary to define the effective angle of attack(α_e) and the effective pitch rate (q_e) which have the time history effects:

$$\alpha_e = \alpha - X_\alpha(s) - Y_\alpha(s) \quad ; \quad q_e = q - X_q(s) - Y_q(s)$$

Therefore, the circulatory and non-circulatory components are expressed as:

$$C_l^c = C_{l\alpha}\alpha_c + \frac{1}{2}C_{l\alpha}q_e \quad ; \quad C_l^{nc} = \frac{\pi}{2U}c\dot{\alpha} - \frac{\pi}{4}\left(\frac{c}{U}\right)^2 a\ddot{\alpha}$$

where *a = -0.5* (the pitching axis is at ¼-chord) and $C_{l\alpha} = 0.11$ according to experimental studies from reference [5]. However, a finite span correction is applied to the $C_{l\alpha}$ using twice the aspect ratio $AR = b^2/A$. The aim is to take into account the blade attachment and end-plates which partially covers the blade tips.

$$C_{l\alpha finite} = \frac{C_{l\alpha}}{1 + \frac{C_{l\alpha}}{2AR\pi}}$$

In relation to the total drag coefficient, this is given by the sum of profile C_{d0} and induced drag C_{di} components:

$$C_d = C_{d0} + C_{di}$$

The sectional profile drag is approximated by the following expression:

$$C_{d0} = d_0 + d_1\alpha + d_2\alpha^2$$

where $d_0 = 0.0334, d_1 = 0$ (symmetric airfoil) and $d_2 = 2.511$ obtained thanks to a 2-D CFD study according to reference [1].

The induced drag is given by:

$$C_{di} = \frac{C_l^2}{\pi 2ARe}$$

where *e* is the Oswald's efficiency factor and it is assumed to be 0.85 which is a typical value according to reference [1].

The next step is to calculate the forces in the deformed frame. The normal and chordwise forces are given as:

$$F_n^A = 0.5\rho U^2 c(C_l cos\alpha + C_d sin\alpha) \quad ; \quad F_c^A = 0.5\rho U^2 c(C_l sin\alpha - C_d cos\alpha)$$

The force in the spanwise direction $F_x^A = 0$ is ignored. Like it is done with the velocities, it is necessary to rotate the forces but now from the deformed frame to the undeformed frame.

$$\begin{bmatrix} F_u^A \\ F_v^A \\ F_w^A \end{bmatrix} = T_{DU}^T \begin{bmatrix} F_x^A \\ F_c^A \\ F_n^A \end{bmatrix}$$

Therefore, the aerodynamic forces in the non-rotating inertial frame are given by:

$$F_Z^A = F_w^A sin\Psi + F_v^A cos\Psi \quad ; \quad F_Y^A = -F_w^A cos\Psi + F_v^A sin\Psi$$

Finally, the power consumed is given by:

$$P = M\Omega$$

where Ω is the rotation speed and M is the aerodynamic moment whose expression is the following one:

$$M = \sum_{i=1}^{N_b} \left(F_{Yi}^A R cos(\Psi_i) + F_{Zi}^A R cos(\Psi_i) \right)$$

3.3.1.2 Double-Multiple Streamtube Model

Like it was explained in the introduction of section 3.3, this analytical method uses a multiple-streamtube model divided into two parts: one for the upstream half-cycle of the rotor and the other for the downstream half-cycle (figure 3.15).

In this way, each streamtube intersects the blades' path twice, once on the upstream pass and again on the downstream pass. For the problem, the flow through the rotor is considered to be one dimensional, quasi-steady, incompressible and inviscid and the cyclorotor is idealised as an infinitesimally thin actuator cylinder over which a pressure difference between inner and outer surface exits. Therefore, the two halves of the cycle are going to be analysed separately but also take into account the interaction between them.

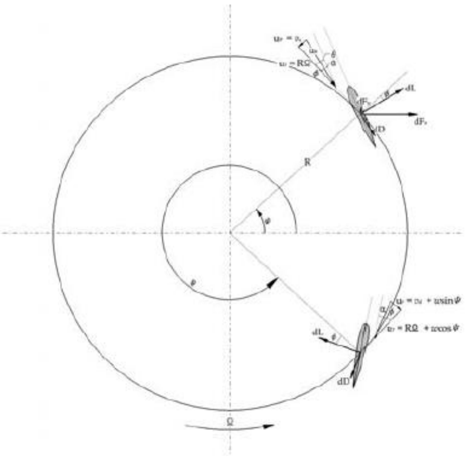

Figure 3.15: Flow environment of the Double-Multiple Streamtube Model [4]

Upstream half of the rotor $(\mathbf{0} \leq \boldsymbol{\Psi} \leq \boldsymbol{\pi})$

From the momentum and energy conservation laws in each streamtube, the element thrust in the upper half can be expressed as:

$$dT_u = 2\rho R\left(\frac{v_u}{sin\Psi}\right)^2 d\Psi \qquad (3.13)$$

where v_u is the induced velocity in the upstream half of the rotor.

Moreover for a rotor with N_b identical blades (with c as blade chord and $C_{l\alpha}$ as lift curve slope), the resultant incremental lift and drag per unit span on a blade element are, using the momentum theory:

$$dL = \frac{1}{2}\rho U_R^2\left(\frac{N_b d\Psi}{2\pi}\right)cC_l \quad ; \quad dD = \frac{\rho N_b c}{4\pi}U_R^2 C_d d\Psi$$

where U_R is the resultant velocity. So, the element thrust in the upper part of the rotor is:

$$dT_u = dLcos\phi - dDsin\phi \qquad (3.14)$$

Equating equations 3.13 and 3.14, the following expression is obtained:

$$4\kappa_{emp}\lambda^2 = \sigma C_{l\alpha}(1+\lambda^2)[(\theta-\phi)cos\phi - \frac{C_d}{C_{l\alpha}}sin\phi]sin^2\Psi \qquad (3.15)$$

where σ is the blade solidity, ϕ is the relative inflow angle, θ is the pitch angle, κ_{emp} is an empirical factor to take into account non-uniform flow, 3-D effects, tip losses, etc... and it is assumed to be 1.15 according to reference [4]. Thanks to equation 3.15, the constant λ can be found which is necessary to obtain the velocities and forces of the problem.

The resultant local flow velocity at any blade element has a perpendicular component U_P normal to the rotor as a result of the induced inflow and a tangential component U_T parallel to the rotor due to the blade rotation. The equations which define these velocities are:

$$U_P = v_u = \lambda R\Omega \quad ; \quad U_T = R\Omega$$

Therefore, the resultant velocity U_R and the relative inflow angle ϕ at the blade element are:

$$U_R = \sqrt{U_T^2 + U_P^2} \quad ; \quad \phi = tan^{-1}\left(\frac{U_P}{U_T}\right)$$

In addition, the effective angle of attack is $\alpha = \theta - \phi$ where θ is the pitch angle. Finally, the far downstream velocity of the upstream half w can be obtained thanks to the following equation:

$$w = \frac{2v_u}{sin\Psi} \qquad (3.16)$$

Downstream half of the rotor $(\boldsymbol{\pi} \leq \boldsymbol{\Psi} \leq \mathbf{2}\boldsymbol{\pi})$

Like it was done in the upstream half, applying the momentum and energy conservation laws to the lower actuator disk, the element thrust produced is:

$$dT_d = 2\rho R v_d\sqrt{w^2 + 2wv_d sin\Psi + v_d^2}\; d\Psi \qquad (3.17)$$

where v_d is the induced velocity in the downstream half of the rotor.

Now, the perpendicular and tangential components of the resultant local flow velocity are given by:

$$U_T = R\Omega + wcos\Psi \quad ; \quad U_P = wsin\Psi + v_d$$

where the far downstream velocity w is obtained from equation 3.16 thanks to the upper half.

The equations which define the lift and drag coefficients are the same as the upper half changing only the value of the resultant velocity U_R. Therefore, using equations 3.14 and 3.17, it is found that:

$$4(\lambda - \varsigma \, tan\Psi)\sqrt{\lambda^2 + \varsigma^2} = \sigma[(1+\varsigma)^2 + \lambda^2][C_{l\alpha}(\theta - \phi)cos\phi - C_d sin\phi] \quad (3.18)$$

where $\varsigma = \frac{wcos\Psi}{R\Omega}$ and the values of w are given by equation 3.16 because for this downstream half, w is considered as an input condition of the flow at each streamtube defined in the upper half. Moreover, thanks to equation 3.18, the induced velocity in the downstream half of the rotor can be obtained using the constant λ:

$$v_d = \lambda R\Omega - wsin\Psi$$

Since the velocities in both up and down halves of the rotor are obtained, the lift and drag coefficients are calculated choosing one of the unsteady models of section 3.2 or the steady case obtaining the values thanks to reference [5]. Therefore, the next step is to determine the forces and the power consumed. Therefore, the radial and tangential forces are:

$$F_R = L\, cos\phi - D\, sin\phi \quad ; \quad F_T = L\, sin\phi + D\, cos\phi \quad (3.19)$$

In order to obtain the total thrust produced on a rotor with N_b blades, the horizontal and vertical forces can be obtained using the previous radial and tangential forces defined.

$$F_X = \frac{N_b}{2\pi}\int_0^{2\pi}(F_R cos\Psi + F_T sin\Psi)d\Psi \quad ; \quad F_Y = \frac{N_b}{2\pi}\int_0^{2\pi}(F_R sin\Psi - F_T cos\Psi)d\Psi \quad (3.20)$$

The torque about the axis of rotation (Q) has two components. One is due to the tangential force which is composed of the profile drag and the induced drag. The other is an additional torque arising from maintaining the oscillation of the blade per revolution. Hence, the total torque is given by:

$$Q = \frac{N_b}{2\pi}\left(\int_0^{2\pi} RF_T d\Psi - \frac{M\dot{\alpha}}{\Omega}\right) \quad (3.21)$$

Therefore, the total thrust produced and the power required can be obtained by the followings equations:

$$T = \sqrt{F_X^2 + F_Y^2} \quad ; \quad P = Q\Omega \quad (3.22)$$

3.3.2 Forward Flight

This simplified numerical model used to approximate the forward flight is explained thanks to reference [2]. It is obtained by simple Cartesian vector analysis and the application of the Pythagorean theorem to the triangles which are represented in figure 3.16.

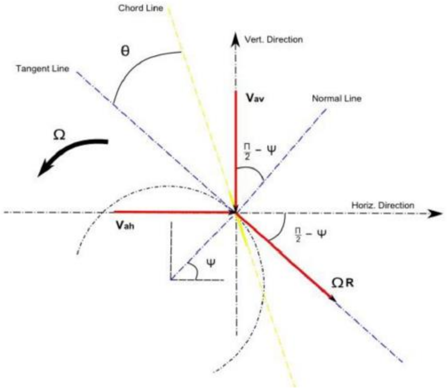

Figure 3.16: Forward motion kinematic analysis [2]

Therefore, the equations obtained according to figure 3.16 and which bring up a primary analysis method for the forward motion are the following ones:

$$V_T = \Omega R + V_h \sin(\Psi) + V_v \cos(\Psi) \qquad (3.23)$$

$$V_N = V_h \cos(\Psi) - V_v \sin(\Psi) \qquad (3.24)$$

$$\gamma = arctan\left(\frac{V_N}{V_T}\right) \quad ; \quad V_R = \sqrt{V_T^2 + V_N^2} \quad ; \quad \theta_a = \gamma + \theta$$

where V_T and V_N are the velocity tangential and normal components respectively, V_h and V_v are the horizontal and vertical advance velocities respectively, γ is the resultant velocity slope in relation to the tangential axis and θ_a is the angle of attack for each blade in forward motion. The different types of motion (forward, backward, upward and downward) can be studied thanks to the values of V_h and V_v.

As it happened in the DS code for hover case, the lift and drag coefficients calculation follows the same procedure and the forces and the power consumed are obtained from equation 3.19 to 3.22.

Chapter 4

Hover Flight Analyses

In this new chapter, the codes which have been developed for the hover situation are going to be explained. These codes have been done with Matlab using the different expressions which were shown in the last chapter. Finally, the results of the codes are going to be presented as well as be compared with experimental values in order to validate the codes.

4.1 Numerical Models

The aim of this section is to explain the numerical codes developed using the equations and expressions explained in sections 3.2 and 3.3 for the next two inflow models:

- Single Streamtube (SS) Code.
- Double-Multiple Streamtube (DS) code.

4.1.1 Initial Parameters

First of all, it is necessary to define what are the initial parameters which have to be defined in order to start with the codes. These initial parameters are:

- Blade chord *(c).*
- Blade radius *(R).*
- Blade span *(b).*
- Number of blades (N_b).
- Maximum pitch amplitude (θ_0).
- Rotation speed (Ω).

Like the blades of cyclocopter are assumed to be rigid, the blade deformation parameters (v, the tangential bending, w, the radial bending and ϕ, the elastic twist) which appear in the balde velocity equations are null.

In addition, one of the previous parameter can be varied in order to see its effect on the performance of the cyclocopter and show like this, the evolution of variables as velocities, forces, power...

4.1.2 Single Streamtube Code

When the initial parameters are defined, the first step is to obtain the wind and blade velocities (V_{wy}, V_{wz}, V_{by}, V_{bz}) in the rotating undeformed coordinate system as well as the resultant velocities (V_y, V_z). For doing this, it is necessary to initialise the induced velocity v_i with values near to zero and vary it since the convergence is achieved. The same occurs with the variable β which, at zero azimuth angle, is supposed to be null.

Next step is to rotate the undeformed frame velocities to the deformed frame velocities (U_T,U_P) using the rotation matrix T_{DU}. Moreover, thanks to these new velocities, the angle of attack (α) and the modulus of the resultant velocity *(U)* can be obtained.

Before calculating the forces, the lift and drag coefficients need to be defined. In relation to the lift coefficient, there are different ways to calculate it:

- Steady case: If the steady case is considered, the lift coefficient can be obtained directly from Xfoil which is a program that allows to obtain the curves with the evolution of the coefficients versus the angle of attack [7]. Moreover, this procedure can be also applied to obtain the drag coefficient.

- Unsteady case: If the previous case is not possible because the unsteady effects are not negligible, an unsteady model needs to be used. In this thesis, the two unsteady models which are going to be used are Theodorsen and Duhamel (both were explained in section 3.2).

If Theodorsen's theory (section 3.2.1) is selected, first the reduced frequency *(k)* is calculated. So, an angular frequency (ω) need to be supposed in order to obtain k from equation 3.1 where the flow velocity is now $V = \Omega R$.

With this reduced frequency, functions F and G can be calculated and finally, the lift coefficient selecting one of the three cases shown in section 3.2.1 (angle of attack, plunging or pitch oscillations).

On the other hand, if Duhamel model (section 3.2.2) is chosen, the time step *(t)* and the reduced time *(s)* are fixed using the following equations:

$$t = \frac{\Psi}{\Omega} \quad ; \quad s = \frac{2}{c} U t \qquad (4.1)$$

Therefore, these two variables are defined each azimuthal position as well as their increments ($\Delta t = t - t_{ant}$ and $\Delta s = s - s_{ant}$). Moreover, $\dot{\alpha}$ and $\ddot{\alpha}$ are assumed to be zero at first. Finally, one of the three algorithms (D-1, D-2 or D-3) is selected and with it, the coefficients X_α, Y_α, X_q and Y_q and the lift coefficient are calculated.

In relation to the drag coefficient, the way to calculate it is explained in section 3.1.1.

The final step is to determine the forces, first in the deformed frame (F_n and F_c) and next, in the undeformed frame (F_v and F_w). So, the aerodynamic forces can be calculated as well as the resultant thrust and the parameter β. This resultant thrust *(T)* is again used to obtain the induced velocity v_i and another iteration of the code is done (using also the new value of β obtained) until the convergence of T is achieved. This is done when the difference between two consecutive values of T is less than a certain tolerance.

When the convergence is achieved, a new azimuthal position is assumed until all the 360º are covered following always the same procedure.

4.1.3 Double-Multiple Streamtube Code

The main difference between this code and the previous one is that now the cycle is divided into an upper and lower parts like it was explained in section 3.3.2. Therefore, the upper half needs to be solved first in order to solve next the lower part.

Upstream half of the rotor ($0 \leq \Psi \leq \pi$)

For each azimuthal position, the equation 3.14 is solved obtaining the value of λ. For doing this, the relative inflow angle ϕ is initialised as zero and a drag coefficient is assumed. Thanks to the value of λ obtained, the velocities (U_p and U_t) can be calculated as well as the resultant velocity, the angle of attack and the new value of the relative inflow angle.

In relation to obtain the lift and drag coefficients, the procedure is the same as it was explained in the Single Streamtube code. This cycle is iterated until the convergence of the relative inflow angle is achieved.

Next step is to determine the induced velocity (v_u) and the far downstream velocity of the upstream half *(w)* for each azimuthal position considered.

Downstream half of the rotor ($\pi \leq \Psi \leq 2\pi$)

For the first azimuthal position, the last values of the upstream half are used to initialise the relative inflow angle and the drag coefficient for this downstream half. With these values and the variable τ which can be also determined using the values of w which were calculated in the upstream part for each streamtube created, the equation 3.17 is solved and with it, the value of λ is obtained. Like it was done in the upstream half, the velocities, angle of attack, relative inflow angle and the induced velocity (v_d) in the downstream half are calculated as well as the lift and drag coefficients. This cycle is again run until the convergence in the code is obtained and for all azimuthal positions.

When all the cycle is solved, the next step is to determine the forces using the equations which appear in section 3.3.2. With them, the resultant thrust can be obtained and the problem is solved.

4.2 Models Validation

The first step which is necessary to do everytime a model is developed is to validate it. The aim of this is to show if the model can approximate and adapt well to the reality. In order to make it possible, the results obtained from the model are compared with experiments. Two subsections are going to be presented using two different ways to vary the pitch angle: one considering a sinusoidal variation and the other with the four-linkage mechanism explained in section 2.4.2.

4.2.1 Sinusoidal Pitch Angle Variation

Sinusoidal Pitch Angle Variation

The sinusoidal variation of the pitch angle along the azimuthal position is expressed by the following equation:

$$\theta = \theta_0 \sin(\Psi)$$

where θ_0 is the amplitude of the sine and so, the maximum value of the pitch angle. In particular, the experimental results used in this subsection are extracted from references [1] and [4] and their values are obtained using the web [6].

The performance parameters that define the geometry of the cyclocopter and which are used to obtain the following graphs are shown in table 4.1, 4.2 and 4.3, respectively. In the first two figures 4.1 and 4.2, the results obtained from the two inflow models developed (section 3.3) are compared with experiments extracted from reference [4]. Moreover, the two unsteady theories explained in section 3.2 are used and the solution obtained with each of them is also shown in the figures.

Table 4.1: Geometry of cyclocopter used in figure 4.1

Characteristic	*c* (m)	*R* (m)	*b* (m)	N_b	θ_0
	0.15	0.4	0.8	6	15º

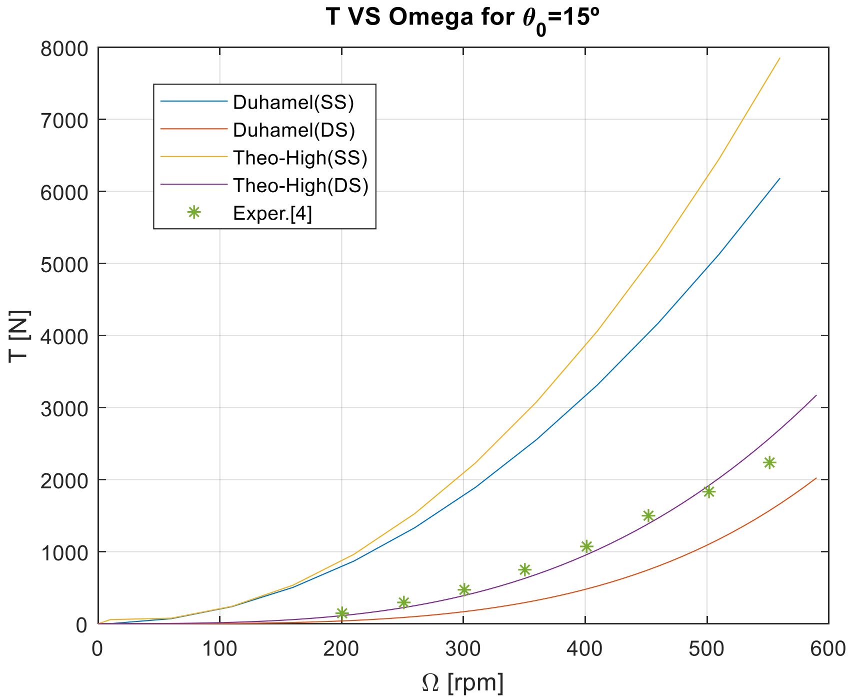

Figure 4.1: Resultant Thrust *(T)* VS Rotation Speed (*Ω*) for maximum pitch amplitude of θ_0= 15º

Table 4.2: Geometry of cyclocopter used in figure 4.2

Characteristic	*c* (m)	*R* (m)	*b* (m)	N_b	*Ω*(rpm)
	0.15	0.4	0.8	6	300

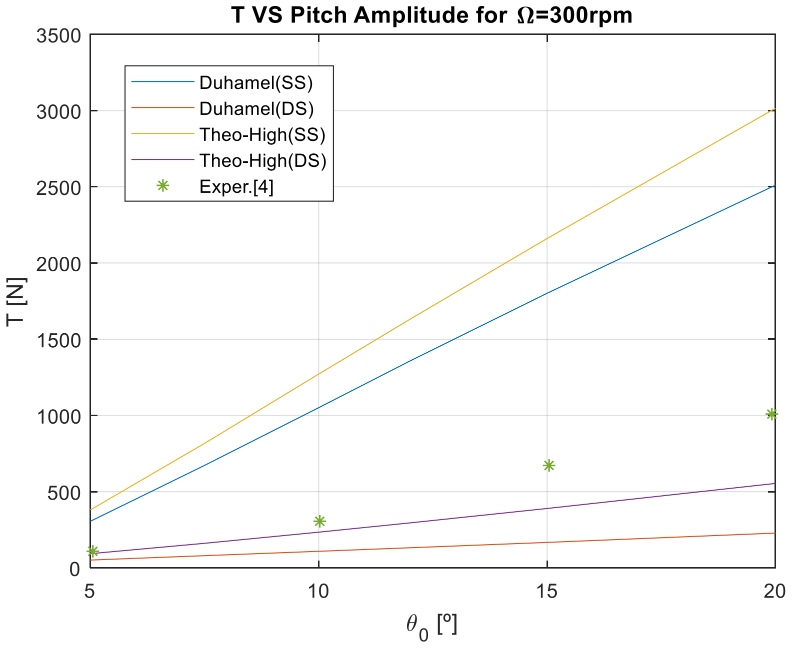

Figure 4.2: Resultant Thrust *(T)* VS Pitch amplitude (θ_0) for rotation speed of Ω=300rpm

As it can be seen in the previous figures, the Double-Multiple Streamtube model (DS) using Theodorsen's theory with high unsteady effects is the model which adapts better to the experimental values. Moreover, this adaptation to experiments is better when the rotation speed (Ω) is varied than when the pitch angle amplitude (θ_0) is modified.

Now, the experimental values from reference [1] are compared using the geometric parameters which appear in table 4.3.

Table 4.3: Geometry of cyclocopter used in figure 4.3

Characteristic	c (m)	R (m)	b (m)	N_b	θ_0
	0.0254	0.077	0.1524	3	25º

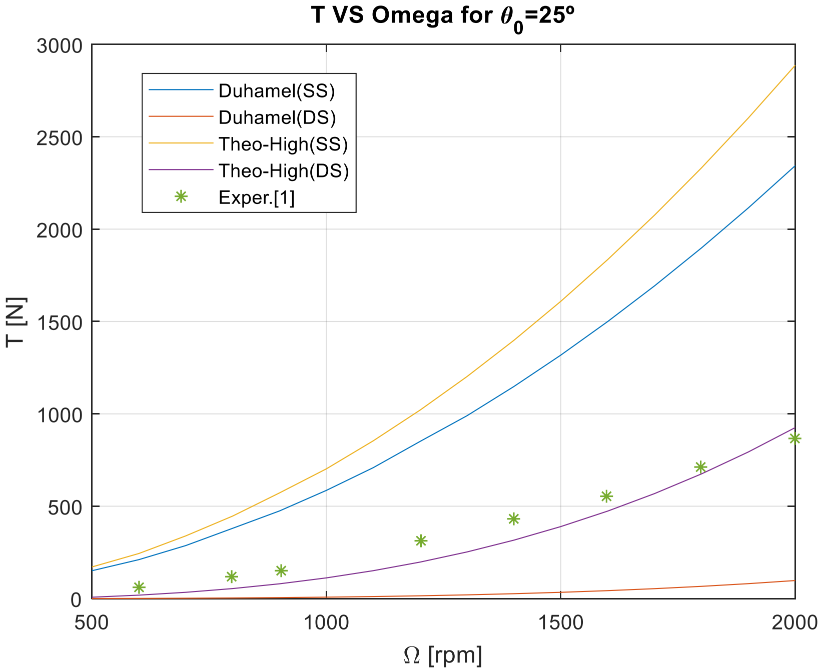

Figure 4.3: Resultant Thrust *(T)* VS Rotation Speed *(Ω)* for maximum pitch amplitude of θ_0= 25º

This last figure 4.3 corroborates the result observed before because the Double-Multiple Streamtube model (DS) using Theodorsen's theory with high unsteady effects is the best one in comparison to both experimental values from references [1] and [4]. Therefore, this conclusion allows to validate this model as the most suitable one to be used to obtain results about the performance of cyclocopters. However, in the following sections, the results from the other models are also going to be shown in order to be compared with this best model.

4.2.2 Four-bar Linkage Pitch Angle Mechanism

The equation which defines the pitch angle variation using this type of mechanism is 2.4 and the experimental values used now come from reference [2] and again, the web [6] was used to obtain them. As in previous subsection, DS model with Theodorsen's theory is found to be the best one compared with experiments, this model is going to be used in this subsection but supposing three cases depending of the value of the angular frequency ω (and therefore, of the reduced frequency k): Theodorsen with steady effects, Theodorsen with low unsteady effects and Theodorsen with high unsteady effects.

In addition, the table 4.4 shows the geometric parameters used to obtain the following graphs as well as the 4-bar parameters which are needed to define the structure of the mechanism and whose definitions are:

- L_1: Rotor radius (m).
- L_2: Magnitude of eccentricity (m).
- L_3: Length of control rod (m).
- L_4: Length d (m).
- ε: Phase angle of eccentricity (º).

Table 4.4: Geometry of cyclocopter used in figures 4.4 and 4.5

Characteristic	c (m)	R (m)	b (m)	N_b
	0.3048	0.6096	1.2192	6

4-bar parameters	L_1(m)	L_2(m)	L_3(m)	L_4(m)	ε
	0.6096	0.0315	0.6134	0.075	0°

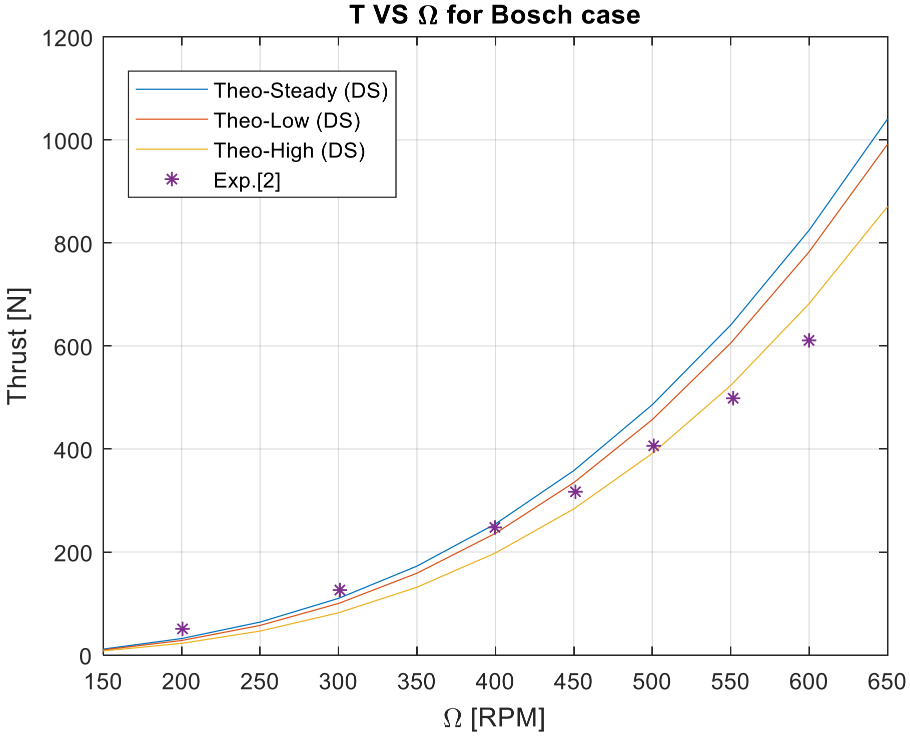

Figure 4.4: Resultant Thrust *(T)* VS Rotation Speed (*Ω*) (Bosch case)

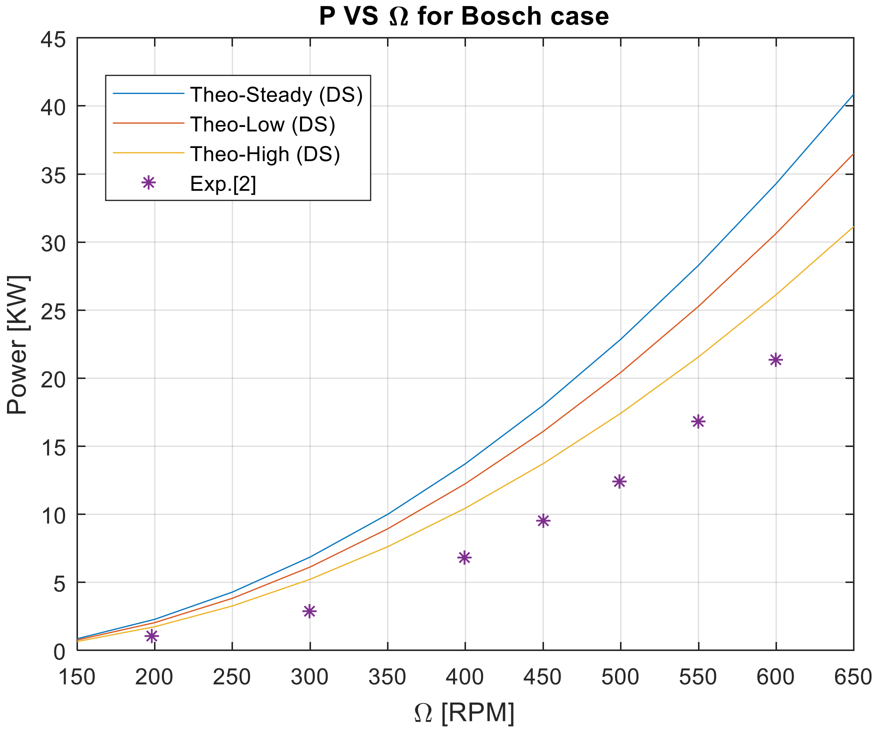

Figure 4.5: Power consumed *(P)* VS Rotation Speed (*Ω*) (Bosch case)

In relation to this Bosch case (figures 4.4 and 4.5), the three models give more or less the same values of thrust and power at low rotation speed. However, at higher speeds, the models start to give different solutions and so, Theodorsen's model with high unsteady effects is the best one for approximating the experimental values, which is in concordance with the result obtained with the sinusoidal variation of the pitch angle. Now, another case is shown in figures 4.6 and 4.7 with its respective experimental values and geometric parameters (table 4.5):

Table 4.5: Geometry of cyclocopter used in figures 4.6 and 4.7

Characteristic	c (m)	R (m)	b (m)	N_b
	0.52	0.6	1.2	6

4-bar parameters	L_1(m)	L_2(m)	L_3(m)	L_4(m)	ε
	0.6	0.038	0.6055	0.09	0°

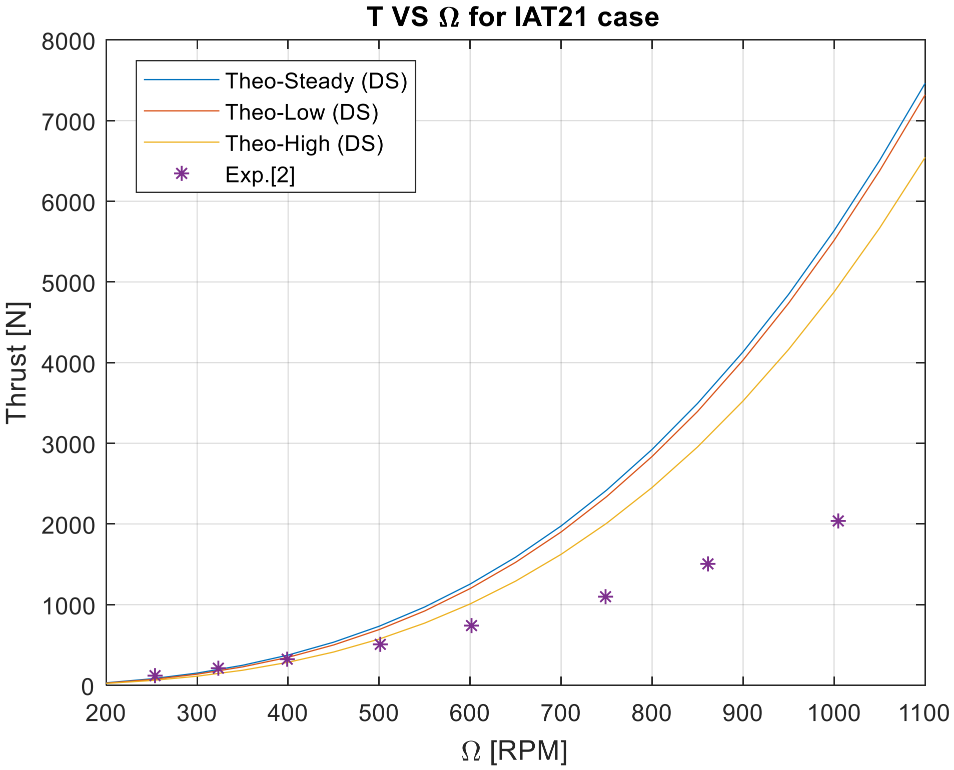

Figure 4.6: Resultant Thrust (T) VS Rotation speed (Ω) (IAT21 case)

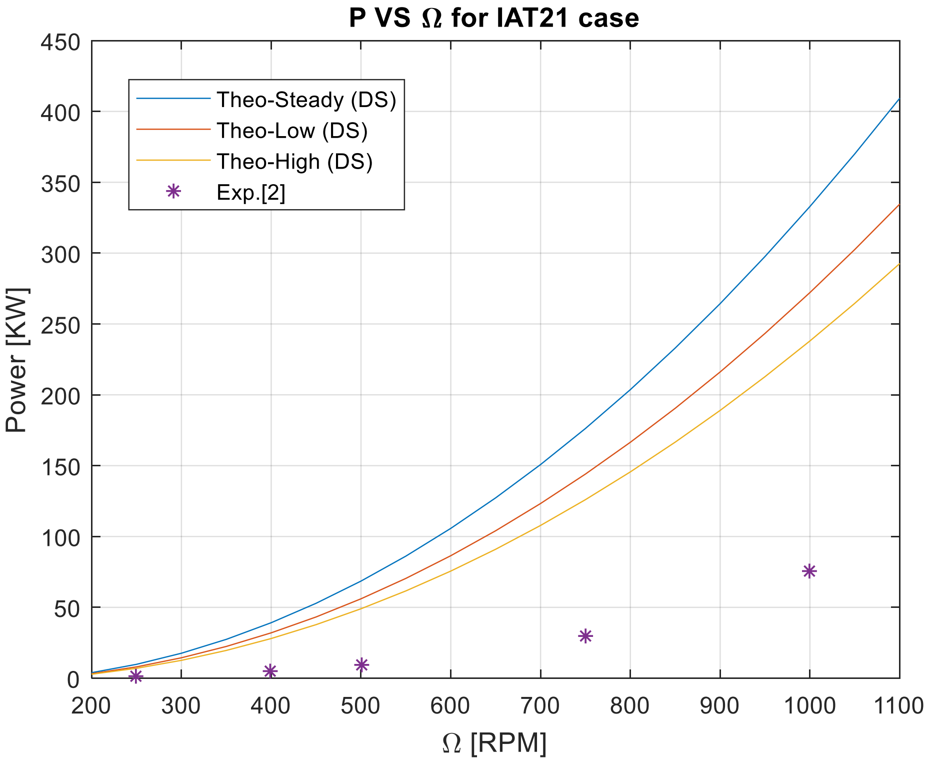

Figure 4.7: Power consumed (P) VS Rotation speed (Ω) (IAT21 case)

In figures 4.6 and 4.7 (IAT21 case), it is possible to see that the models results are worse in comparison to the Bosch case (figures 4.4 and 4.5) because the experimental values deviate from the predicted ones. However, these results are still acceptable due to the order of magnitude of them and also the trend obtained.

4.3 Analyses of Hover Flight

The results are going to be divided using again the same two different subsections like in the previous section: the first one considering the sinusoidal variation of the pitch angle with the azimuthal position and the second one considering the four-bar linkage mechanism.

4.3.1 Sinusoidal Pitch Angle Variation

Thrust VS Rotation speed

This first part of the subsection is focus on the Double-Multiple Streamtube code (DS), which is a better model than the Single Streamtube code (SS). Moreover, the geometric values used for obtaining results from this DS code were shown in table 4.1.

Therefore, the first conclusion that it is interesting to show is the selection of the Algorithm if the Duhamel model is chosen.

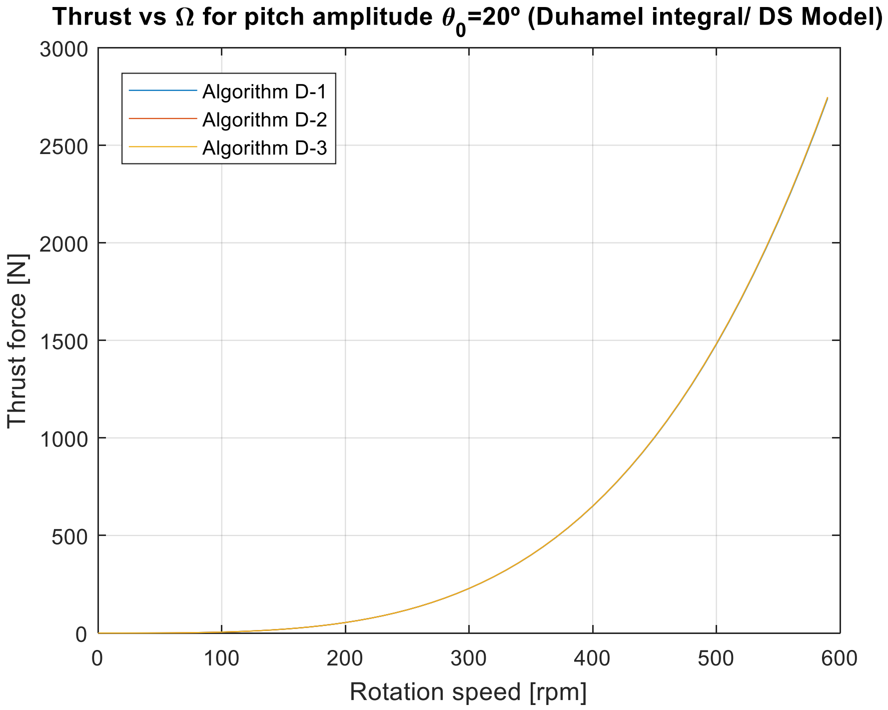

Figure 4.8: Comparison among the Algorithms in Duhamel integral/ DS inflow model

As it can be seen in figure 4.8, the selection of the Algorithm is not important because the results obtained with each of them are really similar. Therefore, Algorithm D-1 is going to be used because it is the simplest one.

If now Theodorsen's model is selected, the influence of the angular frequency (ω) is shown in figure 4.9 and so, the influence of the unsteady effects. In this figure 4.9, three cases are presented which are related with an specific value of ω:

- $\omega = 0$: Theodorsen with steady effects.

- $\omega = 5$: Theodorsen with low unsteady effects.
- $\omega = 10$: Theodorsen with high unsteady effects.

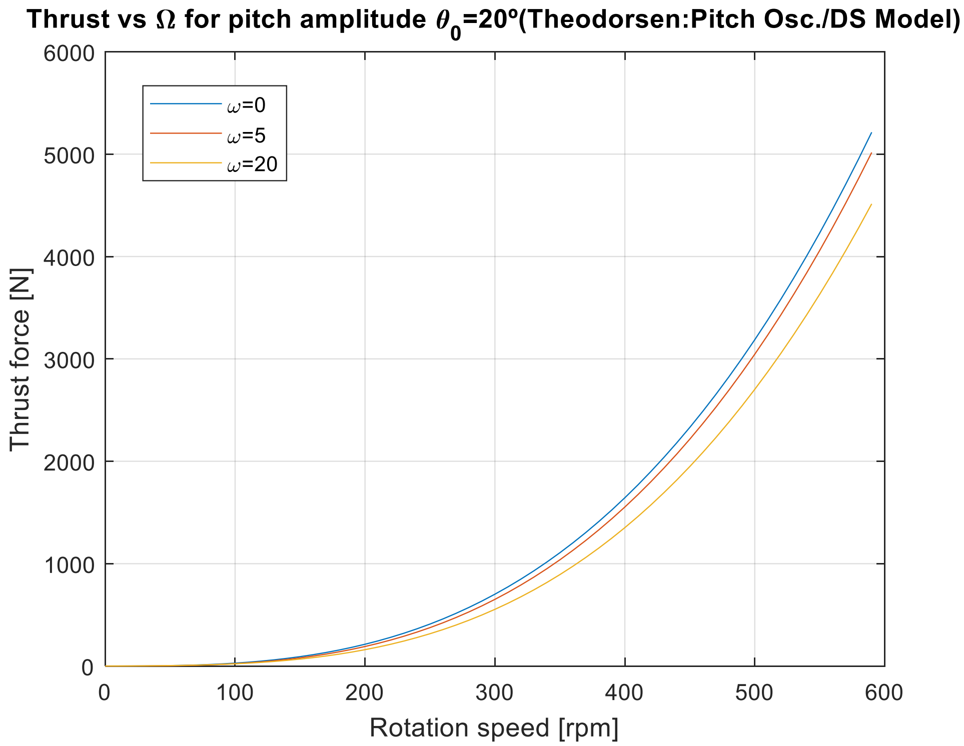

Figure 4.9: Effect of ω in the thrust produced (Theodorsen/ DS inflow model)

According to figure 4.9, if ω increases, which is in relation with the important of the unsteady effects (k increases), the thrust produced by the cyclocopter decreases for an specific rotation speed. This makes sense because if the flow is more unsteady, the thrust which the cyclocopter can produce is less.

The next figure 4.10 allows us to compare the different aerodynamic models, as well experimental values from reference [4], in relation to the thrust produced when the rotation speed is varied for two different maximum amplitudes of the pitch angle.

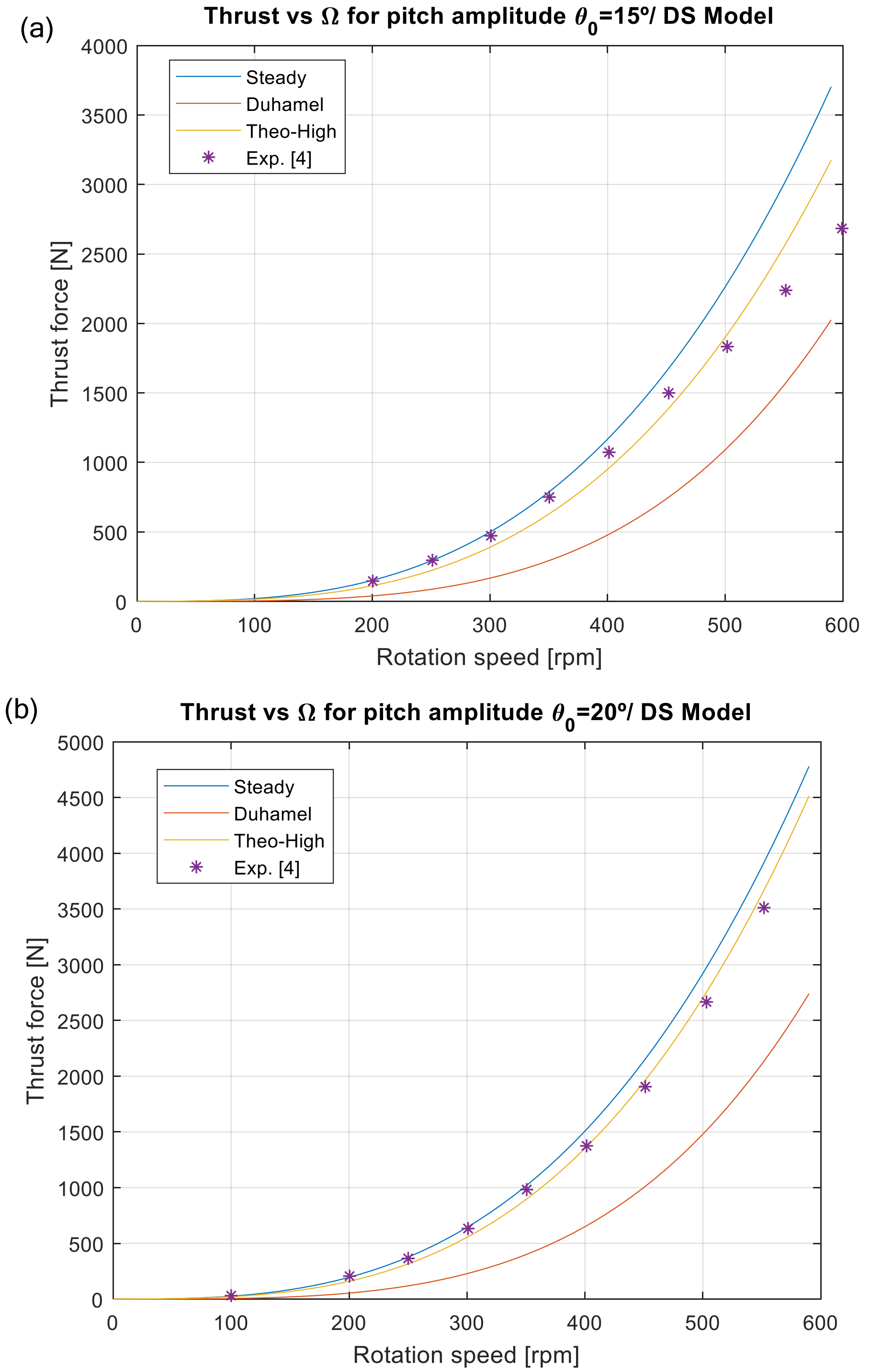

Figure 4.10: Comparison of steady and unsteady models with the rotation speed (Sinusoidal variation/DS inflow model) for pitch amplitudes of (a) θ_0=15º and (b) θ_0=20º

As it is possible to see in figure 4.10, the steady case adapts better to the experimental values when the rotation speeds are low and when it is increased, the model which approximates better the performance of the cyclocopter is Theodorsen (with a high value of reduced frequency). This last conclusion is in concordance with the result extracted during the validation of the models (section 4.2.1). In addition, comparing the two graphs of figure 4.10, it is possible to see that if the pitch angle amplitude is increased, the thrust produced is higher. However, this increase causes that the angle of attack were higher and so, the stalling of the profile may be achieved, fact which is not taken into account in these codes.

If the radius of the blades is changed, the results obtained appear in figure 4.11.

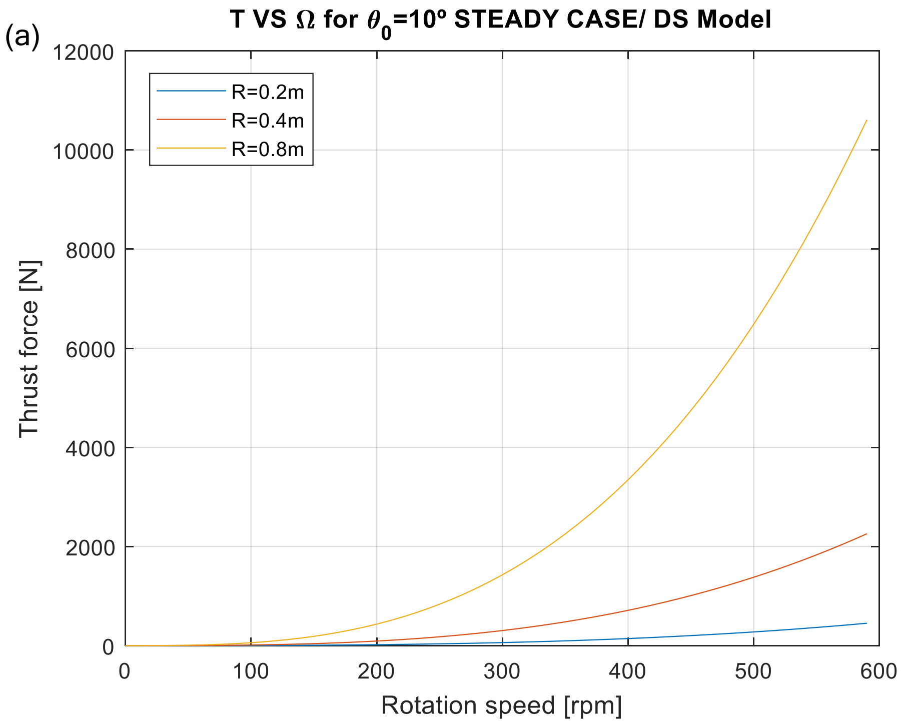

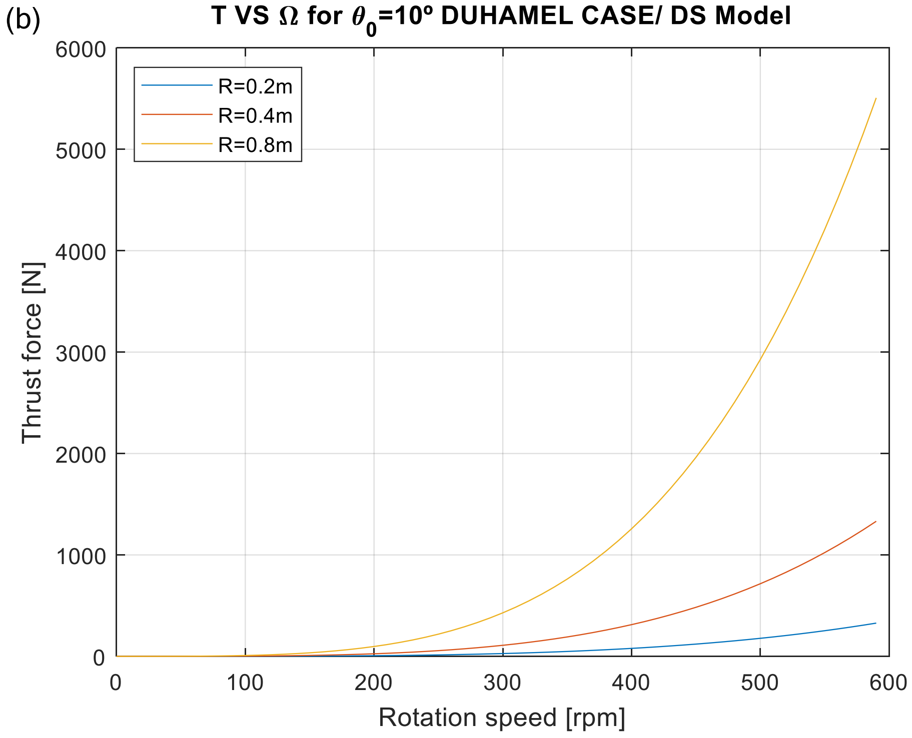

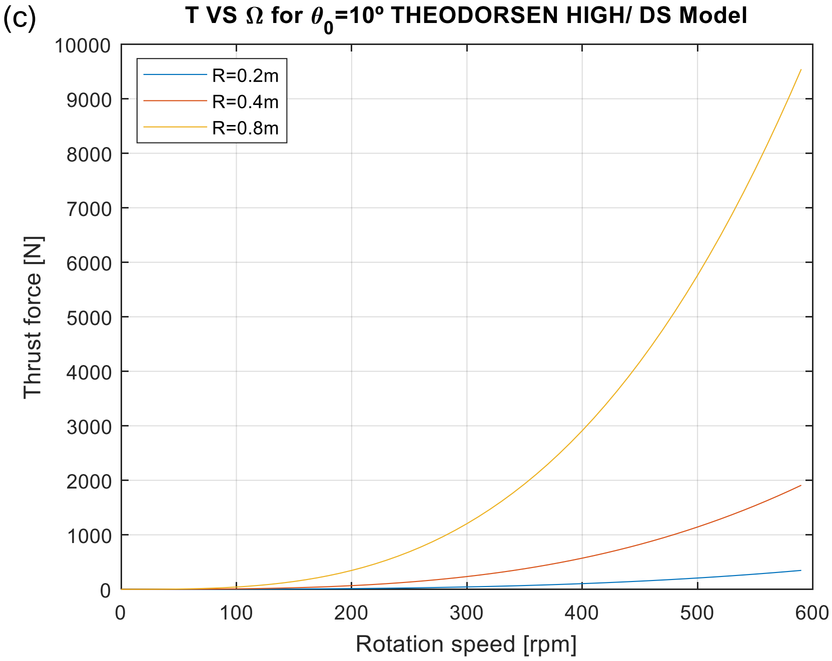

Figure 4.11: Effect of blade radius *(R)* on the thrust produced for (a) Steady case, (b) Duhamel integral and (c) Theodorsen with high unsteady effects (Sinusoidal variation/DS inflow model)

In the three graphs of figure 4.11, the conclusion obtained is the same: when the radius is increased, the thrust force produced increases as well and the slope of this increase is also higher. In the three cases, the trend of the curves of the same blade radius is pratically independent of the model used. Moreover, the strongest increase in thrust occurs in the steady case which may be possible due to the fact that it is the ideal case. However, the stalling of blades has not been taken into account and it could be possible that some of these thrusts can not be achieved in steady case as well as in both unsteady cases.

Another experiment which can be done is to change the number of blades but maintaining the total blade area. In order to do this, the blade chord and/or span is varied when the number of blades changes. The results are shown in figure 4.12.

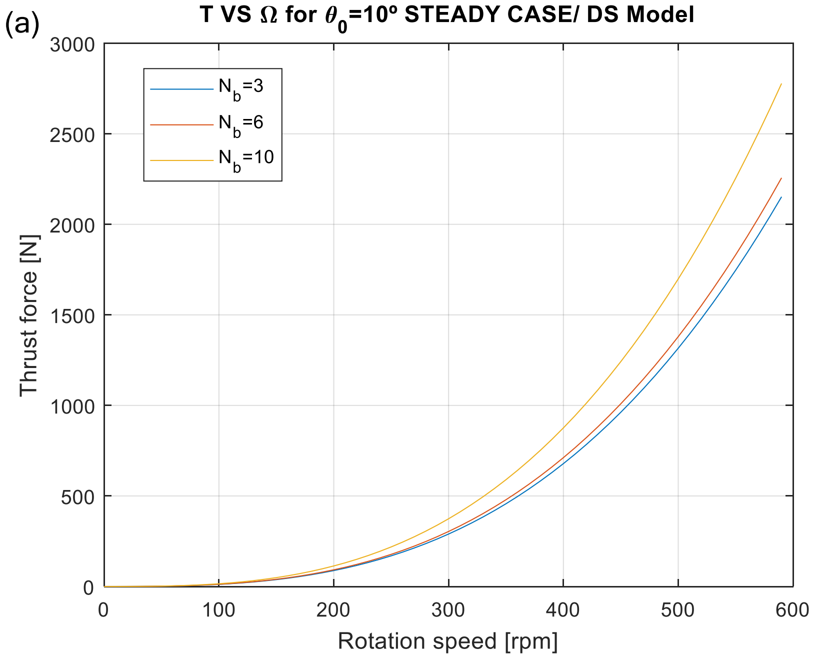

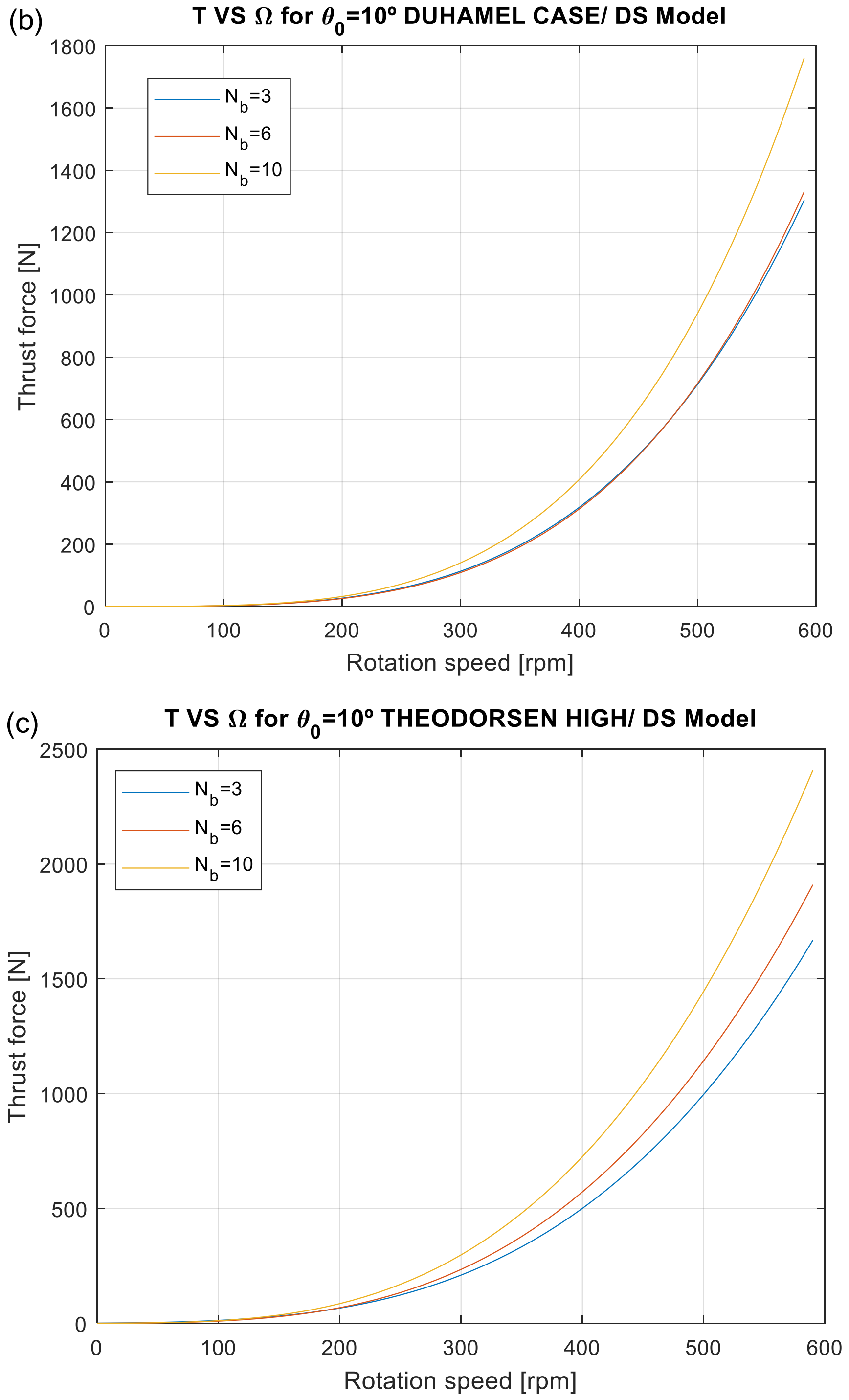

Figure 4.12: Effect of number of blades (N_b) on the thrust produced for (a) Steady case, (b) Duhamel integral and (c) Theodorsen with high unsteady effects (Sinusoidal variation/DS inflow model)

Thanks to figure 4.12, it is possible to see that increasing the number of blades, the thrust produced also increases and the trend which the curves follow is always more or less the same. In addition, the different between the thrusts produced is higher when the number of blades changes from 6 to 10 than the change from 3 to 6. This could show a possible increase in the growth of the thrust produced if the number of blades is further increased. However, the weight of the cyclocopter is higher and in some cases, it may be not a good choice to increase the number of blades since it can be heavier configuration, which may not be a desirable option.

Now, the code is changed to the Single Streamtube (SS) and the geometric values which are used appear in table 4.3. Using this model, the results obtained are presented in the following figures and compared with experimental values from reference [1]:

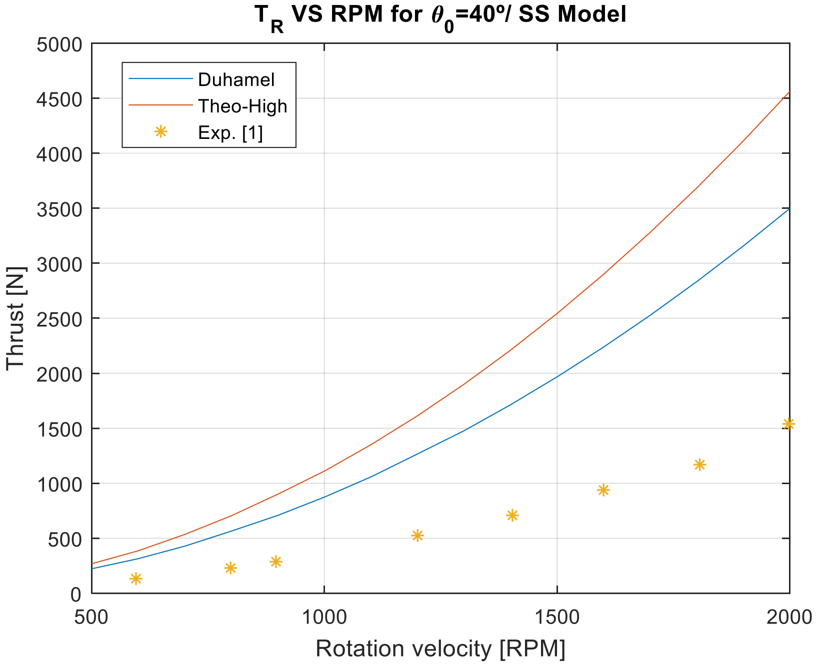

Figure 4.13: Comparison of unsteady models with the rotation speed (Sinusoidal variation/SS inflow model) compared with experiments from [1]

In contrast to the DS code, with this SS model, Duhamel's theory approximates better the experimental values. If this theory is used and the pitch angle amplitude is modified, the graph obtained is the following one:

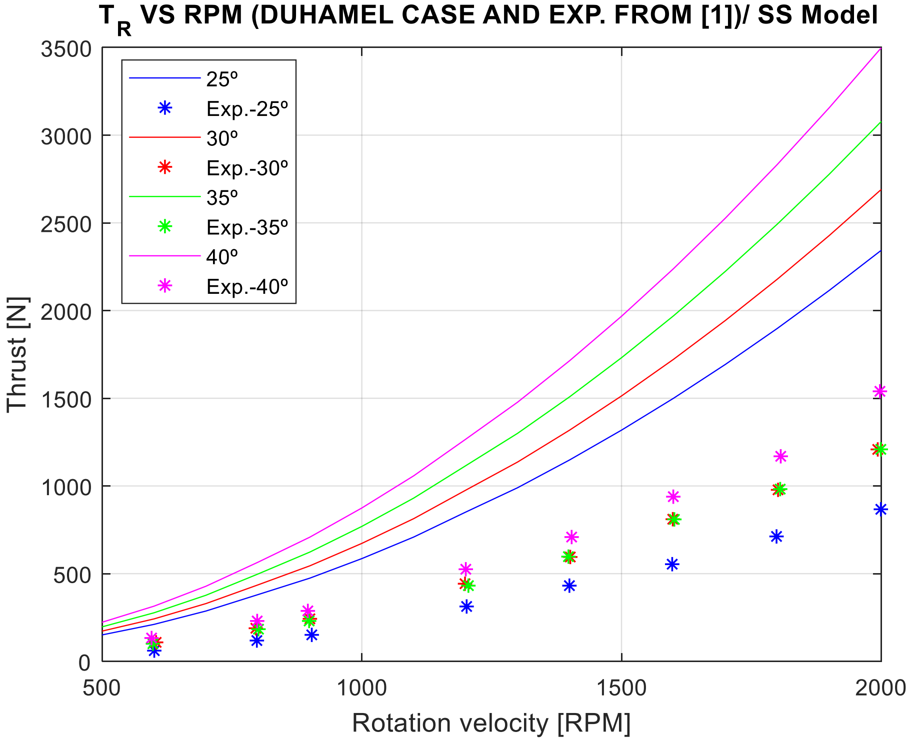

Figure 4.14: Effect of pitch angle amplitude (θ_0) on the thrust produced (Sinusoidal variation/SS inflow model) compared with experiments from [1]

In relation to figure 4.14, the conclusion is the same as previously: an increase in the pitch angle amplitude causes an increase in the thrust produced. However, the difference between results obtained with the codes and experiments are now further than in the DS code, which is a reasonable conclusion due to the fact that this SS code is not so accurate.

Changing now the blade radius, the new results are:

(a)

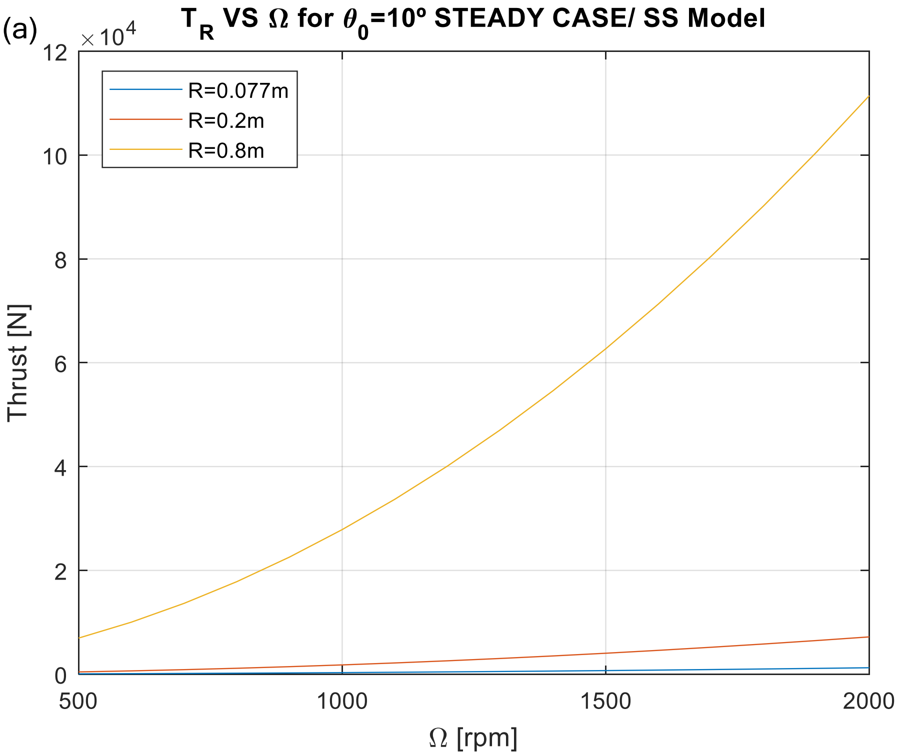

(b)

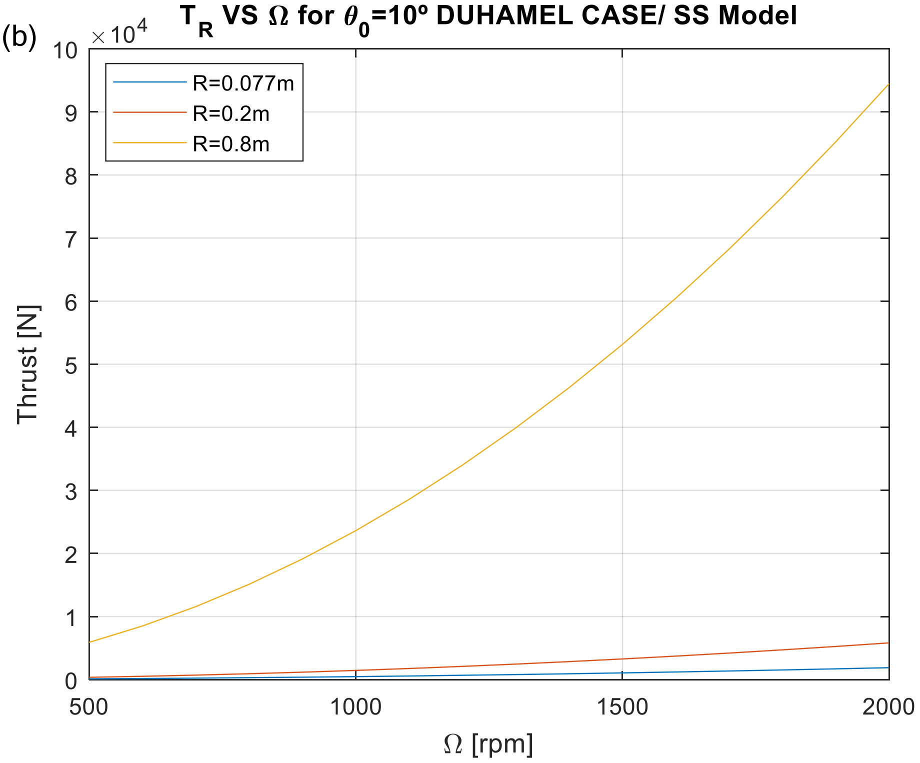

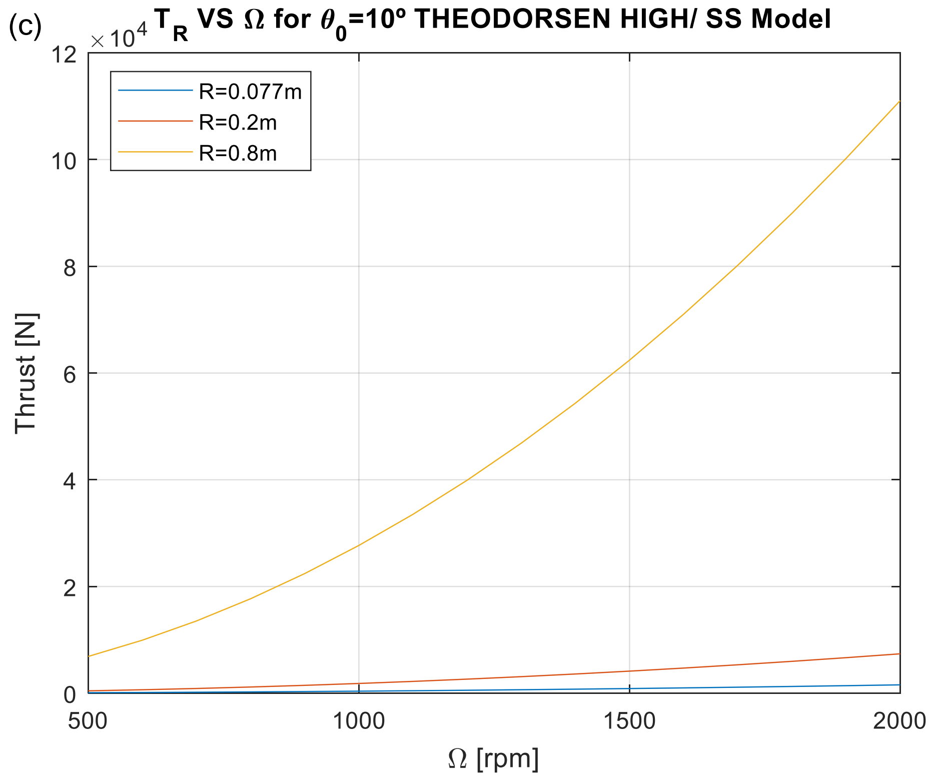
(c) T_R VS Ω for θ_0=10º THEODORSEN HIGH/ SS Model

Figure 4.15: Effect of blade radius *(R)* on the thrust produced for (a) Steady case, (b) Duhamel integral and (c) Theodorsen with high unsteady effects (Sinusoidal variation/SS inflow model)

Again when the radius is increased, the resultant thrust increases as well. Moreover, the change on the thrust produced when the radius changes from 0.2m to 0.8m in this figure 4.15 is quite higher in comparison to figure 4.11, but this conclusion may be due to the different geometric values used to obtain each result.

Finally, if the number of blades is varied:

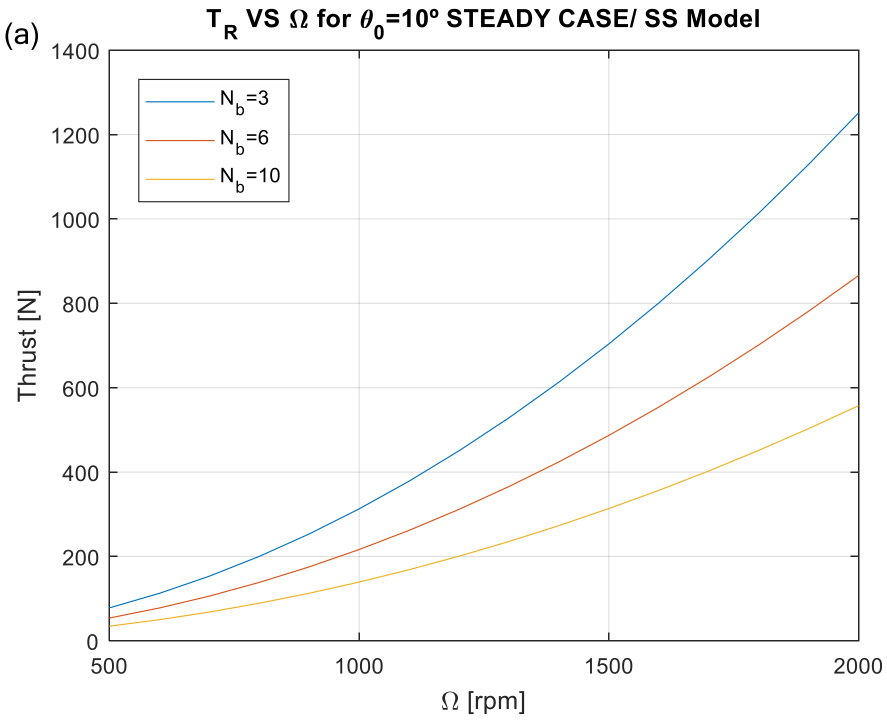
(a) T_R VS Ω for θ_0=10º STEADY CASE/ SS Model

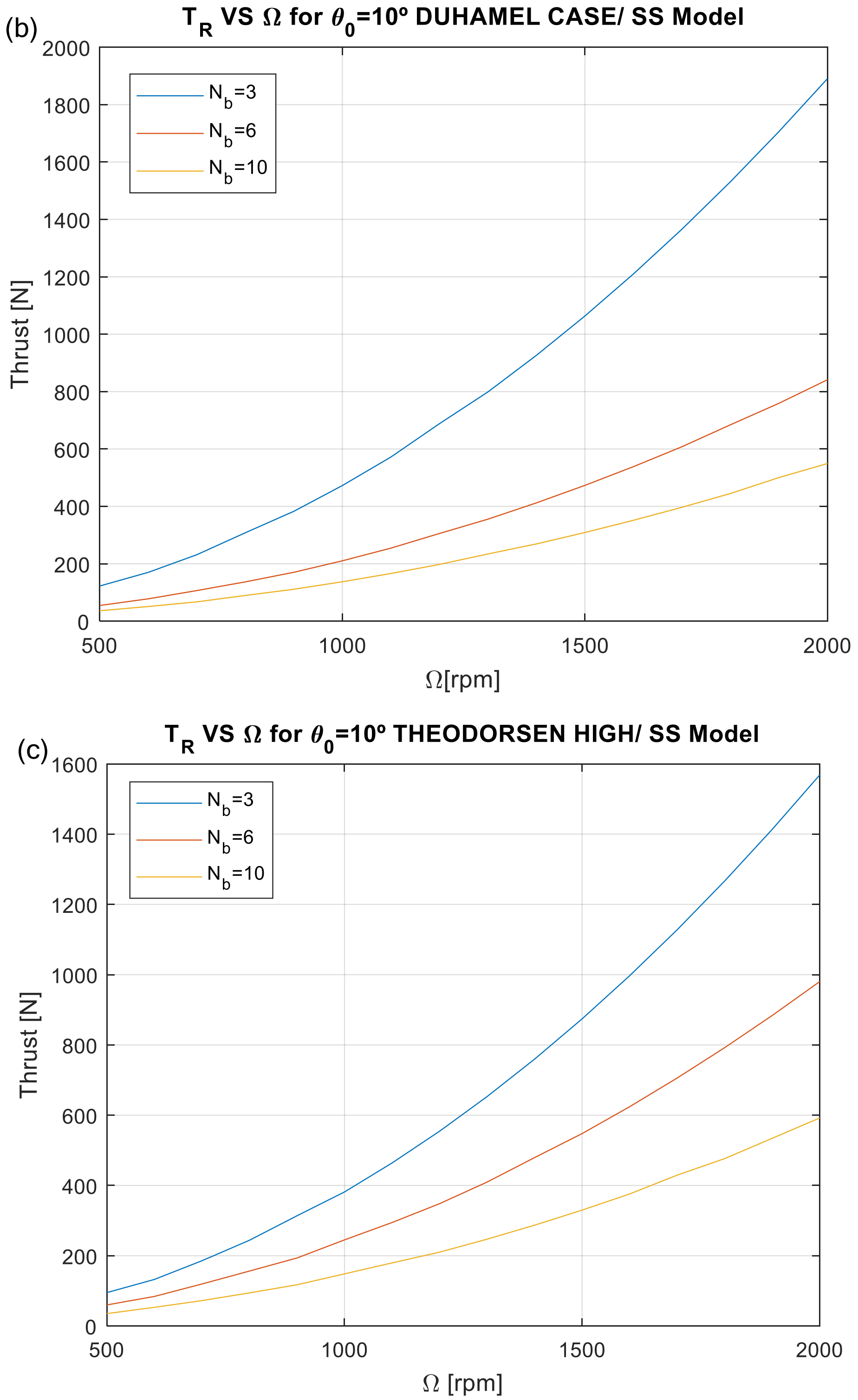

Figure 4.16: Effect of number of blades (N_b) on the thrust produced for (a) Steady case, (b) Duhamel integral and (c) Theodorsen with high unsteady effects (Sinusoidal variation/SS inflow model)

The conclusion remains the same as before: increasing the number of blades, the thrust produced also increases. In addition, the same effect occurs in this figure 4.16 if it is compared to figure 4.12 that the changes in thrust when the number of blades is varied is higher in the SS model than in DS model.

Thrust VS Pitch Angle Amplitude

Like it was done in Thrust VS Ω, the first part uses the DS code and with it, the results obtained are shown in the following figures:

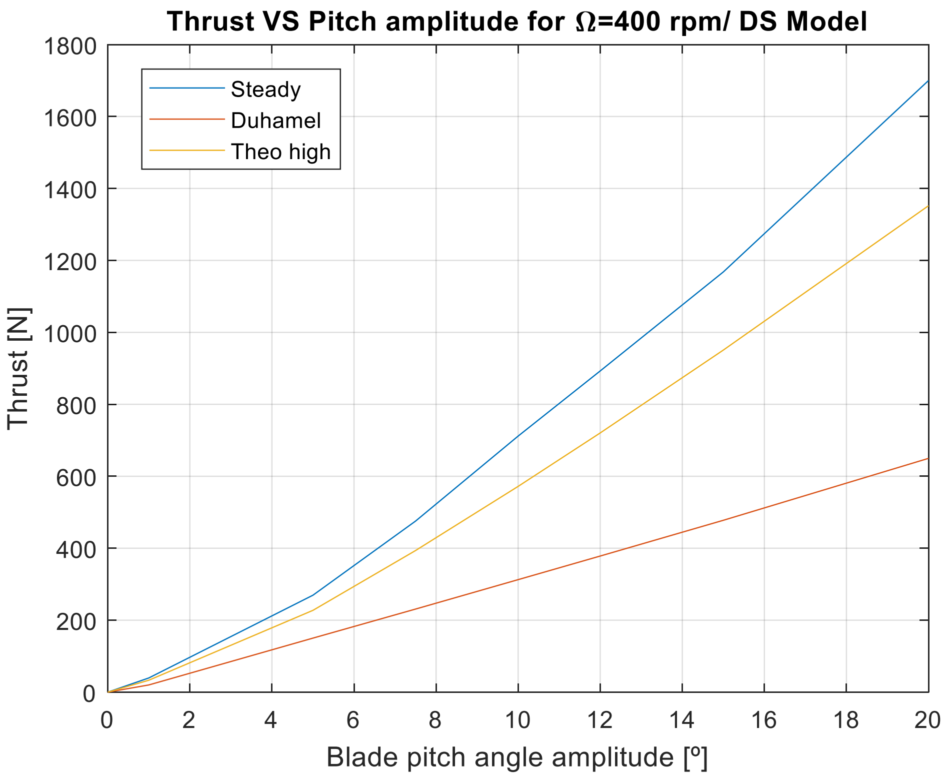

Figure 4.17: Comparison of steady and unsteady models with the pitch amplitude (Sinusoidal variation/DS inflow model)

From figure 4.17, it is possible to see that the steady case gives the highest thrust and Duhamel's model, the lowest one which is in concordance with all previous figures. Moreover, all models follow more or less a linear dependant between this two variables.

If now the rotation speed is varied, the curves obtained are shown in figure 4.18.

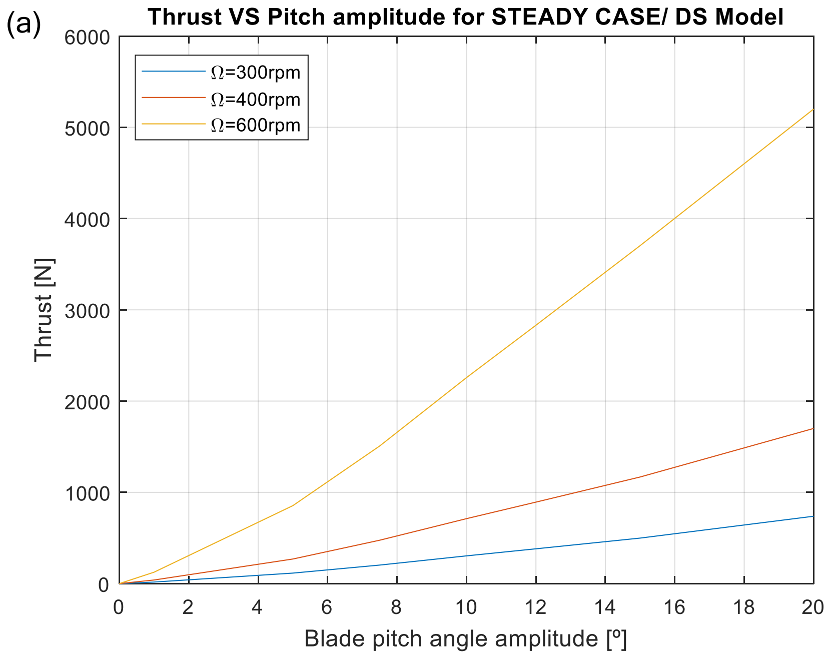

(b)

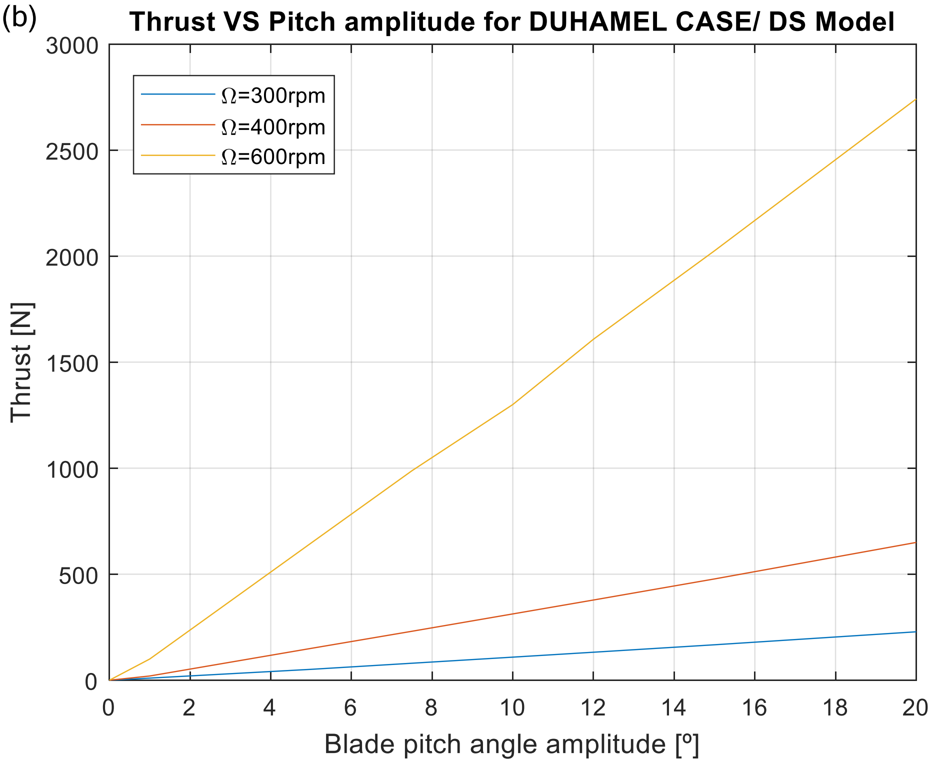

(c)

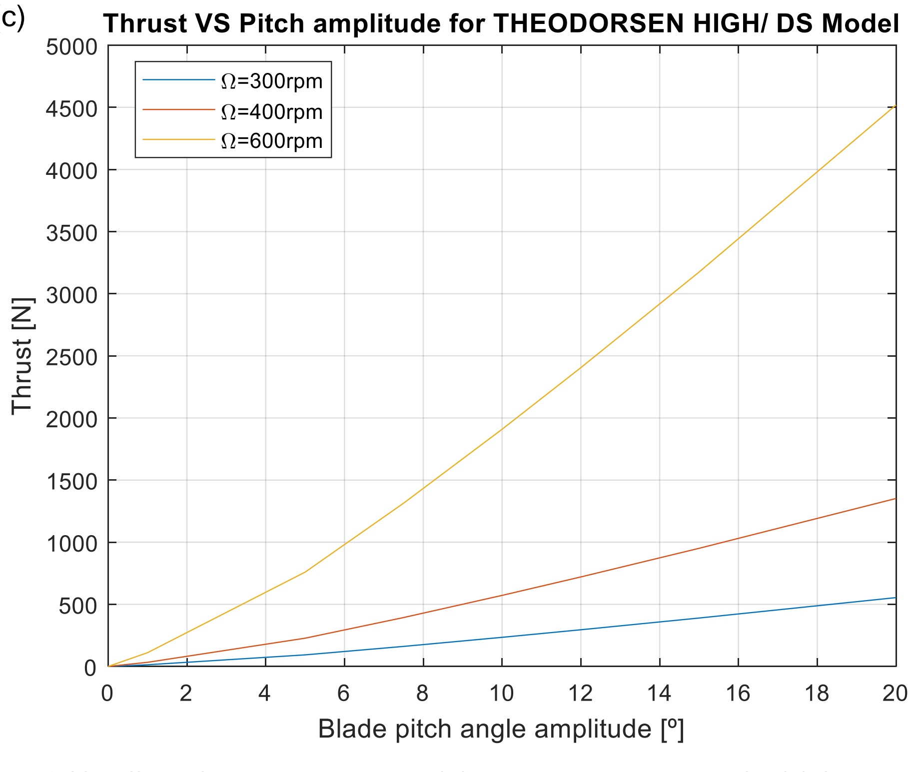

Figure 4.18: Effect of the rotation speed *(Ω)* on the thrust produced for (a) Steady case, (b) Duhamel integral and (c) Theodorsen with high unsteady effects (Sinusoidal variation/DS inflow model)

In relation to the graphs from figure 4.18, the thrust produced is higher when the rotation speed increases in any of the models used which is reasonable. Moreover, it seems to be a linear dependence between the two variables like it was observed in figure 4.17. The problem that may appear is a structural limitation of the cyclorotor which not allow to increase more the rotation speed above a certain limit.

Changing to the SS code, the results are the followings:

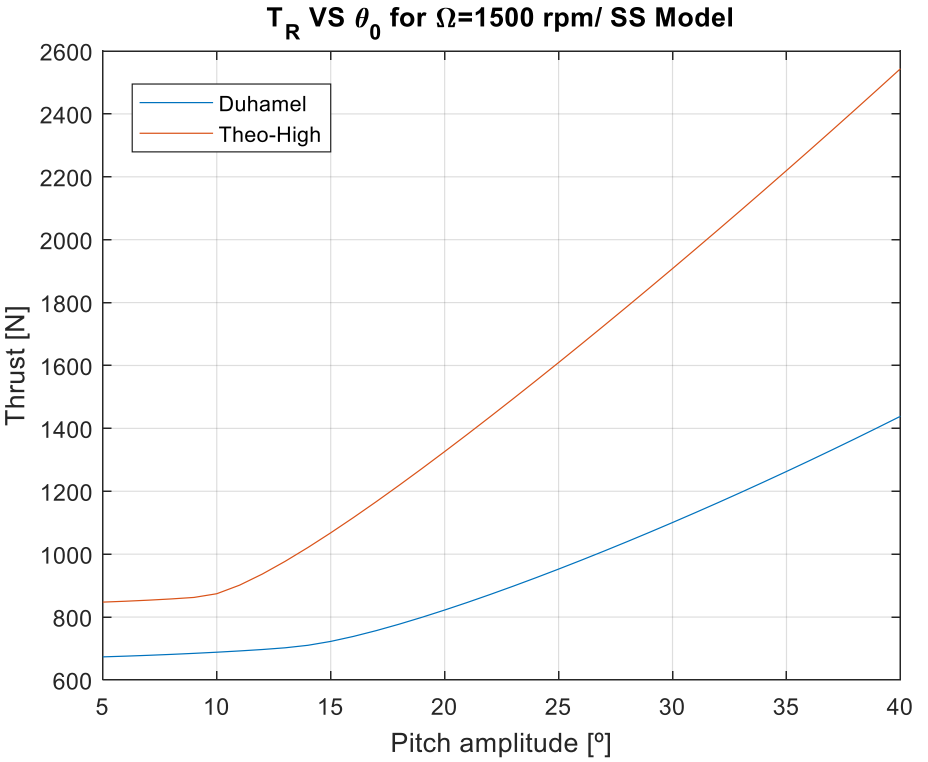

Figure 4.19: Comparison of unsteady models with the pitch amplitude (Sinusoidal variation/SS inflow model)

Thanks to figure 4.19, it is possible to show that the linear dependence between thrust and pitch angle amplitude remains in this SS code and now, a change in the slope of the line can be seen around 10º of the pitch angle amplitude.

If now, the rotation speed is varied:

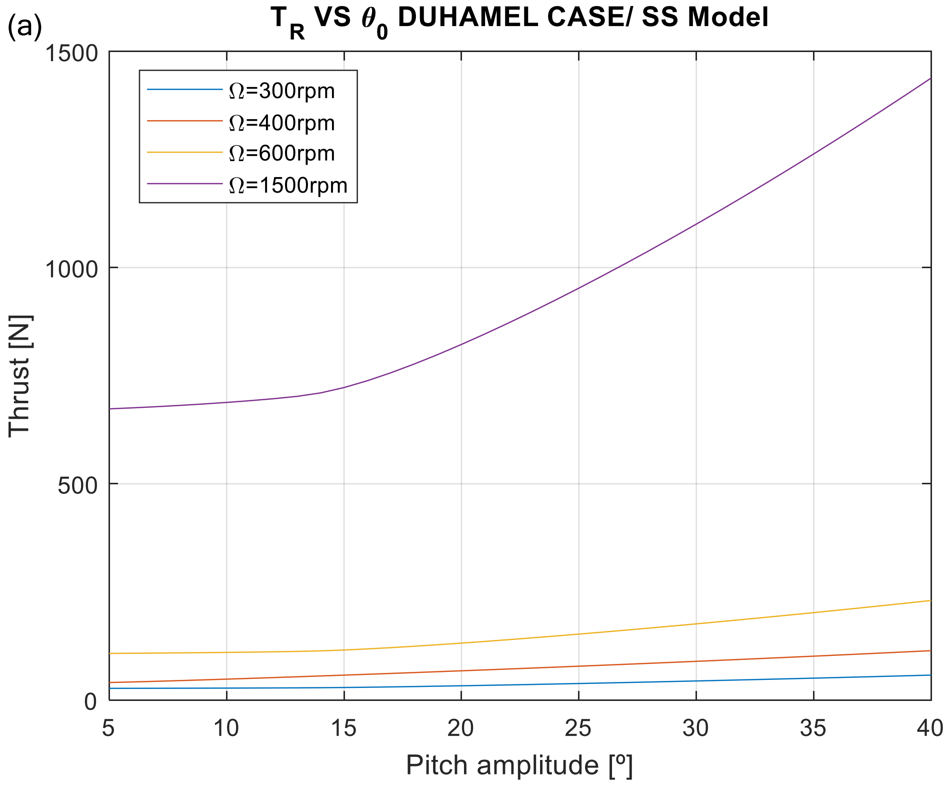

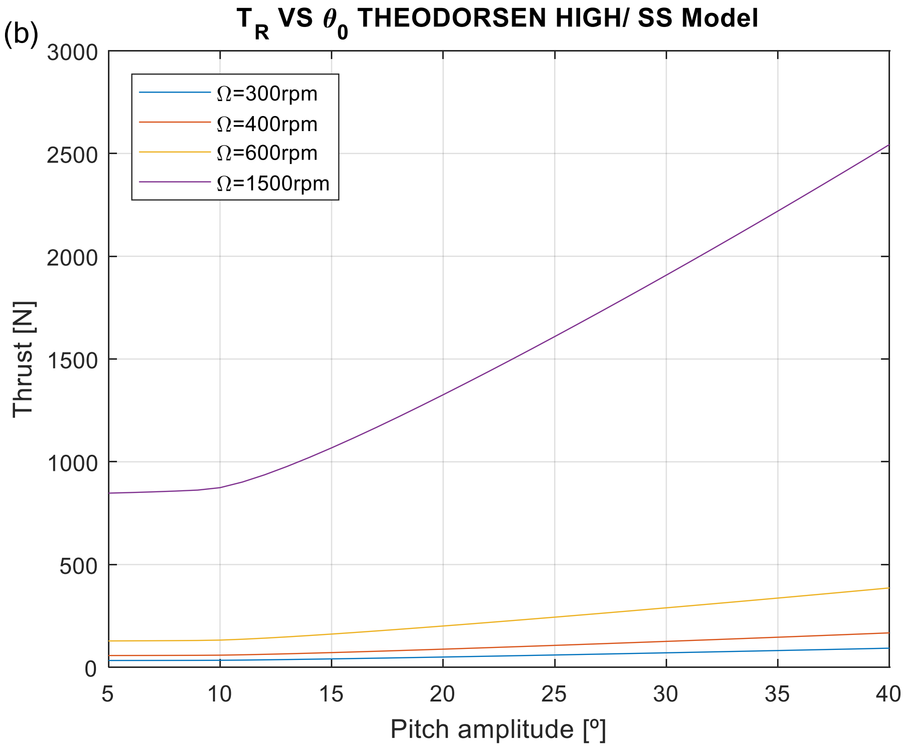

Figure 4.20: Effect of the rotation speed (*Ω*) on the thrust produced for (a) Duhamel integral and (b) Theodorsen with high unsteady effects (Sinusoidal variation/SS inflow model)

From figures 4.19 and 4.20, the conclusions which were writen previously are corroborated with these new results from SS code.

4.3.2 Four-bar Linkage Pitch Angle Mechanism

Thrust VS Rotation speed

The procedure is going to be the same like it was done with the sinusoidal pitch angle variation, starting with DS code and next, with the SS code. The geometric values used in this first part appear in table 4.2 and the goal is to vary the four-bar linkage mechanism parameters (L_1, L_2, L_3, L_4 and ε) in order to see their influence in the thrust produced. In particular, the two parameters which are going to be used are the magnitude of eccentricity (L_2) and the phase angle of eccentricity (ε). So, four cases are going to be analysed and like this, the results obtained are the following ones:

- CASE 1: L_1=0.4m L_2=0.01m L_3=0.5m L_4=0.4m ε=0º
- CASE 2: L_1=0.4m L_2=0.01m L_3=0.5m L_4=0.4m ε=10º
- CASE 3: L_1=0.4m L_2=0.03m L_3=0.5m L_4=0.4m ε=0º
- CASE 4: L_1=0.4m L_2=0.03m L_3=0.5m L_4=0.4m ε=10º

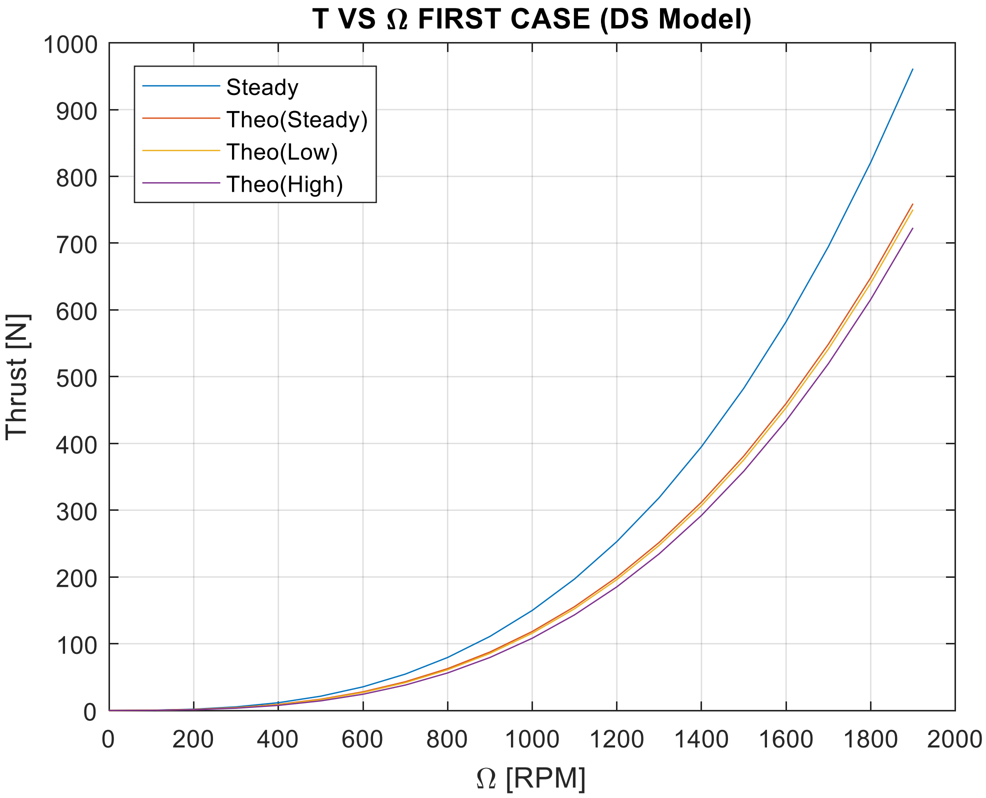
T VS Ω FIRST CASE (DS Model)
Steady
Theo(Steady)
Theo(Low)
Theo(High)
Thrust [N]
0
100
200
300
400
500
600
700
800
900
1000
Ω [RPM]
0
200
400
600
800
1000
1200
1400
1600
1800
2000

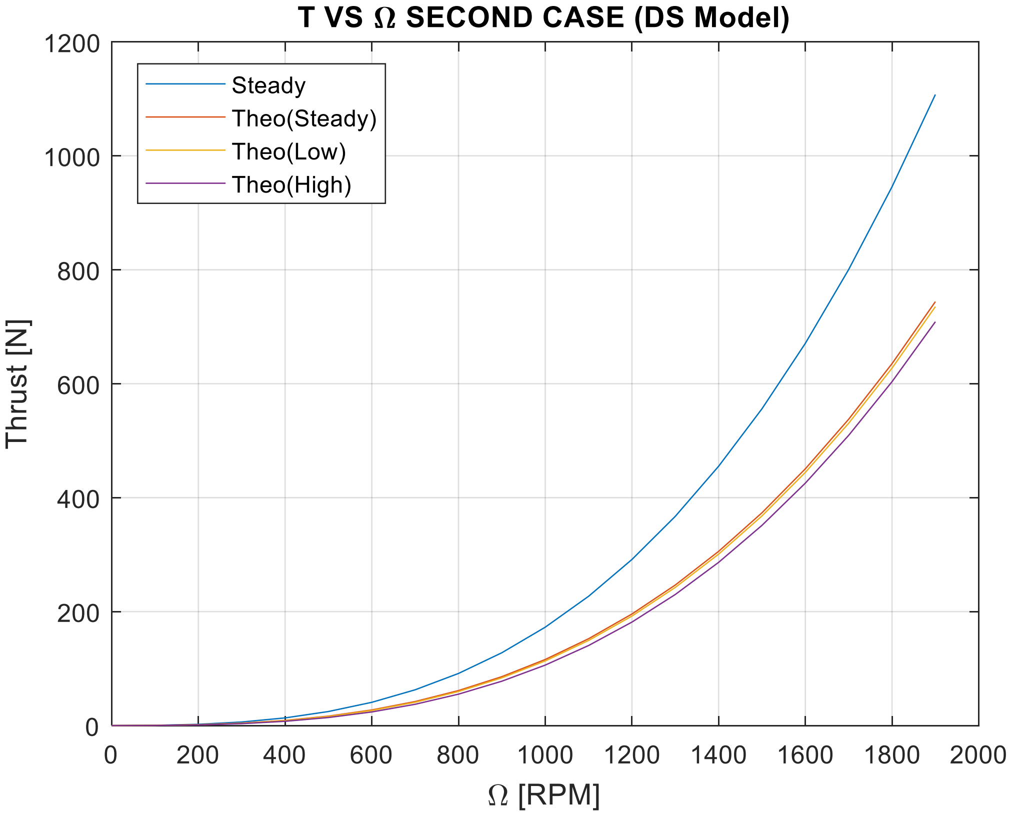
T VS Ω SECOND CASE (DS Model)
Steady
Theo(Steady)
Theo(Low)
Theo(High)
Thrust [N]
0
200
400
600
800
1000
1200
Ω [RPM]
0
200
400
600
800
1000
1200
1400
1600
1800
2000

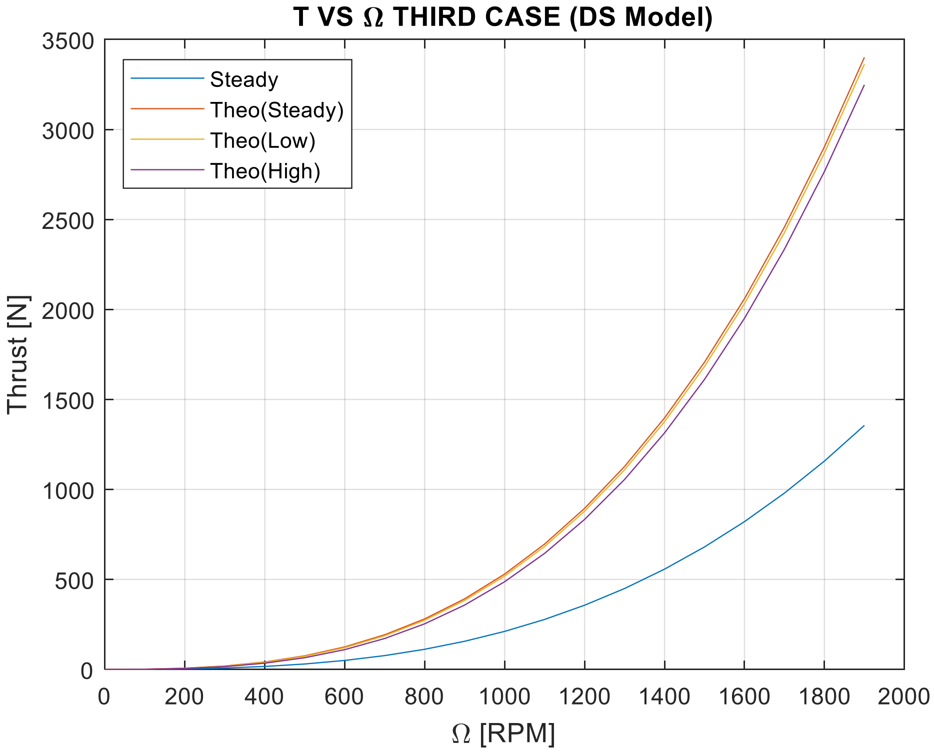

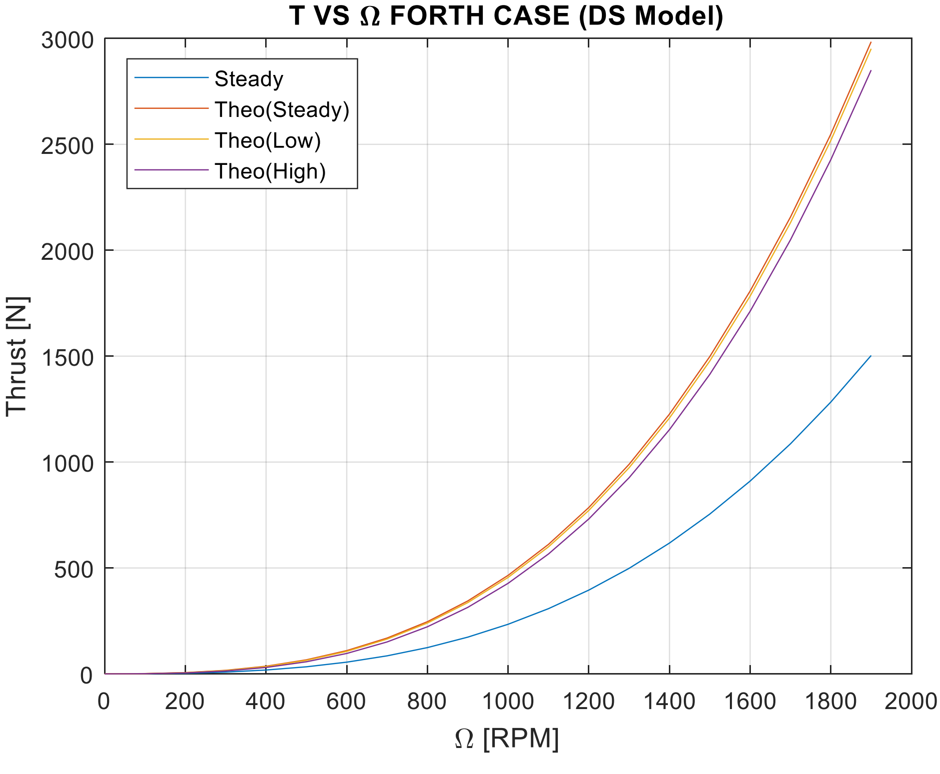

Figure 4.21: Comparison of steady and unsteady models with the rotation speed for four cases (4-bar mechanism/DS inflow model)

Comparing the four graphs of figure 4.21, the first conclusion which can be extracted is that changing the length L_2 from 0.01m to 0.03m, the thrust produced using the steady model passes to be the highest one to the lowest. However, in order to see in a better way the effects of the four-bar linkage parameters, figures 4.22 and 4.23 are shown:

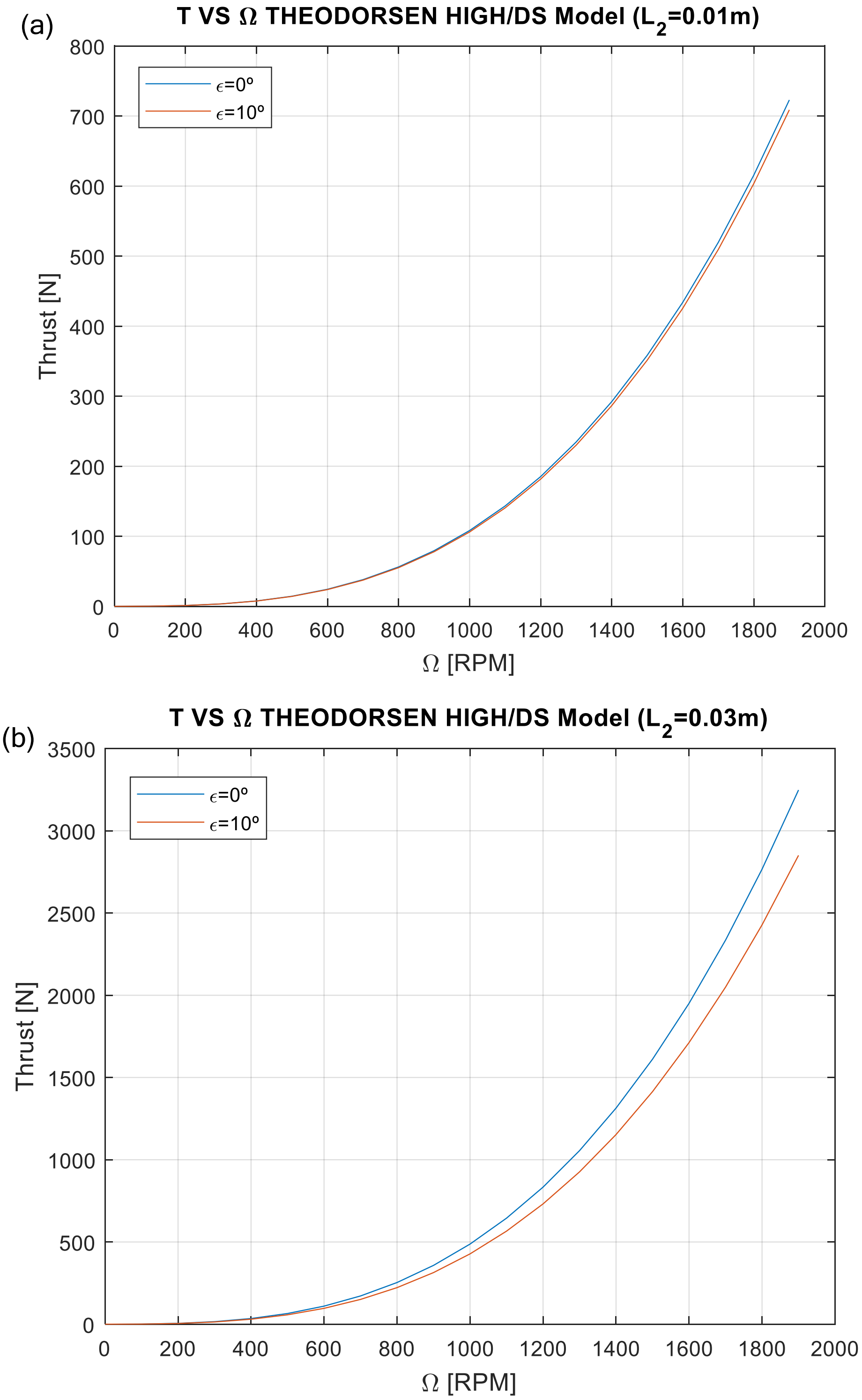

Figure 4.22: Effect of the phase angle of eccentricity (ε) on the thrust produced for (a) L_2=0.01m and (b) L_2=0.03m (4-bar mechanism/DS inflow model)

Thanks to figure 4.22, it is possible to see that the effects of changing ε are higher when L_2 increases as well as increasing ε causes a disminution on the thrust produced. These two conclusions can be also demonstrated using the next figure 4.23.

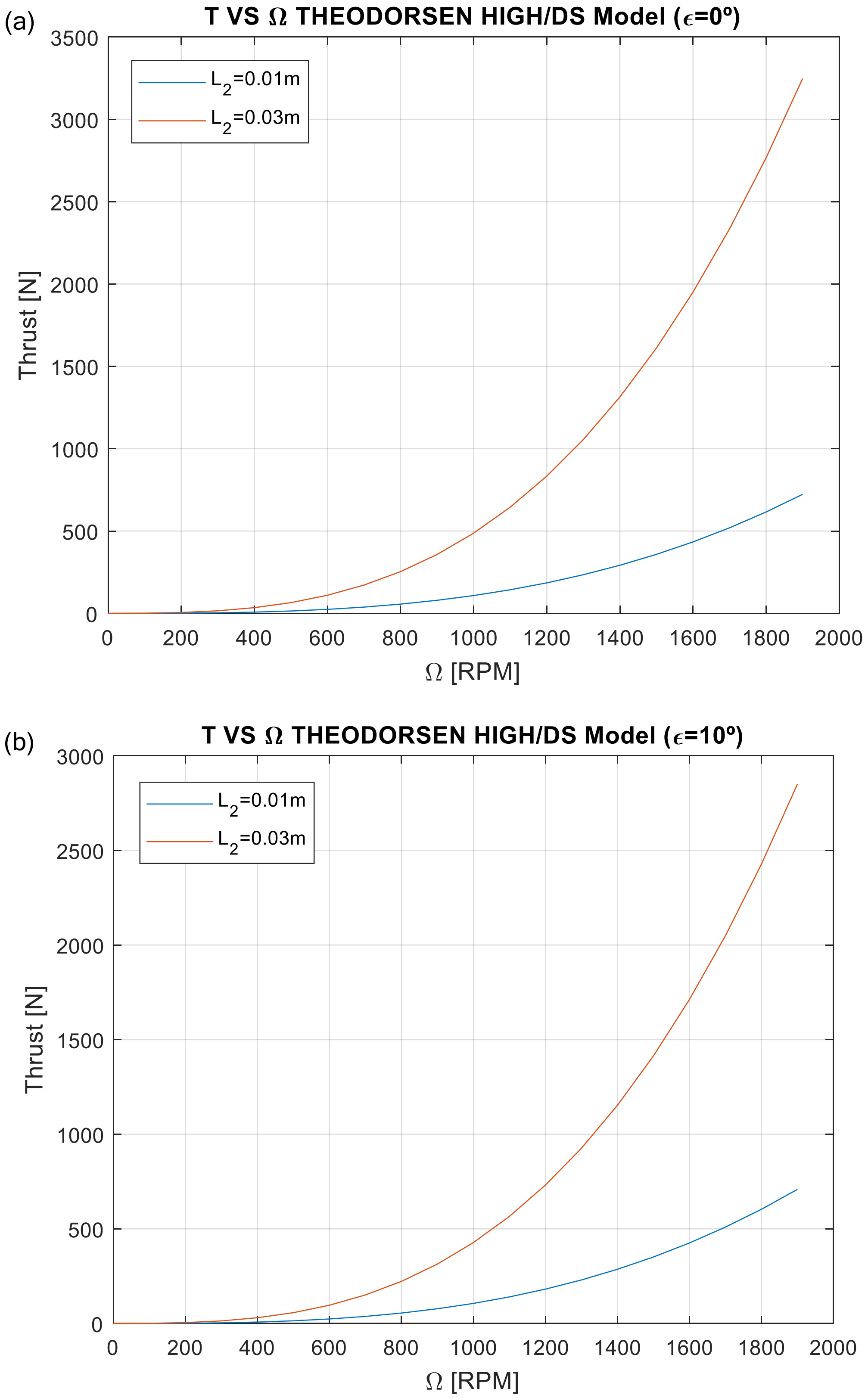

Figure 4.23: Effect of the magnitude of eccentricity (L_2) on the thrust produced for (a) ε=0º and (b) ε=10º (4-bar mechanism/DS inflow model)

In addition, figure 4.23 demonstrates that increasing L_2, the thrust produced also increases. Changing to the SS code, the graphs obtained are:

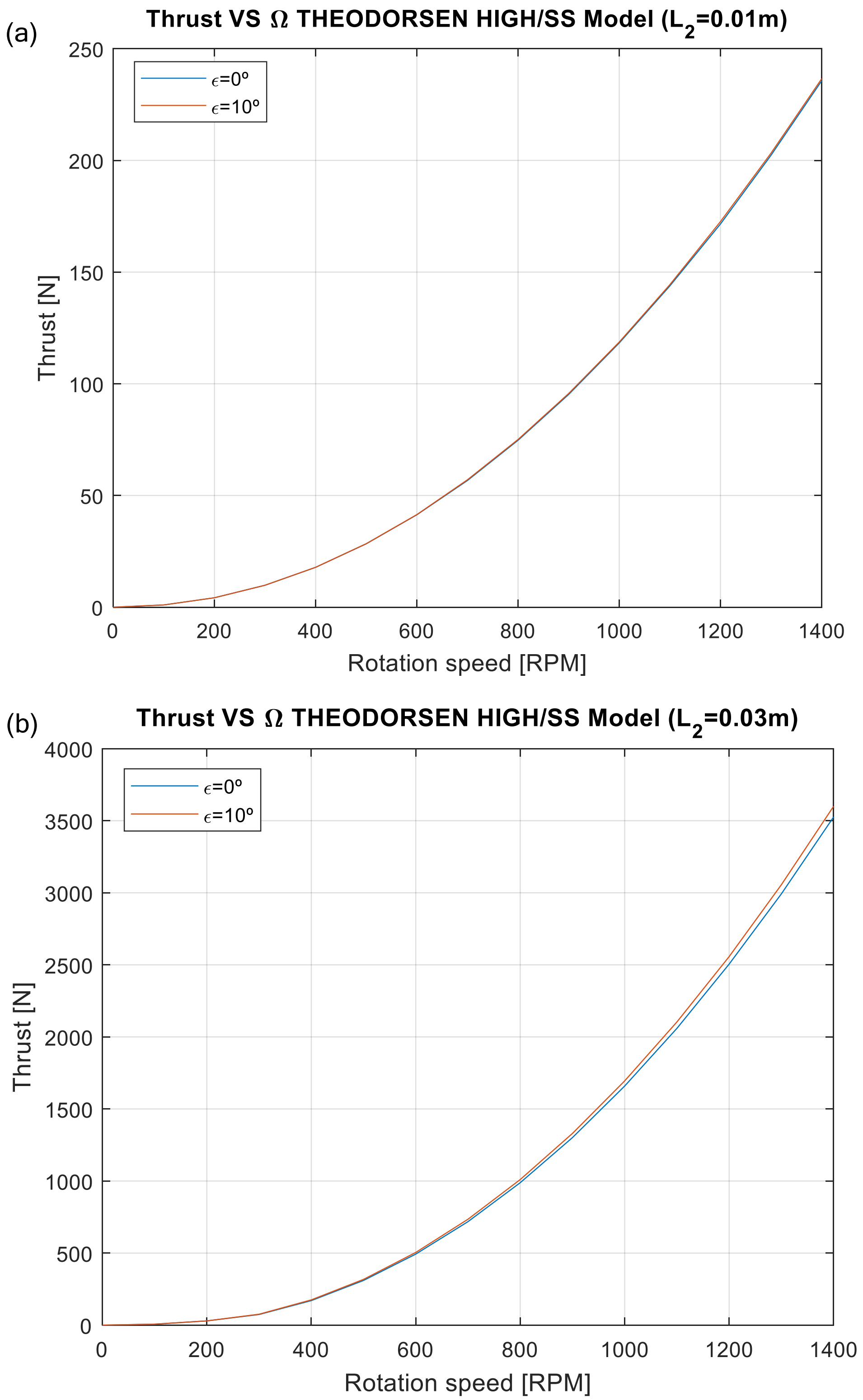

Figure 4.24: Effect of the phase angle of eccentricity (ε) on the thrust produced for (a) L_2=0.01m and (b) L_2=0.03m (4-bar mechanism/SS inflow model)

In this SS code, the effect of varying ε is lower than in the DS code like it is possible to see in the two graphs of figure 4.24.

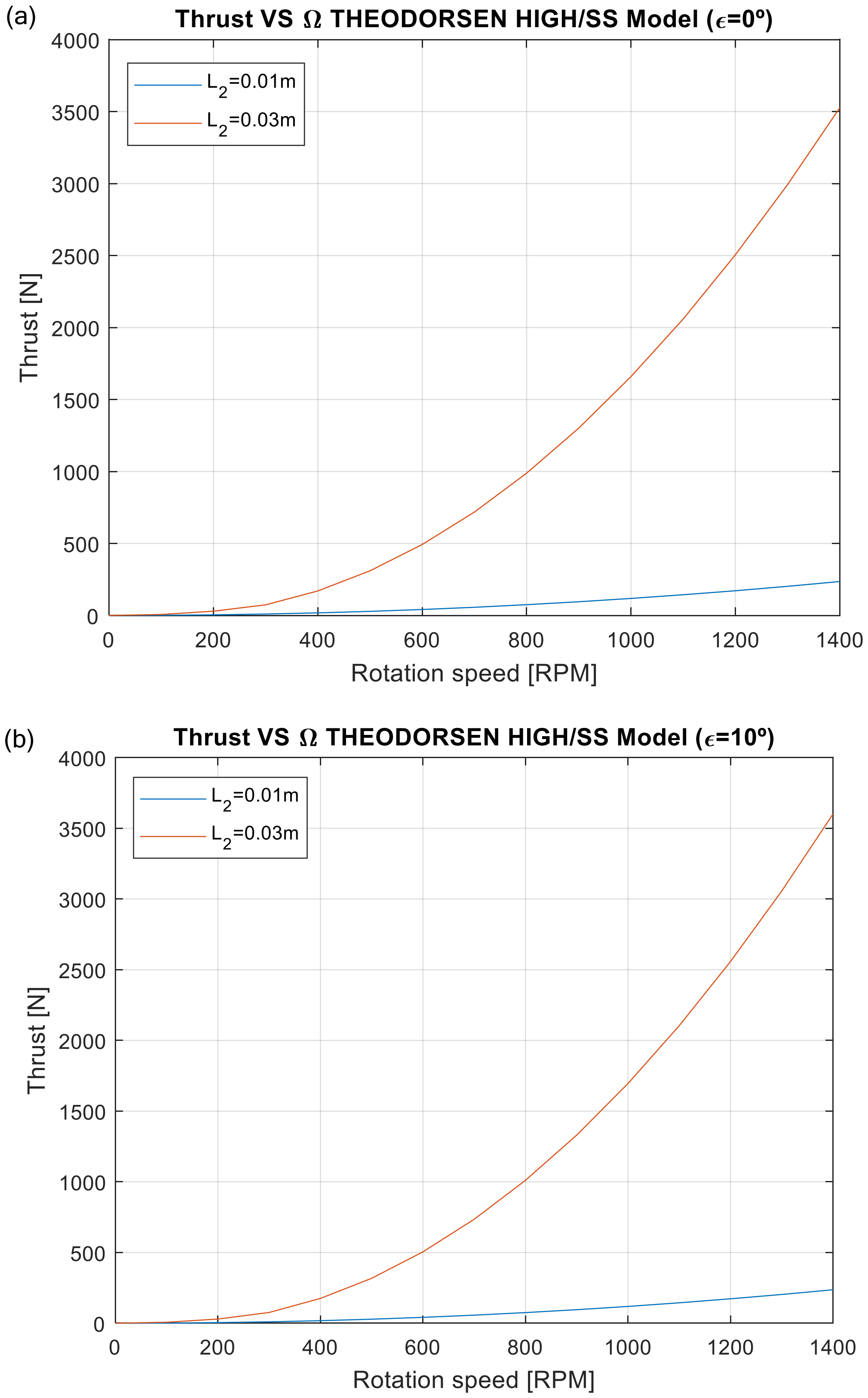

Figure 4.25: Effect of the magnitude of eccentricity (L_2) on the thrust produced for (a) ε=0º and (b) ε=10º (4-bar mechanism/SS inflow model)

This figure 4.25 also proves that increasing L_2 increases the thrust produced but now, in contrast to the conclusion exposed before from figure 4.24, the effect of varying L_2 is higher than in the DS code.

Thrust VS Pitch Angle Amplitude

These graphs are represented in the last subsection (Thrust VS Rotation speed) when the four-bar linkage mechanism parameters are varied because this causes that the pitch angle amplitude changes. The problem here is that there is not a direct relation between the pitch amplitude and the variation of it like it occurred when a sinusoidal variation was considered. So, obtaining these graphs is not so easy and figures 4.22 to 4.25 are used to show this relation knowning that:

- Increasing L_2, the pitch amplitude is higher when the other lengths/angles remain fixed.
- The pitch amplitude does not change too much when ε is varied.

To sum up and analysing all the results which are shown during the chapter for hover case, DS model is the best one because approximates better the experimental values and inside it, the best option is to use Theodorsen's theory with high unsteady effects, independently what type of pitch angle varition is supposed (sinusoidal or 4-bar linkage mechanism).

However, if SS code is chosen, the most suitable unsteady model to be used is Duhamel, although the error committed in comparison to DS code is so significant.

Chapter 5

Forward Flight Analyses

This new chapter is focused on studying the forward flight and analysing the code which has been developed using Matlab. This code and the results obtained with it are going to be presented in the following sections and subsections.

5.1 Numerical Model

As well as it was done with the hover situation, the initial parameters which are necessary to be defined and the equations which describe the numerical model are explained in this first section.

5.1.1 Initial Parameters

The initial parameters needed to start running the code are:

- Blade chord *(c).*
- Blade radius *(R).*
- Blade span *(b).*
- Number of blades *(*N_b*).*
- Maximum pitch amplitude (θ_0).
- Rotation speed (Ω).
- Horizontal advance velocity (V_h).
- Vertical advance velocity (V_v).

In comparison to hover case, the new initial parameters which have to be defined are the horizontal (forward/backward motions) and vertical (upward/downward motions) advance velocities. The other parameters remain the same.

5.1.2 Simplified Numerical Model

After defining the previous initial parameters, the velocities are obtained from equations 3.23 and 3.24. This is done for every azimuthal position in which the lift and drag coefficients are also calculated thanks to unsteady models of section 3.2 or supposing directly the steady case. In this thesis, Theodorsen's model is the only one that it is going to be used in order to obtain results.

Next, the forces and the torque can be calculated using equations from 3.19 to 3.21 and with them, the trusth produced and the power consumed from equation 3.22.

5.2 Model Validation

In this case, the validation of the model is done comparing the variation of the angle of attack showed in reference [2] with the variation obtained thanks to the DS code using Theodorsen model with high unsteady effects for hover case and the simplified numerical model for the four types of movement (forward, backward, upward and downward). The parameters which have been used appear in table 5.1 and the figure 5.1 shows the results obtained for two different rotation speeds.

Table 5.1: Geometry of cyclocopter used in figure 5.1

Characteristic	c (m)	R (m)	b (m)	N_b
	0.3	0.8	1.6	6

4-bar parameters	L_1(m)	L_2(m)	L_3(m)	L_4(m)	ε
	0.8	0.04	0.8041	0.09	10 °

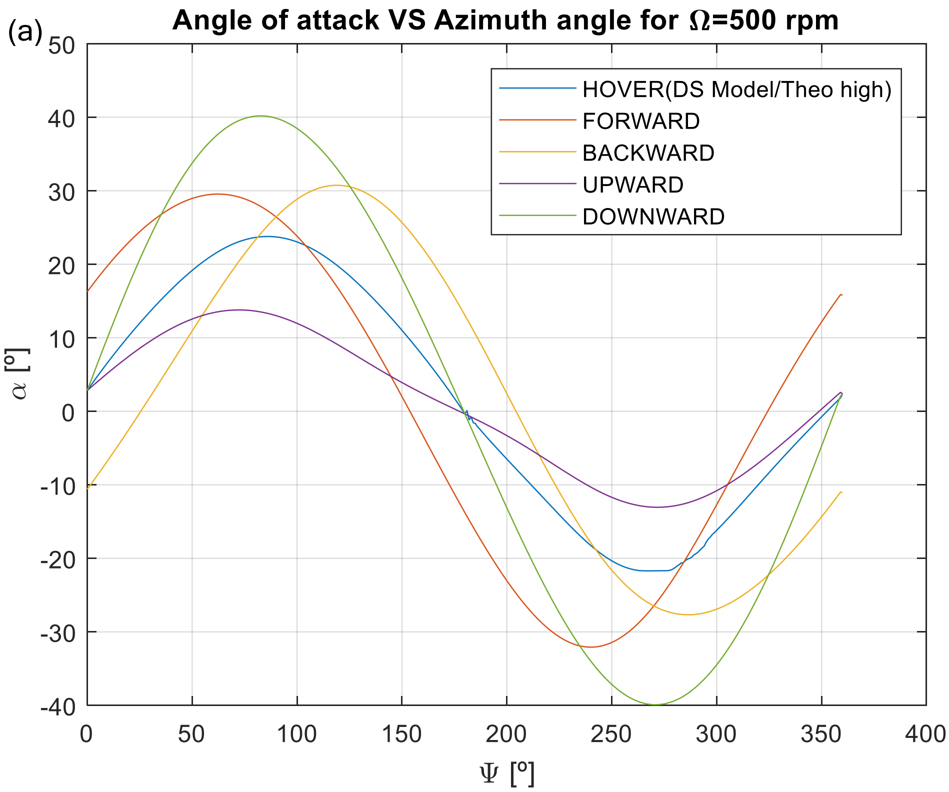

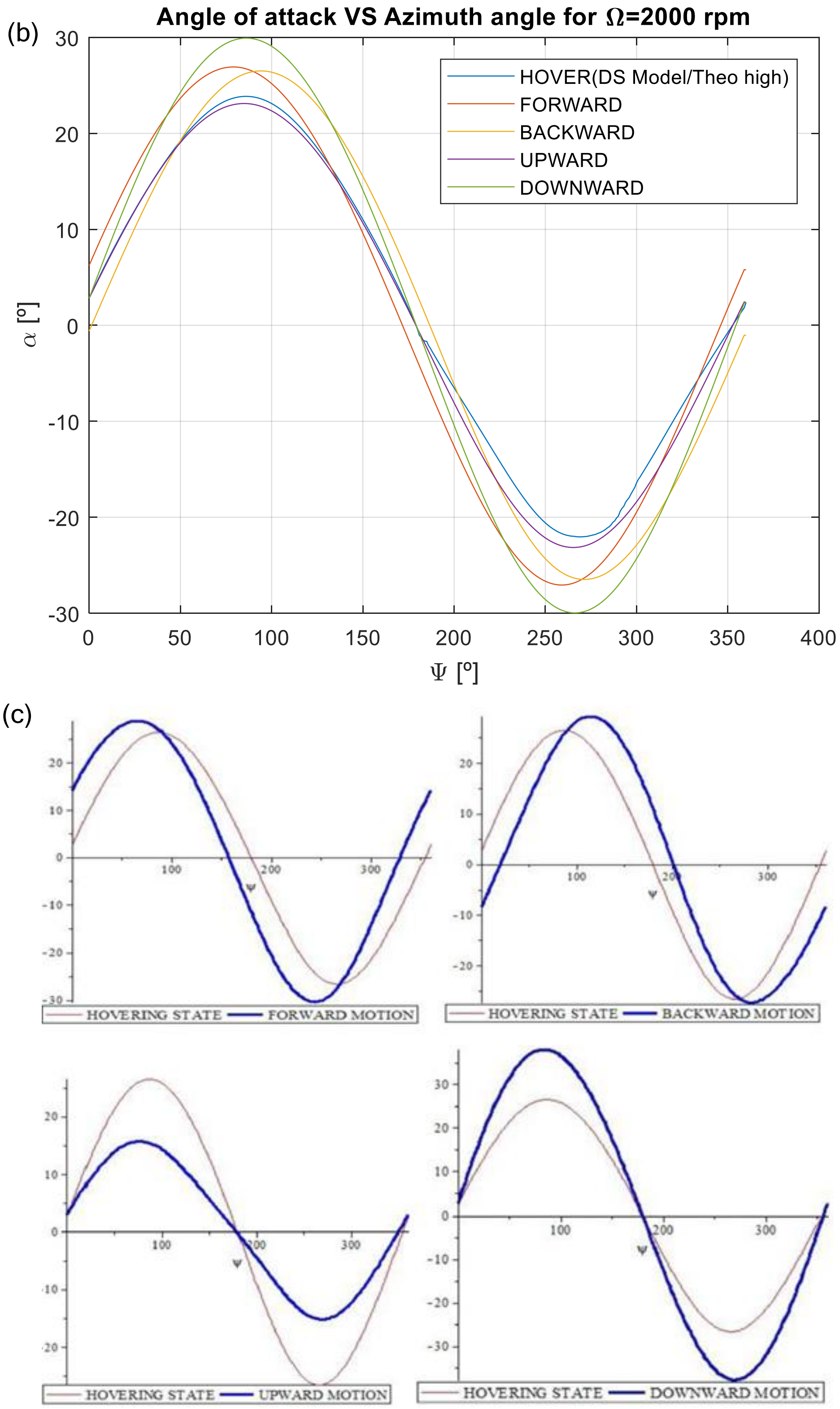

Figure 5.1: Angle of attack variation for hover, forward, backward, upward and downward performances with rotation speeds of (a) 500rpm, (b) 2000rpm and (c) experiments from [2]

Thanks to figure 5.1, the validation of the model is achieved because according to reference [2], the maximum angle of attack is obtained for downward motion and the minimum one for upward. Moreover, the rest of movements are in agreement with reference [2] in value and also in curve shape, particulary when the rotation speed is 500rpm.

5.3 Analyses of Forward Flight

The parameters used to obtain all the graphs which are going to be presented in this section appear in table 5.1.

The first results that are going to be presented are the variation of thrust and power with the rotation speed for the four types of movement and using different advance velocities.

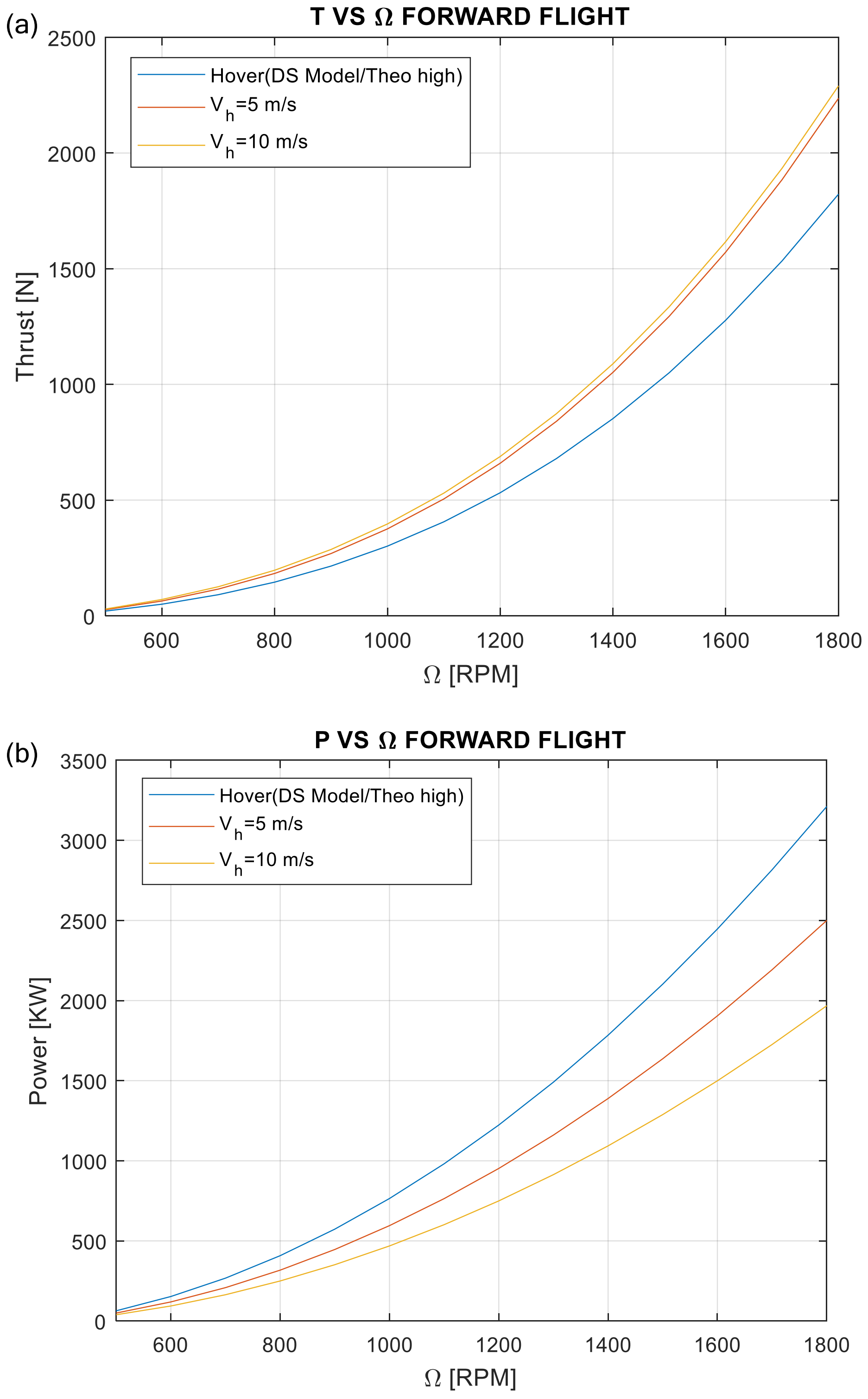

Figure 5.2: Variation of (a) thrust and (b) power with the rotation speed (Forward flight)

According to figure 5.2, increasing the forward velocity (*V_h*), the thrust produced increases and the power consumed decreases. Moreover, in comparison to hover case, the thrust is higher and the power is lower.

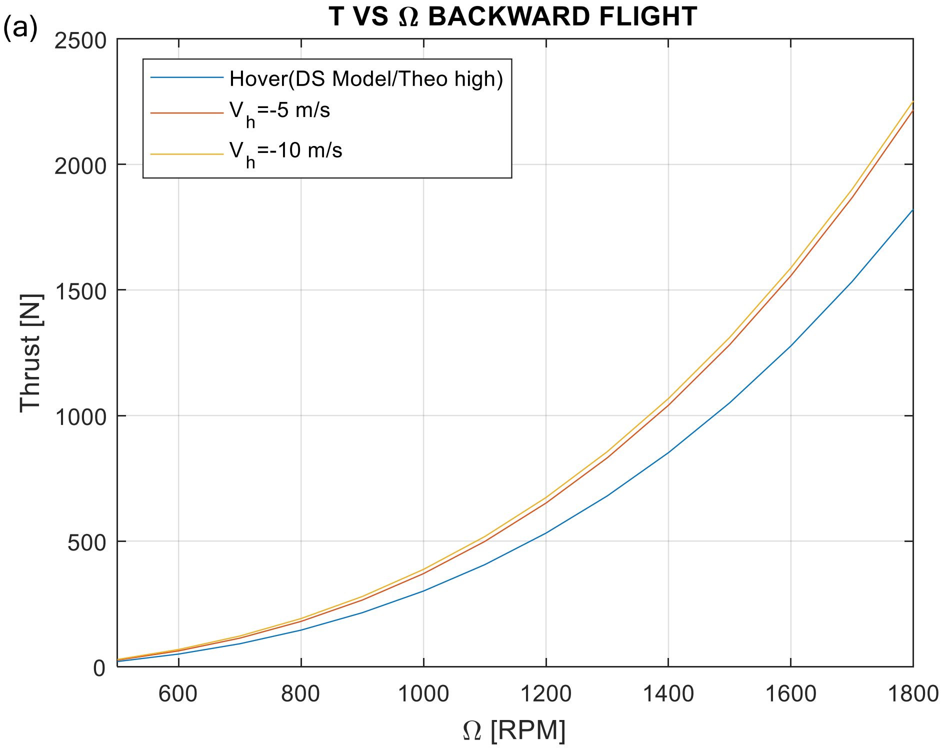

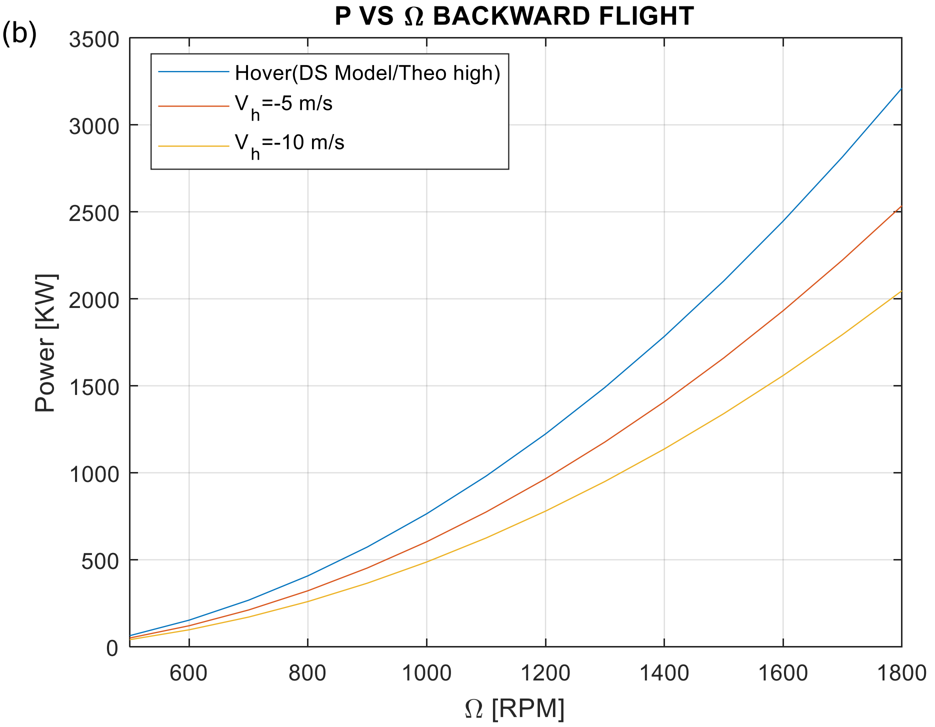

Figure 5.3: Variation of (a) thrust and (b) power with the rotation speed (Backward flight)

For backward motion (figure 5.3), the same conclusions can be extracted as the forward performance because the followed trend and the difference between the thrust produced when the horizontal velocity (*V_h*) is changed are more or less the same in both cases.

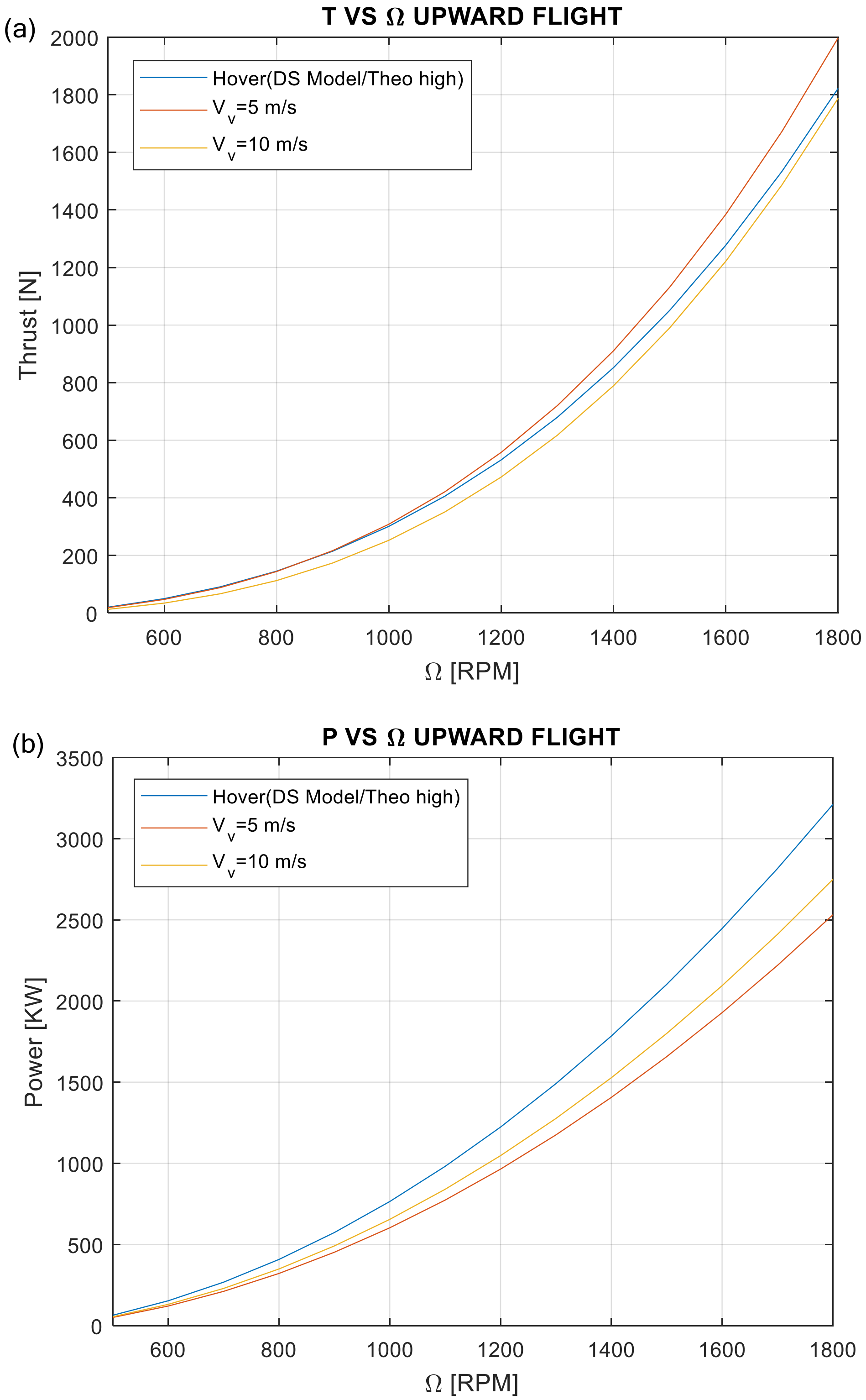

Figure 5.4: Variation of (a) thrust and (b) power with the rotation speed (Upward flight)

This upward motion does not follow a certain trend about the dependence between the thrust and power when the vertical velocity changes and the same occurs when the results are compared with the hover case. The only conclusion that can be obtained is that for the vertical velocities (V_v) used in the figure 5.4, the power needed for upward flight is always lower than the hover case.

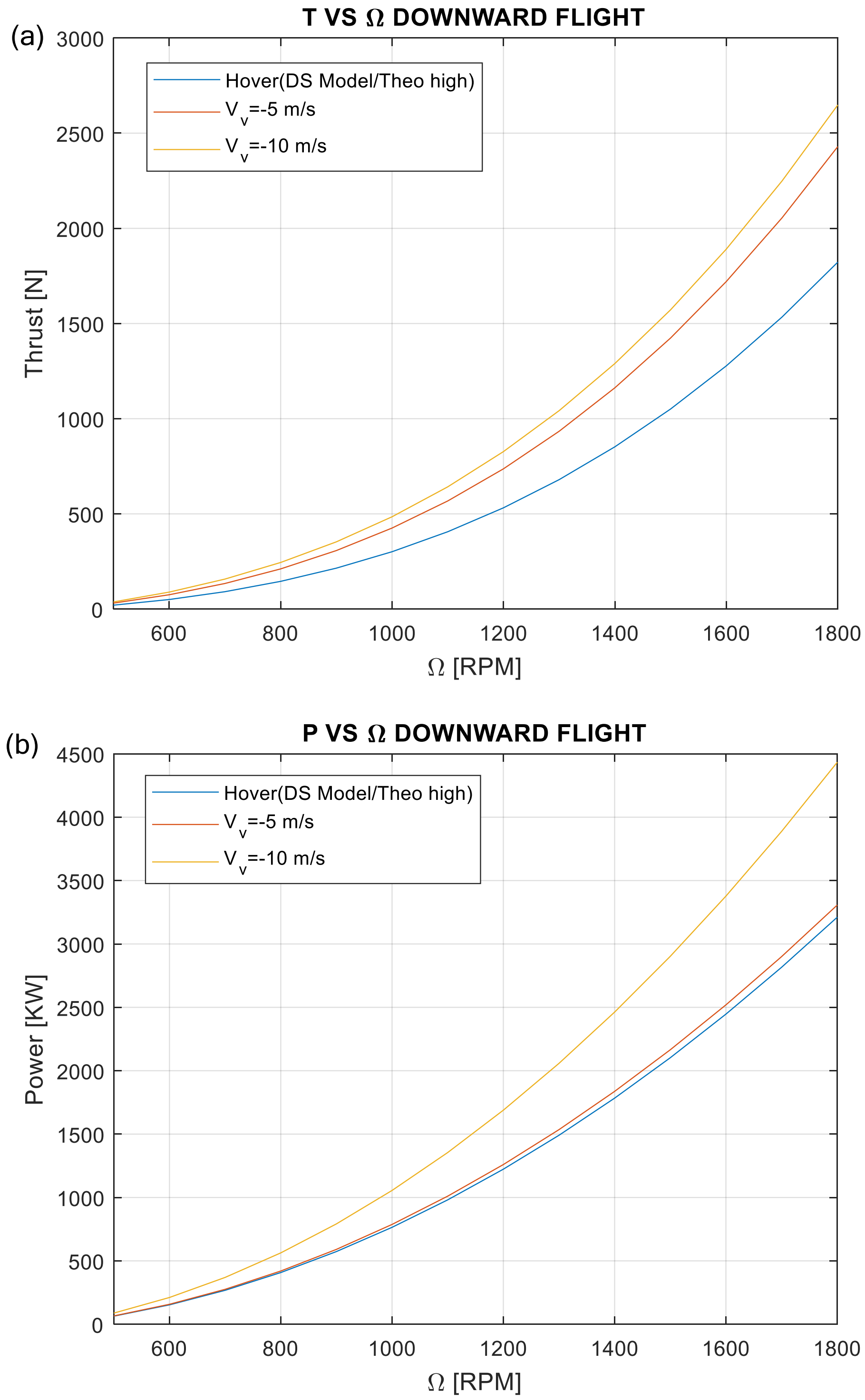

Figure 5.5: Variation of (a) thrust and (b) power with the rotation speed (Downward flight)

However, in this downward flight, the tendence is clear because the thrust and power increase when the downward velocity increases and they are higher than the hover situation.

Comparing now the four previous figures (from 5.2 to 5.5), it is possible to see that for the same value of the advance velocity, the maximum thrust produced is in backward motion which may be due to the help of gravity force for doing this motion. Moreover, this also could explain the opposite case (upward flight) because it produces the lowest thrust. However, the power consumed in backward motion is also the highest one.

Another result which may be interesting to show is the relation between the power consumed and the advance velocity. In order to do this, it is necessary to fix two parameters between these three: thrust, rotation speed or pitch angle variation. In this thesis, the thrust is going to be fixed and the showed graphs are going to be obtained fixing one of the other two and varying the other one.

- FIRST CASE: Thrust and pitch angle variation fixed/ Rotation speed variable.

The result obtained is represented in figure 5.6 in which each marked point shows the necessary rotation speed to achieve this thrust.

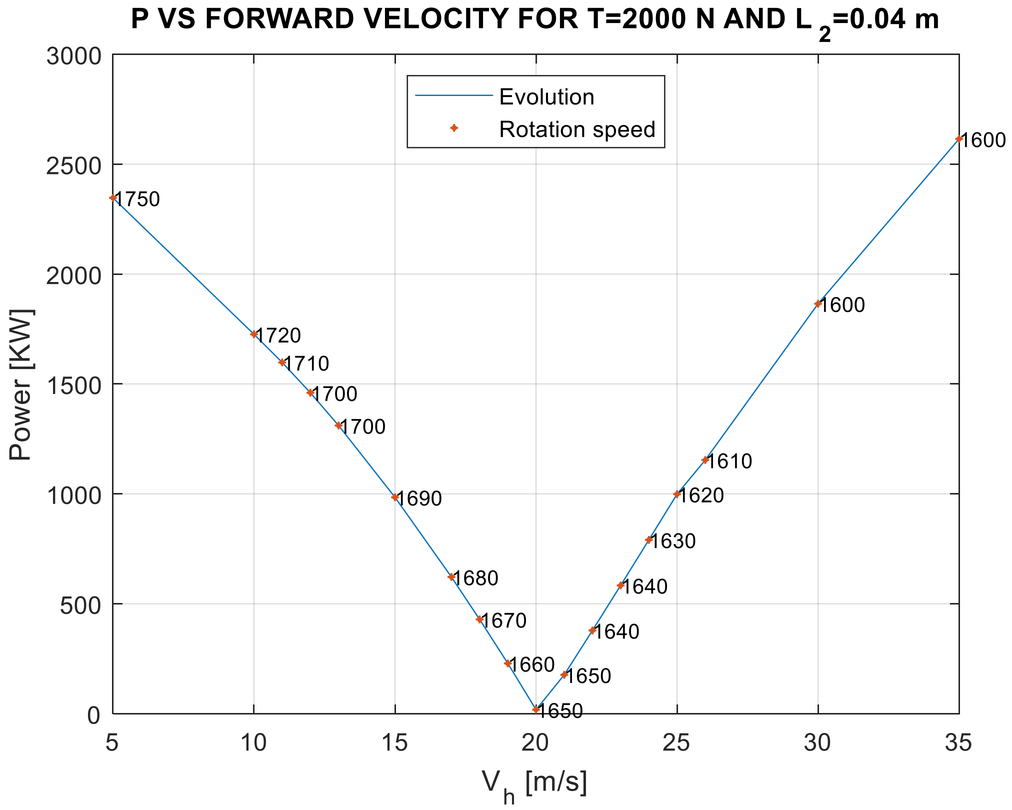

Figure 5.6: Variation of power with the advance velocity fixing thrust and pitch angle variation

Thanks to figure 5.6, it is possible to see that the power consumed is decreasing with the forward velocity until it reaches a minimum and from this point, the power starts to increase. Therefore, this forward velocity in which the power is minimum should be a necessary parameter to know when the thrust and the pitch angle variation are fixed. Moreover, it is possible to see that the rotation speed is always decreasing when the advance velocity increases.

If now the pitch angle variation is fixed but with different values, the result appears in figure 5.7.

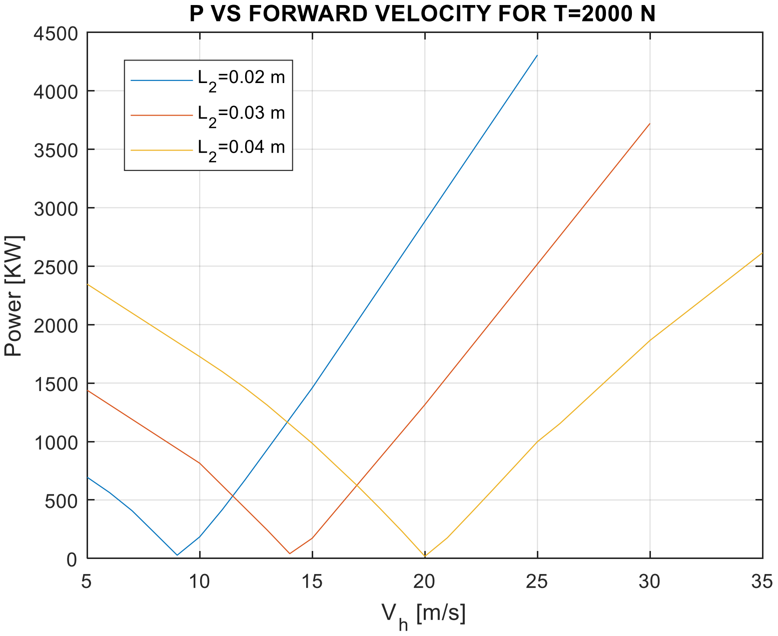

Figure 5.7: Variation of power with the advance velocity fixing thrust for different pitch angle variations

According to figure 5.7, the change in the pitch angle variation is done varying the length L_2 whose relation with the maximum pitch angle was determined in subsection 4.2.2.2 (increasing L_2 increases the maximum pitch angle). Therefore, the forward velocity in which the power is minimum is higher when the length L_2 increases.

- <u>SECOND CASE</u>: Thrust and rotation speed fixed/ Pitch angle variation variable.

This second case is represented in figure 5.8 in which each marked point shows the value of the length L_2 which is necessary to define in order to achieve the fixed thrust.

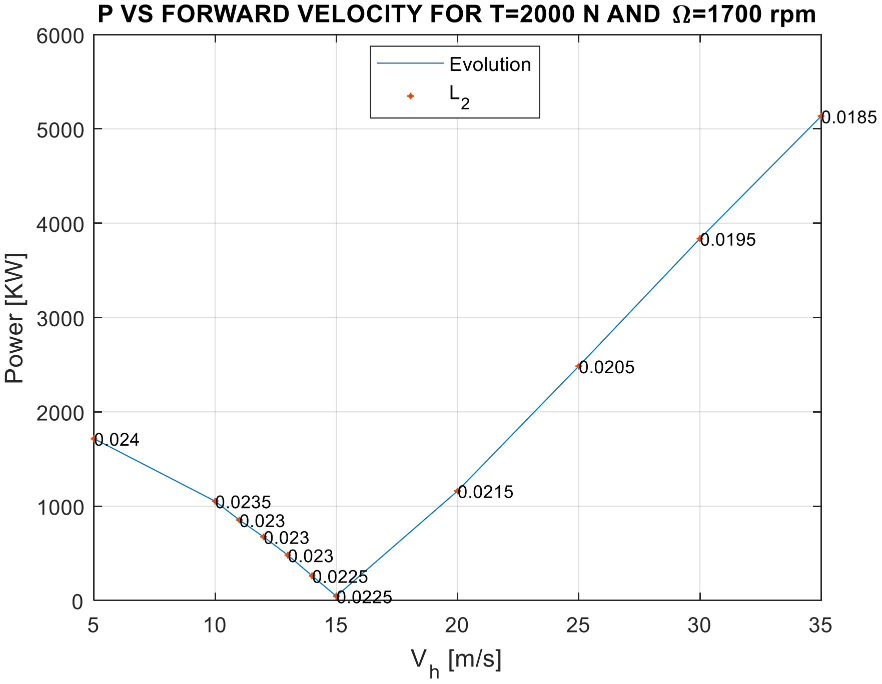

Figure 5.8: Variation of power with the advance velocity fixing thrust and rotation speed

The relation between the power and the advance velocity in this new case remains the same as the first case because the power is decreasing until a minimum value and from this point, it starts to increase. Moreover, the length L_2 has also the same tendence as the rotation speed in case one, as the forward velocity is increasing, this lenght is always decreasing.

Varying now the fixed rotation speed, the result appears in the following figure 5.9:

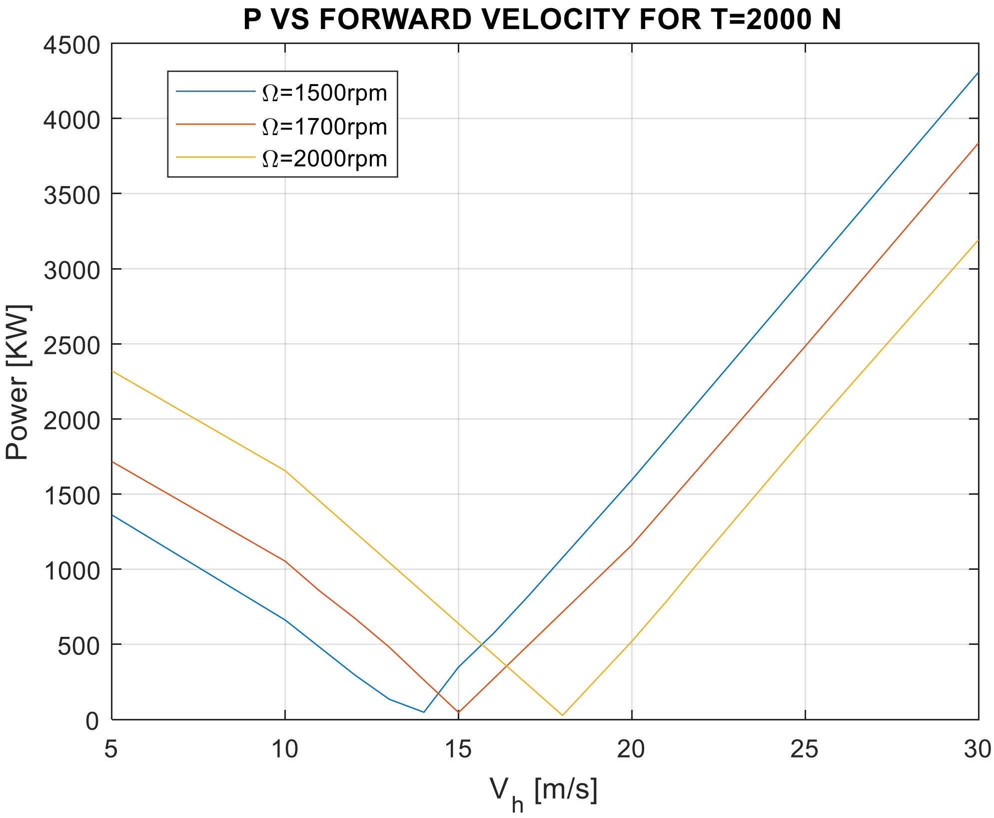

Figure 5.9: Variation of power with the advance velocity fixing thrust for different rotation speeds

Thanks to figure 5.9, it is possible to see that the forward velocity in which the power consumed is minimum is higher when the fixed rotation speed increases, occurring something similar to the previous case with the length L_2.

Chapter 6

Conclusions

6.1 Goals Achieved

The main goal of this thesis was to study, analyse and explain the basic fundamentals about cyclocopters. Thanks to the models presented and the numerical codes developed, their performances have been able to be approximated.

Using some experimental values from different references, the three codes developed (Single Streamtube and Double-multiple Streamtube codes and the forward flight simplified numerical code) could be validated and with it, the results obtained with them. Thanks to these results, some conclusions have been able to be extracted about the behaviour of cyclocopter for hover situation and forward flight.

Finally, the DS code with highly unsteady Theodorsen's model was proved to be the best model because it is the one which is best suited to the experiments.

6.2 Codes Application

According to the last paragraph of the previous subsection 6.1, the DS code may be used to obtain results about the performance of cyclocopters when an user fixs the parameters which define the cyclorotor's problem. Therefore, an application could be elaborated in order to establish a better interface to the user in relation to the data input, solving some difficulties which might appear if the changes are directly done in the DS code. If the forward flight wants to be analysed, the code developed for it can be also used.

This could be achieved using the app-designer tool of Matlab in which an easy application can be developed helping the user about what variables are needed to be introduced to DS code and/or the forward code. With them, the application runs the specific code and displays on the screen the final results of the problem.

Thanks to my teammate Carlos Gallardo Borrego, the cyclocopter application has been posible to be developed with two different options in relation to the inputs which are necessary to be introduced to run the program.

The first one is shown in figure 6.1 and this is a directly application of the developed codes. In figure 6.1, it is possible to see that there are different tabs which allow to select the performance calculation between sinusoidal variation of pitch angle or using the 4-bar linkage mechanism system as well as to change between hover situation and forward flight. The initial parameters which are necessary to be known (and therefore, to be introduced in the application) also appear in figure 6.1 and finally, the thrust produced and the power consumed are displayed on the screen.

Number of blades 4
Radius 0.0000 [m]
Blade span 0.0000 [m]
Chord 0.0000 [m]
Rotation speed 0 [rpm]
Altitude 0.00 [m]
Pitch amplitude 0.00 [deg]
Maximum pitch angle 0.00 [deg]
Thrust 0.0 [N]
Power 0.0 [W]
L2 0.0000 [m]
L3 0.0000 [m]
L4 0.0000 [m]
Phase angle of eccentricity 0.00 [deg]
Maximum pitch angle 0.00 [deg]
Thrust 0.0 [N]
Power 0.0 [W]

Number of blades 4
Radius 0.0000 [m]
Blade span 0.0000 [m]
Chord 0.0000 [m]
Rotation speed 0 [rpm]
Altitude 0.00 [m]
Horizontal velocity 0.00 [m/s]
Vertical velocity 0.00 [m/s]
Pitch amplitude 0.00 [deg]
Maximum pitch angle 0.00 [deg]
Thrust 0.0 [N]
Power 0.0 [W]
L2 0.0000 [m]
L3 0.0000 [m]
L4 0.0000 [m]
Phase angle of eccentricity 0.00 [deg]
Maximum pitch angle 0.00 [deg]
Thrust 0.0 [N]
Power 0.0 [W]

Figure 6.1: Matlab application interface for (a) hover case and (b) forward flight

The second option is shown in figure 6.2 and the aim of it is to calculate the pitch angle variation which is needed in order to obtain a certain thrust. In this application, a sinusoidal variation od the pitch angle is supposed and so, the solution will be directly the pitch angle amplitude. Therefore, the user need to introduced the thrust wanted as well as the rotation speed and the other parameters that appear in figure 6.2. With them, the application shows the lowest pitch angle amplitude (in the range that the user also defines) that is possible to produce the thrust which is also shown on the screen because it depends on the tolerance introduced respecting to the thrust wanted. With this solution, the power consumed is also shown.

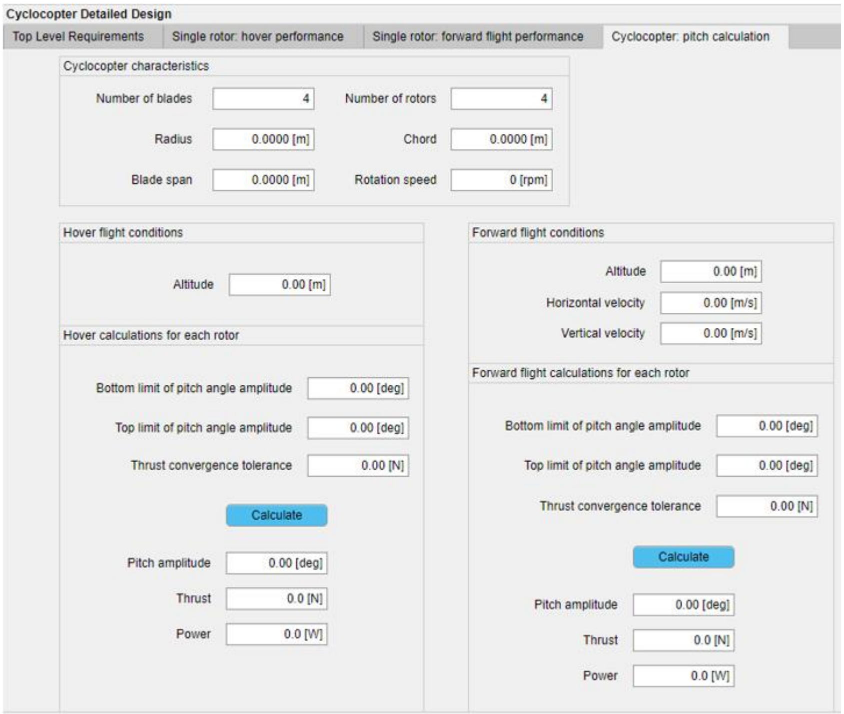

Cyclocopter characteristics

Number of blades: 4
Number of rotors: 4
Radius: 0.0000 [m]
Chord: 0.0000 [m]
Blade span: 0.0000 [m]
Rotation speed: 0 [rpm]

Hover flight conditions

Altitude: 0.00 [m]

Hover calculations for each rotor

Bottom limit of pitch angle amplitude: 0.00 [deg]
Top limit of pitch angle amplitude: 0.00 [deg]
Thrust convergence tolerance: 0.00 [N]
Pitch amplitude: 0.00 [deg]
Thrust: 0.0 [N]
Power: 0.0 [W]

Forward flight conditions

Altitude: 0.00 [m]
Horizontal velocity: 0.00 [m/s]
Vertical velocity: 0.00 [m/s]

Forward flight calculations for each rotor

Bottom limit of pitch angle amplitude: 0.00 [deg]
Top limit of pitch angle amplitude: 0.00 [deg]
Thrust convergence tolerance: 0.00 [N]
Pitch amplitude: 0.00 [deg]
Thrust: 0.0 [N]
Power: 0.0 [W]

Figure 6.2: Matlab application interface for pitch calculation

6.3 Future Works

After completing the thesis and extracting all the conclusions from the results obtained, some future works can be done in order to continue with this research about the cyclocopter:

- Restricting the results shown in the thesis considering the onset of the blades stalling as well as due to the weight of the cyclorotor.
- Calculating the interaction between cyclorotors in the same aircraft as well as being possible to control the thrust module and direction of them in order to do the required performance.
- Analysing the effect of change the blade profile as well as using high-lift devices like flaps during some performances.
- As the forward flight is analysed using a simplified model, some of the results obtained need to be reviewed, maybe developing a more accurate model and analysing the drag coefficient effect on the performance.

Bibliography

[1] M.Benedict. *Fundamental Understanding of the Cycloidal-Rotor Concept for Micro Air Vehicle Applications*. PhD thesis, Department of Aerospace Enginee- ring,University of Maryland, 2010.

[2] J.Monteiro, J.C.Pascoa, and C.Xisto. *Analytical modeling of a cyclorotor in forward flight*. SAE International, 2013. DOI:10.4271/2013-01-2271.

[3] J.Leishman. *Principles of Helicopter Aerodynamics*. CAMBRIDGE UNIVERITY PRESS, 1^{st} edition,2000. ISBN:0-521-52396-6.

[4] C.Yun, I.Park, H.Lee, J.Jung, I.Hwang, S.Kim, and S.Jung. *A New VTOL UAV Cyclocopter with Cycloidal Blades System*. Proceeddings of the 60th Amercian Helicopter Society Annual Forum, Baltimore, June, 2004.

[5] Ira H.Abbott and Albert E.Von Doenhoff. *Theory of wing sections: including a summary of airfoil data*. Courier Corporation, 2012.

[6] Web used: https://automeris.io/WebPlotDigitizer/, Accessed July 2021.

[7] Web used; https://web.mit.edu/drela/Public/web/xfoil/, Accessed June 2021.

[8] *Cyclogyro History*, World-Wide Web document: http://www.rotoplan.narod.ru/historye.htm, Accessed August 2021.

[9] B.Nagler*.* *Improvements in Flying Machines Employing Rotating Wing Systems*. United Kingdom Patent No.280.849, issued November 1926.

[10] C.G.Boirum and S.L.Post. *Review of Historic and Modern Cylcogyro Design*. Paper AIAA-2099-5023, 45th AIAA/ASME/SAE/ASEE Joint Propulsion Conference and Exhibit, Denver, CO, August 2-5, 2009.

[11] M.McNabb. *Development of a Cycloidal Propulsion Computer Model and Comparison with Experiments*. M.S.Thesis, Department of Aerospace Engineering, Mississippi State University, December 2001.

[12] I.E.Garrick. *Propulsion of a flapping an Oscillating Airfoil*. Technical Report 567, National Advisory Committee for Aeronautics, 1937, pp. 419-427.

[13] J.B. Wheatley and R.Windler. *Wind-Tunnel Tests of a Cyclogiro Rotor*. NACA Technical Note No.528, May 1935.

[14] G.Iosilevskii and Y. Levy. *Exprimental and Numerical Study of Cyclogiro Aerodynamics*.

AIAA Journal, Vol.44, (12), 2066, pp 2866-2870.

[15] Y.Levy. *Numerical Simulation of Dynamically Deforming Aircraft Configurations Using Overset Grids*. Journal of Aircraft, Vol.38, No.2, 2001, pp. 349-354.

[16] C.Y.Yun, I.K.Park, H.Y.Lee, J.S.Jung, I.S.Hwang and S.J.Kim. *Design of a New Unmanned Aerial Vehicle Cyclocopter*. Journal of American Helicopter Society, Vol.52, (1), January 2007, pp. 24-35.

[17] S.Kim, C.Yun, D.Kim, Y.Yoon and I.Park. *Design and Performance Tests of Cycloidal Propulsion Systems*. Paper AIAA-2003-1786, 44th AIAA/ASME/ASCE/AHS/ASC Structures Dynamics and Materials Conference, Norfolk, Virginia, April 7-10, 2003.

[18] I.S.Hwang, C.P.Hwang, S.Y.Min, I.O.Jeong, C.H.Lee, Y.H.Lee and S.J.Kim. *Design and Testing of VTOL UAV Cyclocopter with 4 Rotors*. American Helicopter Society 62nd Annual Forum Proceedings, Phoenix, AZ, April 29-May 1, 2006.

[19] *The Development of Cyclogyro*. World-Wide Web document: http://serve.ne.nus.edu.sg/cyclocopter/, Accessed August 2021.

[20] H.Yu, L.K.Bin and H.W.Rong. *The Research on the Performance of Cyclogyro*. Paper AIAA-2006-7704, AIAA 6th Aviation Technology, Integration and Operations Conference Proceedings, Wichita, KS, September 25-27, 2006.

[21] J.Sirohi, E.Parsons and I.Chopra. *Hover Performance of a Cycloidal Rotor for a Micro Air Vehicle*. Journal of American Helicopter Society, Vol.52, (3), July 2007, pp. 263-279.

[22] R.Clark, Acuity Technologies Inc. *SBIR A02.07: VTOL to Transonic Aircraft*. Final technical report, July 24, 2006.

[23] S.Siegel, J.Seidel, K.Cohen and T.McLaughlin. *A Cycloidal Propeller Using Dynamic Lift*. Paper AIAA-2007-4232, AIAA 37th Fluid Dynamics Conference and Exhibit, Miami, FL, June 25-28, 2007.

[24] N.Hara, K.Tanaka, H.Ohtake and H.Wang. *Development of a Flying Robot with Pantograph-based Variable Wing Mechanism*. Proceedings of the 2007 IEEE International Conference on Robotics and Automation, Roma, Italy, April 10-14 2007, pp. 349-354.

[25] H.Nozaki, Y.Sekiguchi, K.Matsuuchi, M.Onda, Y.Murakami, M.Sano, W.Akinaga and K.Fujita. *Research and Development on Cycloidal Propellers for Airships*. Paper AIAA-2009-2850, AIAA 18th Lighter-Than-Air System Technology Conference, Seattle, Washington, May 4-7, 2009.

[26] K.Yang, V.K.Lakshminarayan and J.D.Baeder. *Simulation of a Cycloidal Rotor System Using an Overset RANS Solver*. American Helicopter Society 66th Annual Forum Proceedings, Phoenix, AZ, May 11-13, 2010.

[27] Y.Nakaie, Y.Ohta and K.Hishida. *Flow Measurements around a Cycloidal Propeller*. Journal of Flow Visualization, Vol.16, No.4, 1978, pp. 393-402.

[28] S.Husseyin and William G.Warmbrodt. *Design considerations for a stopped-rotro cyclocopter*

for Venus exploration. NASA International Space University Inter., Aeromechanics Office, NASA Ames Research Center, Moffet Field, CA 94035, 2016.

[29] Atanu Halder and Moble Benedict. *Nonlinear Aeroelastic Coupled Trim Analysis of a Twin Cyclocopter in Forward Flight*. AIAA Journal 59.1, 2021, pp. 305-319.

[30] Elena Shrestha. *All-Terrain Cyclocopter Capable of Aerial, Terrestrial and Aquatic Modes*. Journal of the American Helicopter Society 66.1, 2021, pp.1-10.